Instationnarités dans les interactions choc/couche-limite en régime transsonique : étude expérimentale et analyse de stabilité

F. Sartor

AIX-MARSEILLE UNIVERSITÉ

THÈSE

présentée pour obtenir le titre de

Docteur de Aix-Marseille université

Ecole Doctorale 353 : Sciences pour l'Ingenieur

Spécialité : Mécanique et Physique des Fluides

par

Fulvio Sartor

Unsteadiness in transonic shock-wave/boundary-layer interactions: experimental investigation and global stability analysis

---

Soutenue le 17 mars 2014 devant le jury composé de

Jean-Christophe Robinet	Professeur, ENSAM Paris	*Rapporteur*
Neil D. Sandham	Professeur, University of Southampton	*Rapporteur*
Jean-Paul Dussauge	Directeur de recherche au CNRS, IUSTI, Marseille	*Directeur de Thèse*
Denis Sipp	Maitre de recherche ONERA, Meudon	*Examinateur*
Pierre Dupont	Chargé de Recherche au CNRS, IUSTI, Marseille	*Examinateur*
Uwe Ehrenstein	Professeur, Aix-Marseille université	*Examinateur*
Reynald Bur	Maitre de recherche ONERA, Meudon	*Invité*

ONERA

THE FRENCH AEROSPACE LAB

Abstract

A transonic interaction between a shock wave and a turbulent boundary layer is experimentally and theoretically investigated. The configuration is a transonic channel flow over a bump, where a shock wave causes the separation of the boundary layer and a recirculating bubble is observed downstream of the shock foot.

First, the mean flow is experimentally investigated by means of PIV, then different techniques allows to identify the main unsteadiness of this shock-wave/boundary-layer interaction. As recognised in similar configurations, the flow presents two distinct characteristic frequencies, whose origins are still unknown.

Numerical simulations are performed solving Reynolds-averaged Navier-Stokes equations. Results are in good agreement with the experimental investigation on the mean flow, but the approach fails to predict the unsteady behaviour of the configuration. The solution of RANS equations is then considered as a base flow, and a global stability analysis is performed. Eigenvalue decomposition of the linearised Navier-Stokes operator indicates that the interaction is stable, and the dynamics cannot be described by unstable global modes.

A linearised approach based on a singular-value decomposition of the global Resolvent is then proposed: the noise-amplifier behaviour of the flow is highlighted by the linearised approach. Medium-frequency perturbations are shown to be the most amplified in the mixing layer, whilst the shock wave behaves as a low-pass filter. Optimal forcing and optimal response are capable to reproduce the mechanisms that are responsible for these two phenomena. A restriction on the location of the forcing can give an insight on the origin on the unsteadiness.

The same approach is then applied to a transonic flow over the OAT15A profile, where the flow can present, for a range of angles of attack, high-amplitude self-sustained shock oscillations. Global stability analysis indicates that the shock buffet onset is linked to a Hopf bifurcation, and the eigenvalue decomposition can describe the phenomenon when an unstable global mode is present. Regardless of the angle of attack, singular-value decomposition of the global Resolvent can describe the convective instabilities responsible of medium-frequency unsteadiness.

Contents

1 Introduction **1**

1.1 Shock-wave/boundary layer interactions 2
1.2 Unsteady features in SWBLI 4
1.3 The origins of the unsteadiness 6
1.4 Stability analysis 9
1.5 Outline 11

2 Experimental investigation **13**

2.1 PIV investigation 15
2.1.1 PIV system 17
2.1.2 Shock-induced separation region 21
2.1.3 Boundary layer 28
2.2 Unsteadiness at the wall 30
2.2.1 Pressure fluctuations 31
2.2.2 Skin-friction fluctuations 33
2.3 High-speed Schlieren visualisation 35
2.3.1 Fourier modes decomposition 38
2.3.2 Two-point correlations 41
2.4 Conclusions 45

3 Numerical approach **47**

3.1 Numerical simulation 48
3.1.1 RANS equations 48
3.1.2 Computational grid 52
3.1.3 Results 54

3.2 Global-mode decomposition . . . 57
3.2.1 Theoretical formulation . . . 57
3.2.2 Numerical strategy . . . 59
3.2.3 Results . . . 60
3.3 The global Resolvent . . . 65
3.3.1 Theoretical formulation . . . 65
3.3.2 Numerical strategy . . . 67
3.3.3 Energy maximisation on the whole domain . . . 69
3.3.4 Energy maximisation on a sub domain . . . 77
3.4 Conclusions . . . 82

4 Flow over the OAT15A profile 85
4.1 Experimental investigation . . . 86
4.2 Numerical simulation . . . 88
4.3 Global-mode decomposition . . . 93
4.4 Global-Resolvent analysis . . . 100
4.5 Conclusions . . . 104

5 Conclusions 107
5.1 Perspectives . . . 110
5.2 Acknowledgements . . . 112

Appendices 113

A Résumé en français 113
A.1 Introduction . . . 114
A.2 Résultats expérimentaux . . . 116
A.3 Approche numérique . . . 119
A.4 Tremblement transsonique sur le profil OAT15A . . . 123
A.5 Conclusions . . . 126

Bibliography 129

Chapter 1

Introduction

Shock waves almost inevitably occur when dealing with supersonic flows. The presence of shock waves entails the existence of discontinuities and regions of high gradients, which are the shocks themselves and the shear layers resulting from the interaction with the boundary layers developing on a surface. These gradients "activate" the viscous terms, which produce entropy, making shock waves an important source of drag: directly, by entropy generation in the shock thickness (this contribution is called *wave drag*), and indirectly, by enhancing dissipation in the boundary layer (hence an amplification of *viscous drag*). In addition, strong interactions with the boundary layers may lead to catastrophic separation with possible occurrence of large scale unsteadiness (Délery, 2000).

The interaction between a shock wave and a boundary layer remains one of the most outstanding problems of modern high-speed fluid dynamics. The interaction embodies all of the effects of compressibility, turbulence, and separation that present special challenges for both experimentalists and theoreticians alike. Both external and internal flows are often the subject of shock waves, which interact strongly with turbulent boundary layers.

Shock-wave/boundary-layer interaction (SWBLI) has been the subject of many studies during the last 60 years (Dolling, 2001). The interaction can have a significant influence on aircraft wings, air intakes or rocket performance and often leads to undesirable effects, such as drag rise, drop of the lift due to flow separation, wall heating and shock unsteadiness (Délery and Marvin, 1986). The last of the aforementioned drawbacks has a multidisciplinary importance because it can affect the vehicle and component structural integrity, shortening the fatigue life, and imposing constraints on the geometry or the material selection, introducing additional weight and cost.

Thus, a deeper understanding of the SWBLI phenomenon is required to gain knowledge on a subject that interests both physical and industrial domains.

1.1 Shock-wave/boundary layer interactions

In general, when a shock meets a wall, there is an interaction with the boundary layer that exists in the vicinity of the wall. The strong pressure gradients due to the shock modify the shape of the boundary layer. This deformation, whose effects are notable even before the shock as the flow is subsonic in the boundary layer, modifies the velocity field in the outer part of the flow and thus influences the shock, too.

In SWBLI three configurations are commonly studied: the case of a compression ramp (Ardonceau, 1984; Selig et al., 1989; Thomas et al., 1994; Wu and Martin, 2007), the oblique shock impinging on a flat-plate boundary layer (Dupont et al., 2006; Touber and Sandham, 2009a; Humble et al., 2006) and the normal shock on a wall (or profile) (Délery, 1978; Bur et al., 2006; Bruce and Babinsky, 2008; Pirozzoli et al., 2010a). In the first two configurations, a weak oblique shock interacts with the boundary layer, and the flow remains supersonic after the interaction. In the compression ramp configuration, the shock is induced by the flow-deviation due to the ramp, whilst in the other case the shock is formed by an upstream external device, and reflects on the wall inducing the interaction zone. Besides the different geometry, in both cases the separated zone is proportional to the shock intensity, that is given by the shock slope, and the flow remains supersonic after the interaction. In the last configuration the shock is strong, normal to upstream the velocity direction, and the flow after the interaction is subsonic.

Our study focuses on a strong normal shock impinging on a curved profile in a transonic flow. The shock intensity depends only on the Mach number, function of the downstream pressure and cannot be adjusted through geometrical parameters as is the case in the compression ramp or impinging shock case. This configuration is common in air intakes, nozzles jet or in flows over a profile.

Transonic SWBLI

A transonic interaction, if strong enough to cause the separation of the boundary layer, is characterised by the existence in the outer flow of a lambda shock pattern, like the one appearing in the sketch of figure 1.1: the necessity of this shock shape stems from the fact that the leading shock (labelled S1 in figure 1.1) is a *weak* oblique shock, in the sense of the weak solution of the shock theory, whose strength is a function of only the upstream Mach number M_0 and the incoming boundary layer properties. Thus, referring to figure 1.1, when the shock S1 meets the *strong* quasi-normal shock S3 present in the far outer field, there exists behind S1 and S3 two states 2 and 3 with different pressures and velocity inclinations. At the meeting point I (see figure 1.1) of the two shocks, these states are not compatible, as can

be seen from the shock polar diagram on the right of figure 1.1. In order to fulfill the conditions for two adjacent flows to be compatible, that means having the same pressure and the same velocity orientation, a third state (state number 4 in figure 1.1) must be introduced, with the same pressure and velocity orientation as state 3.

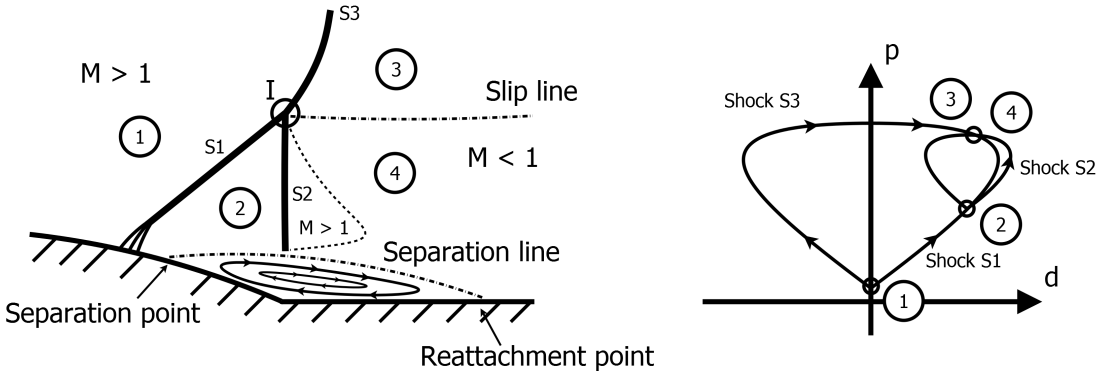

Figure 1.1: Lambda-shock wave pattern and shock polar diagram for a normal shock wave on a wall. From Délery and Marvin (1986).

State 4 is reached through a trailing shock (number S2 in figure 1.1), weaker than the strong shock S3, that is usually barely visible in Schlieren visualisation because of the small density jump across the wave. As shown on the shock polar diagram, the shock exists to ensure the compatibility condition for the two adjacent flows 3 and 4, so that the same pressure and velocity orientation are obtained in this region. Depending on the shock intensity, a locally supersonic zone may exist downstream of this trailing shock. The extent of this zone, called *supersonic tongue*, depends on the particular conditions for the strong coupling process associated to the deviation towards the wall of the reattaching dissipative layer, and its position in the flow field is determined by the separation bubble. The triple point emerging from the meeting of the shocks cited above (point I in figure 1.1) generates a slip line that surround the upper part of the supersonic tongue.

If we consider a transonic flow with upstream Mach number grater than 1.3, the interaction is strong enough to cause the separation of the boundary layer (Délery and Marvin, 1986). The recirculation bubble is however very sensitive to external factors and its stream-wise extent can increase or decrease dramatically as a consequence of shock displacements. For that reason, when studying this configuration, it is common to use a bump in order to increase the size of the recirculation bubble: the separation is caused by both the shock wave and the pressure gradient due to the wall curvature. This is the case also for supersonic flows over airfoils.

The Délery bump

In the present work we consider a well-documented geometry known as the Délery bump or the Délery case C (Délery, 1978; Loyau et al., 1998; Galli et al., 2005; Bur et al., 2006; Sandham et al., 2003), presented in figure 2.2. The incoming flow is supersonic and the boundary layer, as it will be shown in details in the next chapter, is fully turbulent. In this particular interaction, referring again to figure 1.1, the normal shock S3 occurs at Mach number $M = 1.4$, and downstream of the point S1 the Mach number of the outer flow remains everywhere supersonic, its value ranging from 1.05 near the boundary layer edge to 1.15 in the vicinity if the triple point I. Shock S1 has the structure of a weak oblique shock wave, and the Mach number on the downstream face of S2 decreases from nearly 1 at the edge of the dissipative layer to 0.9 near point I. As the boundary layer edge is approached, the rear shock S2 is weakened to such an extent that it causes no disturbance to the wall static pressure distribution. The flow is everywhere subsonic downstream of S2 except for the supersonic tongue, visible in figure 2.6.

In conclusion, if we examine a general interaction between a shock and a boundary layer, many configurations are possible, depending on several parameters such as the geometry, the shock strength, the Reynolds number or the nature of the boundary layer. However, despite the differences in the configurations, there are some aspects of the interaction that can be considered universal, and some features of the flow that can always be found in shock-wave/boundary-layer interactions, not only in the transonic domain with turbulent boundary layer, as the current study.

1.2 Unsteady features in SWBLI

Regardless of the configuration, many experimental and numerical studies have shown the existence of two distinct characteristic frequencies: on the one hand, shock motions involve generally frequencies much lower than those involved in the incoming boundary layer, but on the other hand, the mixing layer downstream of the separation line exhibits unsteadiness whose frequencies are higher than those observed in the shock motions, but still below the energetic scales of incoming turbulence. Inside the recirculation bubble one can find both low-frequency motions, commonly related to the shock, and medium-frequency motions, typical of the mixing layer. The latter unsteadiness can be related to Kelvin-Helmholtz instability triggered in the shear layer downstream the shock wave and above the recirculation bubble. Boundary layer fluctuations are commonly referred as high-frequency motions.

Depending on the shock intensity, the boundary layer can either separate or

remain attached after the interaction, and the flow can either remain supersonic downstream of the shock wave or, in the case of a strong shock, become subsonic. If the flow does not separate, numerical simulations for an impinging shock wave (Garnier et al., 2002) suggest that the flow is stationary. On the contrary, experimental investigations on a transonic case (Bogar et al., 1983) found that the interaction is unsteady, and the shock frequencies vary with the channel length, arguing the possibility that the natural frequencies are associated to the longitudinal acoustic modes of the channel. If the flow separates, in both strong- and weak-shock cases, an acoustic feedback is possible, at least in the subsonic zone between the reattachment of the bubble and the shock foot. According to Souverein et al. (2010), without separation the flow unsteadiness may be mostly governed by upstream events, with the predominance of high-frequency oscillations coming from the boundary layer. However, Piponniau et al. (2009) documented that low-frequency unsteadiness is present even without flow separation.

It has been documented that SWBLI unsteadiness is independent of the laminar or turbulent nature of the incoming flow (Chapman et al., 1958). Moreover, it was shown (Dussauge and Piponniau, 2008) that the shock motion increases with the shock intensity. Numerical simulations (Wu and Martin, 2007; Garnier, 2009; Touber and Sandham, 2009a) indicate that in most configurations, both low- and medium-frequency unsteadiness are broadband fluctuations, with the exception of the transonic flow over a non-swept two-dimensional profile: it is known (McDevitt and Okuno, 1985) that for a combination of Mach number and angles of attack, the so-called buffet phenomenon dominates the interaction. In this particular case, the unsteadiness is characterised by a high-amplitude modulation of the shock wave with a very narrowband spectrum, and the shock exhibits periodic high-amplitude motion, maintained without any external input of energy (Lee, 2001). In this case a unique frequency value can describe the periodic pressure fluctuations of the shock (Deck, 2005; Barakos and Drikakis, 2000) for various angles of attack.

In conclusions, regardless of the topology of the oscillations, one might say that low-frequency unsteadiness can always be found in viscous interactions, and medium-frequency motions are commonly related to the separated zone, and associated to vortical structures that propagate along the shear layer. However, numerical simulations revealed some exceptions: the DNS performed by Wu and Martin (2008) documented the presence of small-amplitude span-wise wrinkling on the shock, probably due to non-uniformity of turbulent structures in the incoming boundary layer. Agostini et al. (2012), analysing results of LES computations, confirmed the presence of these medium-frequency motions, arguing that the kinematics of the shock is the mirror of the physical phenomena in the separated zone, whatever the frequency.

The Strouhal number

As commonly done in SWBLI (Erengil and Dolling, 1991b), one can introduce a dimensionless frequency (or Strouhal number) defined as

$$S_L = \frac{f L_{sep}}{U_e} \tag{1.1}$$

where f is the frequency, L_{sep} is the separation length and U_e is the external velocity. Although widely used, other reference scales may be used to define the Strouhal numbers: in some configurations (typically when the separated zone displays a limited extension) it is common to use an interaction length scale, defined as the distance between the mean reflected-shock-foot position and the nominal inviscid impingement location. Using this scaling, Dussauge et al. (2006) have shown that a typical value of $S_L = 0.02 - 0.05$ can describe qualitatively the shock motions in several experiments as well as in numerical simulations. However, the frequencies found based on this scaling exhibit some scatter in the values, as also noted by the authors, so it is not obvious that a unique value, independent of flow conditions, should exist.

Regardless of the precise value of the Strouhal number, it is well established that the shock exhibits low-frequency motions and that the separation-point position is directly linked to this unsteadiness. Even if, as it will be discussed in the next section, it is still not clear if the bubble motions are the cause or the consequence of the shock displacement, there is a clear relation between the two phenomena: it has been shown that low-frequency shock motions are linked to the contraction and expansion of the bubble (Dupont et al., 2006), and for this reason it is common to refer as *breathing* of the recirculation zone the low Strouhal number motions (or pulsations) of this region.

Using the same frequency scaling, one can compute the Strouhal number of the medium-frequency motions of the mixing layer. Typical values spanning from $S_L = 0.1$ to $S_L = 0.5$ are common for subsonic shock-induced separation cases, and are often referred to as *flapping* motions of the recirculating zones (Kiya and Sasaki, 1983). Those motions have been acknowledged since a long time (Cherry et al., 1984) and have been associated to Kelvin-Helmholtz type instability. As explained by Piponniau et al. (2009), even if the low- and medium-frequency typical values depend on the flow conditions, there is at least a factor four between the two values.

1.3 The origins of the unsteadiness

If medium-frequency motions of the separated zone are commonly related to the shear layer downstream the interaction, the origin of low-frequency motions affect-

ing shock waves is controversial, and the question of why shock oscillations occur remains rather unexplained. One of the first answers was suggested by Plotkin (1975), who developed a mathematical model to explain the low-frequency unsteadiness in SWBLI: the main idea is that the shock foot is affected by the passage of turbulent eddies, while the stability of the mean flow tends to restore the shock to its original position.

The hypothesis of shock motions caused by organised structures existing in the incoming flow has been verified by several experimental investigations: Andreopoulos and Muck (1987) found that the frequency of the shock-wave unsteadiness is of the same order as the bursting frequency of the upstream boundary layer, and that this frequency is independent of the downstream separated flow. Afterwards Erengil and Dolling (1991a) and Dolling and Erengil (1991) found correlations between pressure fluctuations in the upstream boundary layer and the shock velocity, but in a more recent study Beresh et al. (2002) suggest that a thickening/thinning boundary layer is not the cause of the shock unsteadiness: a correlation between stream-wise velocity fluctuations in the upstream boundary layer and the shock position indicates that low-frequency shock motions are inherited from eddies in the incoming flow, and that the separation bubble responds to the movements of the shock wave. In a compression ramp configuration, Ganapathisubramani et al. (2007) confirmed this last theory, documenting the existence of long stream-wise coherent structures in the boundary layer that are related to shock motions.

While the shock is undoubtedly affected by the passage of low- or high-speed streaks, as for instance evidenced by the tomographic particle image velocimetry study of Humble et al. (2009), the success of the mechanism proposed by Ganapathisubramani et al. (2009) to explain the low-frequency shock motions depends on the existence of sufficiently long streaky structures. To prove that upstream events are not the only cause of shock unsteadiness, Touber and Sandham (2009b) performed large-eddy simulations in a shock-reflection configuration where special care was devoted to the inflow conditions to prevent the development of coherent structures. Although the upstream boundary layer was deprived of very long coherent structures, the low-frequency shock motions could still be observed. The LES computation of Hadjadj (2012) confirms this result, suggesting that low-frequency instabilities are due to the intrinsic movement of the shock/bubble acting dynamically as a coupled system. This result is an indication that the aforementioned structures existing in the upstream boundary layer are not necessary for the low-frequency SWBLI dynamics: if they exist the shock will be undoubtedly affected, but upstream events might be only one of several contributing mechanisms.

Another interesting theory suggests that it is the downstream flow that plays the

most important role in driving the low-frequency shock motions. Supporting this idea, in a Mach 1.5 compression ramp configuration, the experimental investigation of Thomas et al. (1994) indicates that the dynamics in the separation bubble is responsible at first-order of the shock oscillations. This result is not in complete disagreement with the previous theory, because separation bubbles are known to amplify incoming disturbances (Dovgal et al., 1994), which can affect the shock position through the separated zone. However, in a shock-reflection configuration, Dupont et al. (2006) measured pressure fluctuations at two points along the centreline of the flow, and found very weak coherence between the unsteadiness in the upstream boundary layer and those at the shock foot. On the contrary, fluctuations at the shock foot are found to be strongly correlated with the separated zone and with the flow downstream of the reattachment. A small correlation between the low-momentum structures in the incoming boundary layer and the separation point has been documented also by the direct numerical simulations of Wu and Martin (2008), where it is shown that the low-frequency shock unsteadiness is influenced by the downstream flow. This result has been experimentally confirmed by the PIV investigation of Dupont et al. (2008), highlighting the evidence of a link between the reflected shock excursions and the size of the separated flow.

These latter studies deny the thesis that incoming turbulent eddies are the cause of shock motions, and support the theory that the observed low-frequency oscillations are caused by coupling between the dynamics of the separation bubble and the shock, either through global instability of the separation bubble, or through some mechanism of self-sustainment: Pirozzoli and Grasso (2006) performed DNS on an impinging SWIBLI and proposed that the large-scale low-frequency unsteadiness is due to an acoustic feedback, similar to those responsible for the generation of tones in cavity flows. However their simulation did not extend to long-enough times to capture the lowest-frequency motions observed in the experiments.

The two theories described, even if in disagreement on the location, support the idea that the instability of the system is driven by a unique source. However, a plausible model is that the interaction responds as a dynamical system that is forced by external disturbances (Clemens and Narayanaswamy, 2014). In this respect, Touber and Sandham (2011) proposed an original derivation of the Plotkin (1975) equation and indicated that the low-frequency unsteadiness was related to a fundamental property of the shock wave. The model is obtained by using a combined numerical/analytical theory, and proves that the coupling between the shock and the boundary layer is mathematically equivalent to a first-order low-pass filter. According to Touber and Sandham (2011) the observed low-frequency unsteadiness in such interactions is not necessarily a property of the forcing, either from upstream

or downstream of the shock, but an intrinsic property of the global system.

This theory is interesting since it does not deny the possibility of correlations between the shock motions and the incoming boundary layer or the separated flow, and extends the conceptual idea that the shock could act as a low-pass filter, formally expressed by Plotkin (1975) and, to the author knowledge, verified only by Poggie and Smits (2001, 2005). Combining the theoretical formulation with LES simulations, Touber and Sandham (2011) showed that the low-frequency motions can simply arise from a background noise, and the shock filters the fluctuations, arising from the separated region or coming from the upstream boundary layer, up to a given cut-off frequency, which would lead to the observed low-frequency unsteadiness.

1.4 Stability analysis

Linear stability analysis has become a tool commonly used in fluid dynamics, which can often give physical insights to understand flow unsteadiness (Theofilis, 2003; Sipp et al., 2010). According to Huerre (2000), occurrences of unsteadiness can be classified into two main categories: the flow can behave as an oscillator, and an absolute instability imposes its own dynamics, or it can behave as a noise-amplifier, in which the system filters and amplifies existing environmental noise, due to convective instabilities.

In the first case, a global-mode decomposition has the ability to identify the mechanism responsible for the self-sustained unsteadiness, indicating that the flow is driven by an unstable global mode (Theofilis, 2011). In other configurations, where the unsteadiness is characterised by a broadband spectrum and needs an external forcing to persist, the flow does not exhibit any unstable global mode. The linearised Navier-Stokes operator acts as a linear filter of the external environment, and a frequency-selection mechanism leads to a broadband spectrum: the eigenvalue decomposition poorly describes the dynamics of the phenomenon (Trefethen et al., 1993; Sipp et al., 2010). In such cases a singular-value decomposition of the Navier-Stokes evolution operator highlights optimal growth phenomena, which are more suitable to describe the dynamics of a globally stable flow. The connection between transient growth and convective instability has been discussed by Cossu and Chomaz (1997) and numerous studies have successfully applied this method in different configurations (Ehrenstein and Gallaire, 2005; Abdessemed et al., 2009).

In shock-wave/boundary-layer interaction, only few studies tried to answer the question on the origins of the unsteadiness through stability analyses. Investigating the linear stability using a base-flow derived from two-dimensional DNS, Robinet

(2007) suggested that in a laminar SWBLI an unstable global mode, whose existence depends on the shock intensity, may be the source of the unsteadiness. However the mode was found to be three-dimensional and non-oscillatory, and has not been directly linked to the low-frequency shock oscillations. The work of Robinet (2007) may be an extension to the supersonic domain of the existence of stationary global instabilities inside recirculation bubbles: the interaction between the shock wave and the boundary layer may cause, depending on the shock intensity, a recirculation zone, whose behaviour dominates in the global stability analysis. Similar results confirming that the flow becomes globally unstable via a three-dimensional stationary mode have been found in subsonic boundary-layer separations (Theofilis et al., 2000), over a backward-facing step (Barkley et al., 2002) or in a flow over a bump (Gallaire et al., 2007).

In a transonic flow over a NACA0012 profile configuration, Crouch et al. (2007, 2009) performed a global stability analysis using a base flow resulting from RANS simulations. They found a strong link between the onset of shock unsteadiness in the interaction and the appearance of an oscillatory unstable global mode. It has been shown that, for a given Mach number, a critical value of the angle of attack exists above which the shock starts to oscillate, in the same way that a critical Reynolds numbers is responsible for vortex shedding in a cylinder wake (Jackson, 1987). Results are shown to be in good agreement with both experiments and numerical URANS simulations. The study provides evidence linking the transonic buffet onset to a Hopf bifurcation, indicating that a single oscillatory unstable global mode can represent the low-frequency self-sustained shock motions.

In a shock impinging on a turbulent boundary layer configuration, Touber and Sandham (2009b) performed a global-mode decomposition of a mean flow obtained by time and span averaging the result of a three dimensional LES computation. The mean flow obtained is in excellent agreement with experimental and numerical results, but the most unstable global mode was found to be stationary (with zero-frequency), so this result cannot be considered relevant to discuss unsteadiness. Moreover, the mode being two-dimensional, it cannot be linked to the stationary three-dimensional mode inside recirculation bubbles found by Robinet (2007) and other researchers in the case of incompressible bubbles. Global modes must display non-zero frequency to account for an unsteady phenomenon; for example, Ehrenstein and Gallaire (2008) have shown that unstable oscillating bi-dimensional global modes exist in certain incompressible separation bubbles. The fact that the mode found by Touber and Sandham (2009b) is stationary and 2D does not give any information about the unsteadiness.

Following a similar approach on the same configuration, Pirozzoli et al. (2010b)

confirmed the presence of a single, non-oscillatory exponentially growing mode, but as for Touber and Sandham (2009b) study, the link between the mode and the low-frequency unsteadiness remains a hypothesis. However, contrary to the previous work, Pirozzoli et al. (2010b) also documented the presence of slightly damped oscillatory modes. Those modes, even if stable, display frequencies comparable to the low-frequency unsteadiness observed in full LES and spatial structures that resemble the breathing motions of the recirculation bubble. These partial results constitute a hint that a linearised approach can give insight on the low-frequency dynamics of the flow, but eigenvalue decompositions may not be the correct approach to address this problem, because broadband fluctuations cannot be described by a series of unstable global modes.

If shock-wave/boundary-layer interactions behave as noise amplifiers, the unsteady behaviour would be better described through an analysis of its receptivity to external forcing. In a general view, this approach highlights the property of the linear operator by extracting optimal forcings that lead to largest responses. In separation bubbles the existence of optimal growths has been proven by Marquet et al. (2008a); Blackburn et al. (2008), who described the flow dynamics by analysing the two- and three-dimensional initial perturbations that maximise the energy gain over a given time horizon. In configurations where there is a strong frequency-selection process, working in the frequency domain instead of the temporal domain, as done in optimal growth method, has a deeper physical meaning (Farrell and Ioannou, 1996). Such an analysis can show if some frequencies are amplified by the shock, the mixing layer or the recirculation bubble, and if there is a link between the unsteadiness observed in experiments and the response of the shock as it reacts to the broadband pressure fluctuation environment. A similar approach has already been used to describe the most amplified modes in a channel-flow configuration (Jovanovic and Bamieh, 2005), in a turbulent pipe flow (McKeon and Sharma, 2010) and in a Blasius boundary layer (Brandt et al., 2011).

1.5 Outline

In this work we propose to characterise the unsteadiness in a transonic shock-wave/boundary layer interaction by means of experimental investigations and linear stability analyses. We consider a channel-flow configuration at Mach number 1.4, where the interaction between a strong shock and a turbulent boundary layer causes the separation of the flow, leading to a recirculation bubble which is observed downstream the shock foot.

The experimental investigation is proposed in chapter 2: two-component PIV

measurements and oil-flow visualisation yield to a complete description of the mean velocity field (section 2.1), and the results will be used to validate the numerical simulations presented in chapter 3. Unsteady transducers and high-speed flow visualisation give an appraisal of the temporal behaviour of the flow, identifying low- and medium-frequency peaks and indicating the zones of the flow where this unsteadiness is most energetic: the frequency-selection process is highlighted in section 2.2 using wall pressure and skin-friction measurements. Then, Fourier modes decomposition of Schlieren photography (section 2.3) can give an insight of the location of low- and medium-frequency unsteadiness, whilst cross-correlation maps indicate their spatial structures.

The numerical approach is presented in chapter 3: in section 3.1 the results of the numerical simulation are compared in with the mean flow experimentally obtained. The theoretical formulation that leads to the linear stability analysis is then introduced. Results of the global-mode decomposition are presented in section 3.2, whilst the results of the stability analysis based on the singular-value decomposition of the global Resolvent are in section 3.3. Both approaches will assess the ability of linear stability analyses to predict the various flow unsteadiness phenomena observed experimentally.

Finally, we will consider in chapter 4 another type of SWBLI, where a normal shock causes the separation of the boundary layer over the OAT15A profile at different angles of attack. The configuration, that has been experimentally investigated by Jacquin et al. (2009), is presented in section 4.1. Then, a wide range of angles of attack is numerically investigated by means of RANS and URANS simulation (section 4.2), spanning from $\alpha = 2.5^\circ$ to $\alpha = 7.0^\circ$. When the angle of attack exceeds a critical value, the flow presents high-amplitude periodic low-frequency oscillations, known as shock buffeting. In section 4.3 we will show how direct and adjoint modes decomposition can describe the main features of the flow. Then, in section 4.4 we perform singular-value decompositions of the global Resolvent as proposed for the channel-flow configuration, and compare the results to discuss the difference between the two SWBLI considered.

Chapter 2

Experimental investigation

In this chapter, we present the main results of the experimental investigations conducted in the so called Délery bump configuration. The experiments were performed in the S8Ch transonic wind tunnel of the ONERA Meudon centre, a continuous open-loop wind tunnel supplied with desiccated atmospheric air. The stagnation conditions were near ambient pressure and temperature: $p_{st} = 0.96 \cdot 10^5 \pm 300$ Pa and $T_{st} = 300 \pm 10$ K. The associated unit Reynolds number is around $Re = 14 \times 10^6 \mathrm{m}^{-1}$ which leads to a value of $Re_\Theta = 3500$ for the incoming boundary layer. An air dryer is placed after the air inlet to control the humidity of the flow: during every test run the rise of the total temperature was lower than 2° C degrees, and the dew point is maintained around −50° C.

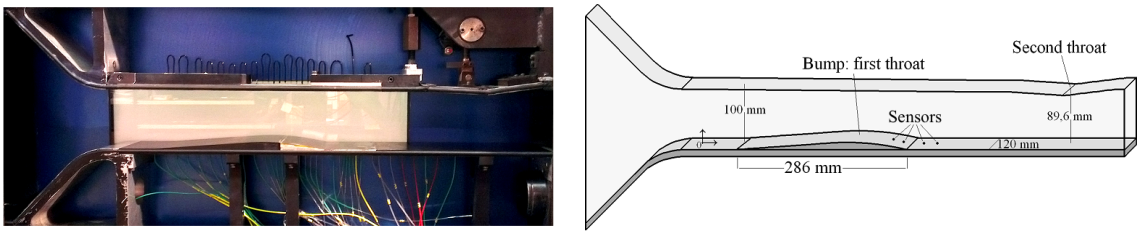

(a) Photo of S8Ch wind tunnel.

(b) Schematic diagram.

Figure 2.1: Photo and sketch of the test section of the S8Ch wind tunnel.

The test section has a span of 100×120 mm, and as shown in figure 2.1 the lower wall is a profile designed to produce a uniform supersonic flow. A second throat of adjustable cross section is placed at the outlet, and causes, by choking effect, a shock wave whose position and intensity can be adjusted in a continuous manner. In the present conditions, the ratio between the two throat sections is 1.12, and the shock occurs at Mach number $M = 1.4$.

Two-component LDV measurements performed in the same configuration and facility (Bur et al., 1998, 2009) showed that on the bump, upstream of the shock,

the boundary layer is fully turbulent with the following characteristics: physical thickness $\delta = 4$ mm, displacement thickness $\delta^* = 0.46$ mm, momentum thickness $\Theta = 0.25$ mm and incompressible shape parameter $H_i = 1.42$. Comparing to similar studies (Dupont et al., 2008; Humble et al., 2006; Lapsa and Dahm, 2011), the boundary layer thickness is very small and consequently measurements close to the wall are more challenging.

The position of the shock is monitored by the evolution of static pressure through 36 pressure taps on the lower wall. The detachment of the boundary layer starts already on the bump and the recirculating bubble, whose average size can be evaluated by the oil-flow visualisation or PIV measurements (see section 2.1), extends after the end of the profile. Previous studies (Galli et al., 2005) showed that there is an optimal position of the lambda shock to achieve the maximal size of the recirculation zone, obtained when the tangent of the shock normal to the lower wall is 12.6 mm downstream of the end of the bump. As the present study focuses on the separation of the boundary layer, the shock wave is maintained in that position in order to obtain the largest recirculating zone.

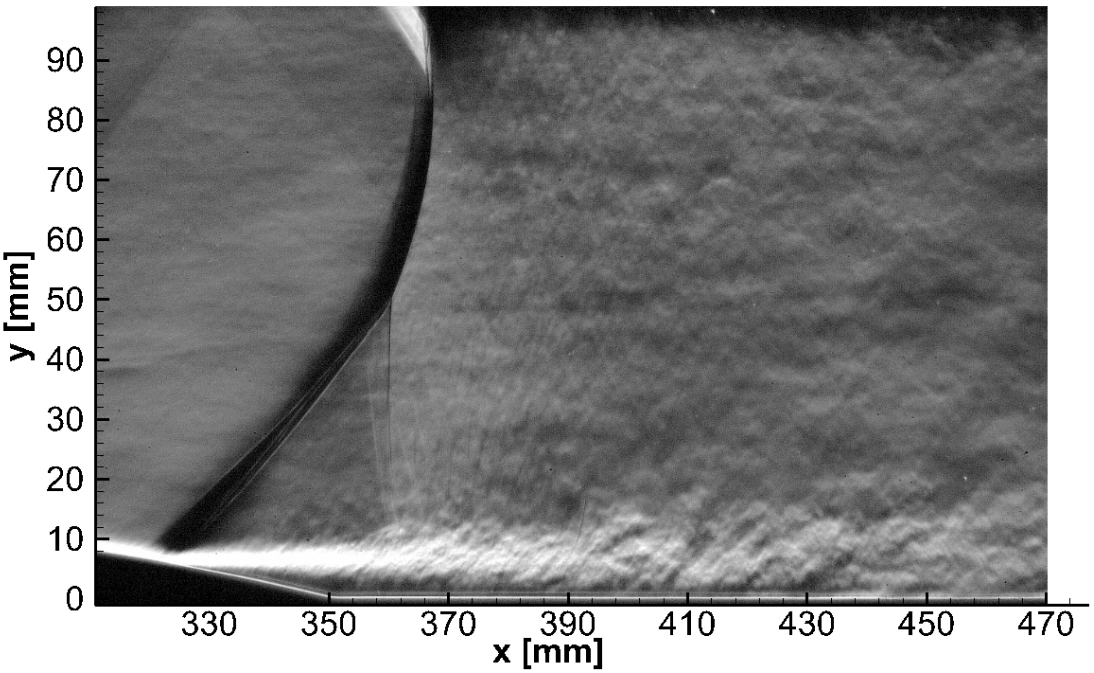

Figure 2.2: The end of the bump with the lambda shock wave: Schlieren photograph of the interaction, horizontal knife.

Downstream of the shock wave, the nominal Mach number is approximately $M = 0.75$ in the upper zone, where the shock can be considered normal, and its value increases up to $M = 0.95$ as approaching the triple point where the two legs of the shock merge together, as shown in figure 2.2. Finally, it is important to note that

the second throat placed at the end of the test section produces a further supersonic zone that acts like a filter to the existing downstream noise that comes from the engines at the end of the wind tunnel.

To visualise the flow and monitor the shock position in the test section, a Schlieren apparatus is used. Very high-speed Schlieren photography give access to a general description of the flow and its motions: a wide field (1280×800 pixels) at frequency rate 7500 fps framed the whole interaction, from the separation point to the completely developed shear layer, yielding a complete characterisation of the shock structure (figure 2.2), whilst a smaller image (460×360 pixels) at frequency rate 35000 fps is used to gain understanding of the temporal and spatial characteristics of the interaction, as it will be shown in section 2.3. The knife-edge of the Schlieren apparatus was oriented both horizontally and vertically, giving access to a complete description of the vertical and horizontal components of the density gradient.

The chapter proceeds as follows: a PIV study is first presented in section 2.1, aiming at characterising the mean features of the flow field (Sartor et al., 2012). The results will be used to validate the numerical simulation that will be performed in the next chapter. Particular attention will be given to the turbulent behaviour of the separated zone, and the boundary layer will be investigated using special lenses. Once the flow is described in its steady behaviour, we focus on the unsteadiness by wall measurements (section 2.2): unsteady pressure transducers and skin-friction sensors will be placed in different zones of the flow, in order to characterise the frequency of the unsteady phenomena involved in the interaction. The pressure and skin-friction spectra will be compared to other studies and a frequency scaling based on characteristic length and velocity will show that both the shock wave and the separated zone present the typical unsteady behaviour observed in similar configurations. The results will then be extended to an analysis of the whole flow-field, presented in section 2.3, where Fourier modes decomposition of high-speed Schlieren visualisation can be used to localise the zone of the flow that is affected by low- and medium-frequency motions, whilst correlation maps will indicate the spatial structure of the unsteadiness. These results will be compared to those of the stability analysis of the next chapters.

2.1 PIV investigation

Particle Image Velocimetry (PIV) has become an essential tool in fluid measurements and is therefore widely used in industrial as well as academic situations. However, it has some limitations, such as the time necessary to compute the vector fields from

the images, or the spatial resolution linked to the windows interrogation size and the difficulty to characterise flow-fields where both high and low values of velocity are present. In that respect, over the last decade, high speed dual-PIV (Souverein et al., 2009), multi laser multi camera systems (Hou et al., 2002) or dense PIV based on GPU's (Champagnat et al., 2011) as FOLKI-PIV[1] have been developed in order to overcome the typical PIV limitations.

Since its invention, the PIV technique has become a tool widely used for incompressible flow investigations. When studying phenomena at high Mach number, the effects of compressibility bring with them technical problems such as seeding, optical access through the wind tunnel windows or lighting. As result of the advances in laser and digital imaging technology, in the last decade PIV has been applied to a variety of typical compressible flows, ranging from transonic to hypersonic configuration with and without shock waves. According to Hadjadj and Dussauge (2009), the SWBLI problems can be divided into three families: the transonic shock-boundary layer separation, the oblique shock impinging turbulent boundary layer and supersonic flow over a compression ramp. To the authors knowledge, the PIV technique has been widely applied to compression ramps (Schrijer et al., 2006; Ganapathisubramani et al., 2007) and impinging shock wave interaction (Hou et al., 2003; Humble et al., 2007; Dupont et al., 2008; van Oudheusden et al., 2011): few PIV studies (Hartmann et al., 2011) have been applied to a transonic interaction with a strong shock wave that causes massive separation of the boundary layer. Even considering LDV investigation (Délery, 1978; Muller et al., 2001), a deeper physical understanding is still needed for this particular case that presents the additional disadvantage that, in the same field, a supersonic, a high subsonic and a low speed reverse flow zones coexist. From a technical point of view, the presence of high turbulence levels due to the separation of the boundary layer can cause seeding problems that arise in addition to the classical complications arising in supersonic flow PIV.

The purpose of the present section is thus to investigate by means of PIV the transonic SWBLI previously introduced, using the capability of the recently developed software FOLKI-PIV (Champagnat et al., 2011). An important effort has been made to discuss all the hypotheses of the study: the two-dimensionality assumption of the flow is verified using multi plane PIV inspection, the repeatability of the measurements is assured by an air dryer to exclude any displacement of the shock in different test runs, the seeding system is described and a particle-response assessment is presented to show the fidelity of the tracer for the measurement conditions. The whole mean velocity field is discussed in details, providing a wide analysis of the interaction, the recirculating bubble and the velocity profiles in the mixing layer.

[1]French acronym for Iterative Lucas-Kanade Optical Flow.

By analysing the velocity fluctuations, an analysis of the statistical properties has been accomplished in order to qualify the turbulent flow field and its anisotropic behaviour. Finally, a zoom in the vicinity of the wall shows the main properties of the flow, and both mean velocity and turbulent profiles are discussed for a transonic boundary layer upstream of the shock wave.

2.1.1 PIV system

All the presented results stem from a 2C PIV investigation: the two velocity components observed are the horizontal along x, and the vertical along y. Measurements are thus performed along a plane located in the middle of the wind tunnel test section (see figure 2.3), where the three dimensional effects due to side walls are less pronounced. The test section is supposed to be wide enough to justify the neglect of the wall effects studied by Bruce et al. (2011). A multi planar evaluation was performed to assess the uniformity of the flow in the span-wise direction. The laser sheet plane was displaced a few millimetres from the middle of the wind tunnel, and the resulting velocity field for different laser positions were compared to each other: since no significant differences were observed between the resulting fields, one concludes that the two-dimensionality assumption of the flow is correct. The absence of non-uniform span-wise effects in the centre of the wind tunnel can be confirmed also by the oil flow visualisation in figure 2.4a which shows that the 3D effects are not negligible only near the side walls of the test section.

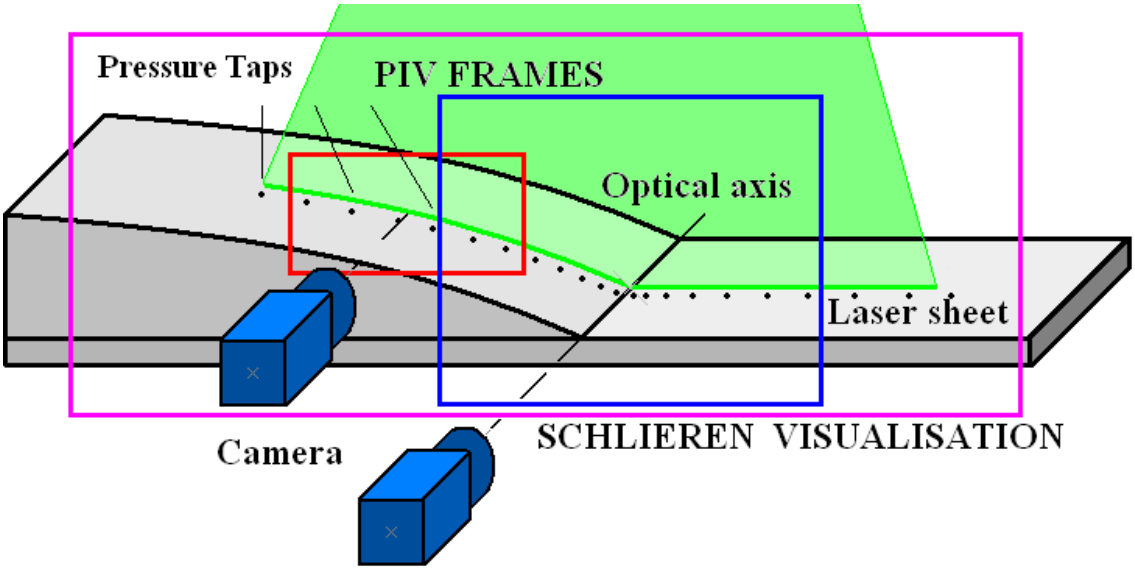

Figure 2.3: Scheme of the experimental apparatus.

The light sheets are generated by a double pulse ND:YAG laser, which delivers 150mJ per pulse. The access for the laser light is provided by a window on the top

wall of the wind tunnel, so that the light source direction is towards the decreasing y direction: this configuration remains unchanged for both the PIV investigation hereafter referred as global field and boundary layer investigation. Laser pulse separations are 2.5 μs for the global fields and 1.5 μs for the zoom on the boundary layer. 1000 image pairs are acquired at 5.6 Hz and less than 4 minutes were sufficient to record the data. A statistical assessment was performed to verify the convergence of the mean field for the number of samples considered. The camera is equipped with a lens of focal length of 105 mm for the global field, and a telecentric lens for the boundary layer; as the CCD is 2048 $\times$ 2048 pixels, the resulting magnification ratio is around 20 pixels/mm and 37 pixels/mm for the two different cases.

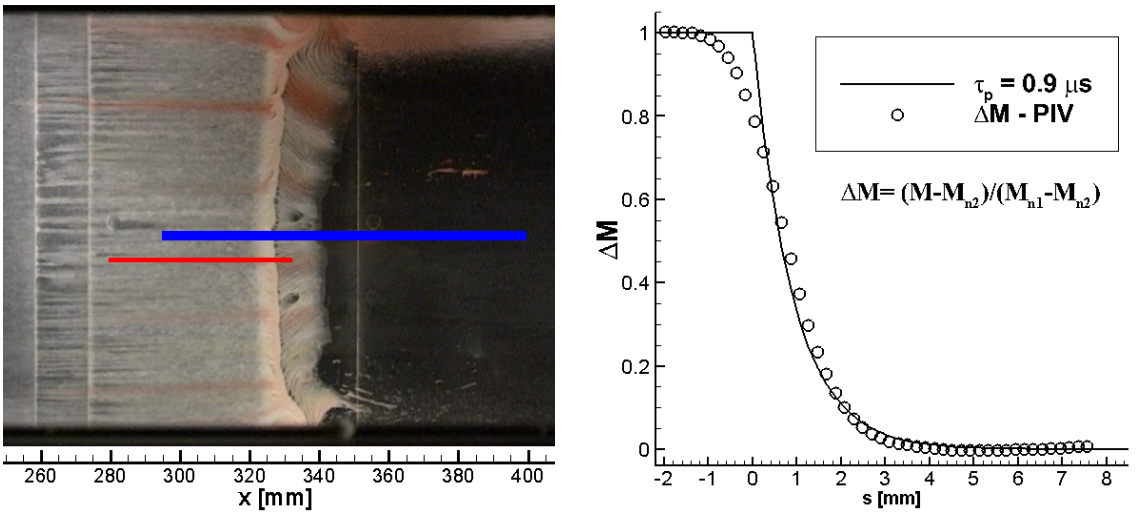

(a) Oil flow visualisation (top view, flow coming from the left). The lines identify the laser sheet positions for the two investigations.

(b) Particle response to the shock wave: normal Mach number vs local abscissa s.

Figure 2.4: Oil flow visualisations (view from the top) and Stokes number appraisal.

The parameter that mostly affects the results is the size of the interrogation window: this window must be sufficiently large to contain enough particles for the correlation, but the smaller it is the more detailed are the results, since each interrogation window returns a vector as result. In our case, the resulting field has one vector each 20 pixels, that means one vector each millimetre: each field presented had at least 100×100 vectors. For the zoom on the boundary layer the interrogation window is 10 pixels, thus the field presents 200×200 vectors, and considering the different magnification ratio, we obtain one vector every 300 μm.

Seeding

Flow seeding is a critical aspect of PIV in high-speed flows. Moreover, due to the presence of a large zone of boundary layer separation with reverse flow, the pollution on the lateral windows progressively perturbs the flow measurements. The most effective solution for the tracer in the present case is thus the use of liquid particles of Di-Ethyl-Hexyl-Sebacat (DEHS), produced by an atomiser aerosol generator[2], not only because the ease of use, but also because the liquid film that gradually settles on the windows is less "opaque" than a deposit of particles as the incense or the titanium dioxide, which are commonly used in supersonic PIV.

The DEHS oil injected has a density of about $\rho_p = 900$ kg/m^3 and a typical particle size of about $d_p = 0.5$ μm. The characteristic particle response time is derived from Stokes law for spherical particles as:

$$\tau_p = \frac{\rho_p {d_p}^2}{18\mu} = 0.7\mu s \tag{2.1}$$

where μ is the dynamic viscosity of the fluid. Considering a characteristic time of the incoming flow given by:

$$\tau_f = \frac{\delta}{U_\infty} \approx 10\mu s \tag{2.2}$$

the resulting Stokes number is:

$$S_t = \frac{\tau_p}{\tau_f} \approx 0.07 \tag{2.3}$$

The profile of the Mach number across the shock wave is shown against the local abscissa s in figure 2.4b: $s = 0$ indicates the shock position, and s is normal to the shock wave. As a particle passes through the shock, its normal Mach number M_n decreases from M_{n1} to M_{n2}. ΔM indicates the jump in the normal Mach number through the shock wave, defined as

$$\Delta M = \frac{M - M_{n2}}{M_{n1} - M_{n2}} \tag{2.4}$$

ΔM is normalised so that before the shock $\Delta M = 1$ and after $\Delta M = 0$. The experimental data profile (circles in figure 2.4b) indicates that there is a lag in the particle spatial response due to the inertial effect of the tracers. The particle relaxation time can also be estimated from an exponential fit of the post-shock particle response: as indicated in figure 2.4b, this leads to a particle response time $\tau_p = 0.9\mu s$, slightly larger than the theoretical estimation (2.1) because of the particle agglomeration (Ragni et al., 2011). According to Samimy and Lele (1991), in a compressible flow the particle slip is fully negligible if the particle Stokes number is $S_t < 0.1$ so both the

[2]Topas Gmbh ATM 210.

experimental measurements and the exponential fit referred to our seeding system indicate that the particle response lag is within the limit of a PIV study.

The particle injection system plays an important role in the PIV image quality achieved. Seeding by multi-hole pipes or bent-probe just upstream of the test section were soon discarded for stability and homogeneity reasons. To achieve the most regular seeding without a probe, it is convenient to place the particle generator far upstream of the test chamber, so that the tracers concentration in the flow can homogenise and create a uniform cloud of particles. To do so, the seeding system was placed between the air dryer and the plenum chamber, in a low speed zone. As the wind tunnel stagnation pressure is less than atmospheric, the particles were naturally sucked into the flow.

PIV images processing

As previously mentioned, in the present paper the image processing does not rely on a classical FFT based PIV software but on an iterative gradient-based cross-correlation optimisation algorithm. The reader is referred to Champagnat et al. (2011) for a complete explanation of the software FOLKI-PIV. The PIV computation is about 50 times faster[3] than a classical FFT-PIV algorithm, but the most important quality of FOLKI-PIV is its capability to recognise a particle displacement regardless if it is of a fraction of pixel or hundreds of pixels. Imposing a displacement of 30 pixels for a couple of images in the supersonic zone, yields a movement of at least 2 pixels in the separation bubble, where the speeds are about $\pm$ 20 m/s. Even assuming a sensitivity of 0.1 pixels (as traditionally done in PIV (Raffel, 2007)), we can detect velocities of 1 m/s, which is satisfying even for a subsonic field and more accurate than the other studies in literature (Dupont et al., 2008; Humble et al., 2007).

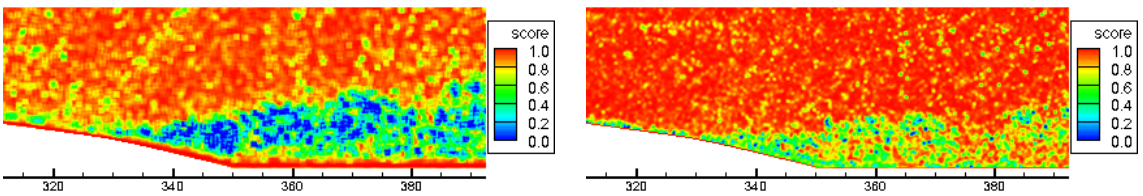

(a) Time between laser pulses = 3.5 μs.

(b) Time between laser pulses = 2.5 μs.

Figure 2.5: Score fields for different times between images. Figure (a): the particle displacement is too big, some trace particles have exited the PIV image. Figure (b): sufficient correlation everywhere in the field.

[3]With images of 2048 $\times$ 2048 pixels and a TESLA C1060 - 4Gb memory, less than 1 second is required to process one image.

A limit of the separation time between two laser pulses is the condition that the same tracer must be present in two successive images: as described in Champagnat et al. (2011), to determine how many particles exited from the laser sheet, it is sufficient to look at the score field of the results, which is a number between 0 and 1 that represent the Zero Normalised Sum Squared Differences (SSD). If the score is more than 0.3, we can trust the result of the SSD calculation. An example of a score field is represented in figure 2.5: if some particles enter or leave the laser sheet because of span-wise velocity in a zone where the three dimensional effects due to the boundary layer detachment are more pronounced, FOLKI-PIV fails to make the calculation of correlation, and then responds with a low score. Experimental tests have shown that the best compromise between sensitivity and correlation corresponds to a particle displacement of about 30 pixels in the supersonic zone. Finally, the histogram of the velocity field indicates that there is no concentration in integer pixel displacement: the peak locking problem is minimised using a sub-pixel interpolation and to the scattered light of each particle, that is in the region of 2 - 6 pixels across on the image.

2.1.2 Shock-induced separation region

In this PIV investigation, the global field of view is about 100 mm large and is horizontally centred on the downstream end of the bump ($x = 351.4$ mm): in the reference coordinate system, the resulting field ranges from $x = 300$ mm to $x = 400$ mm.

Figure 2.6 shows the structure of the shock as observed in the Schlieren visualisation of figure 2.2, and the supersonic tongue (Délery and Marvin, 1986) is delimited by the $M = 1$ isocontour line. The separation bubble, characterised by negative values of the longitudinal velocity, is the direct consequence of the boundary layer separation. A zoom in that area, shown in figure 2.7, where there also are velocity vectors, shows the presence of the separation bubble, which starts at the shock foot and extends up to $x \approx 378$ mm. Note that the vectors have been decimated, the result field being more dense. The presence of such a recirculating zone could have been inferred from the Schlieren image in figure 2.2: close to the wall, starting from $x \approx 330$ mm and until $x \approx 380$ mm, there is a zone where the turbulent structures that start from the shock foot are no more visible.

Figure 2.7 illustrates the complexity of the flow to be measured: while the bulk flow is supersonic, we also aim at characterising a recirculating bubble that presents limited values of velocity, one order of magnitude smaller than the outer field. With FOLKI-PIV and its multi-resolution framework, this can be done on the same image pair, without the need to acquire additional images focusing on the recirculating

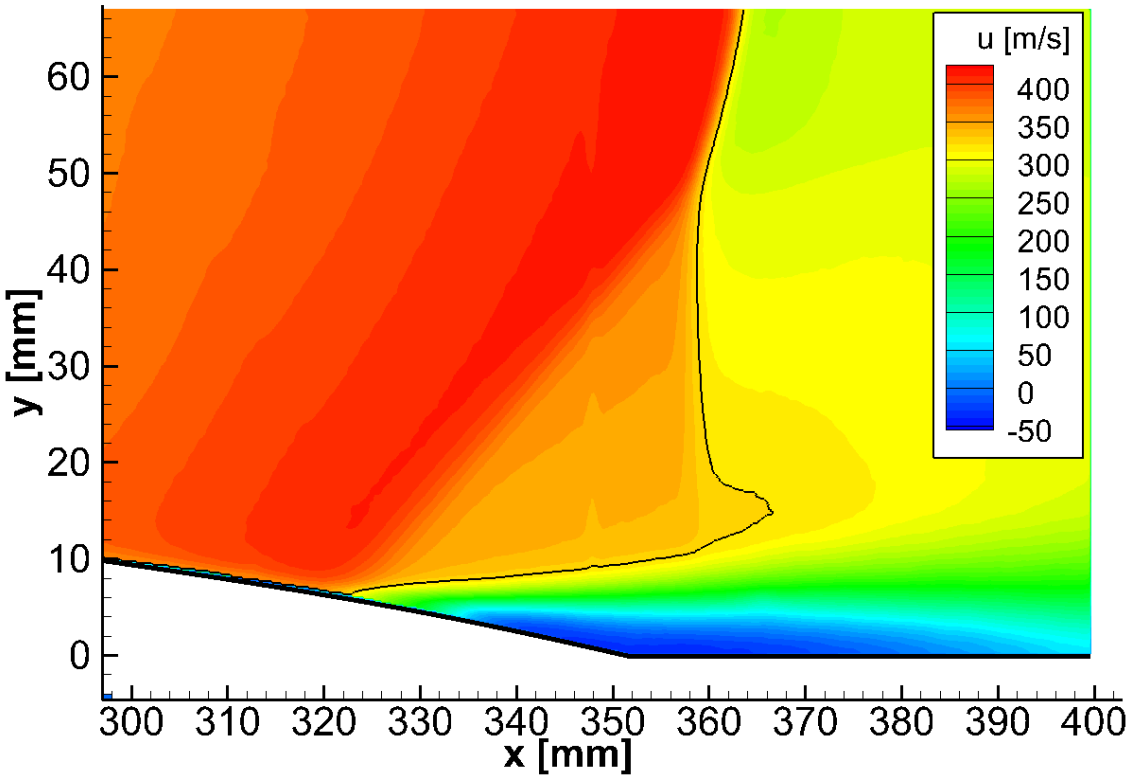

Figure 2.6: Iso-contours of the horizontal velocity component for the global field investigation. $M = 1$ solid black line.

bubble. To the authors knowledge, a transonic PIV with an accuracy of 1 m/s (with a sub-pixel refinement of 0.1 pixel at worst) has never been reported. Unfortunately, in the considered SWBLI, the boundary layer thickness is so small that its dynamics cannot be entirely detected by the spatial resolution of the global field investigation: in this result we dispose of one vector per millimetre, not sufficient to characterise the boundary layer property. For that reason the boundary layer investigation has been made with a special camera lens as explained in subsection 2.1.3.

Far away from the wall, the velocity field can describe the flow properties in a more accurate way than other studies: PIV results of the current investigation have higher spatial resolution and sensitivity than in previous studies. Figure 2.8 presents a comparison with LDV results obtained by Délery (1983). The geometrical configuration is the same in the two studies, but the nominal Mach number presents a slight difference. In a transonic interaction over a bump, the Mach number determines the shock position, tightly linked to the separation point of the boundary layer: a small difference in the Mach number can cause a shift of the shock foot location along the bump, which results in a displacement of the separating point. Besides that, the centre of the recirculating bubble is the same for the two cases, and for that reason we discuss the profiles inside both of the recirculating bubbles.

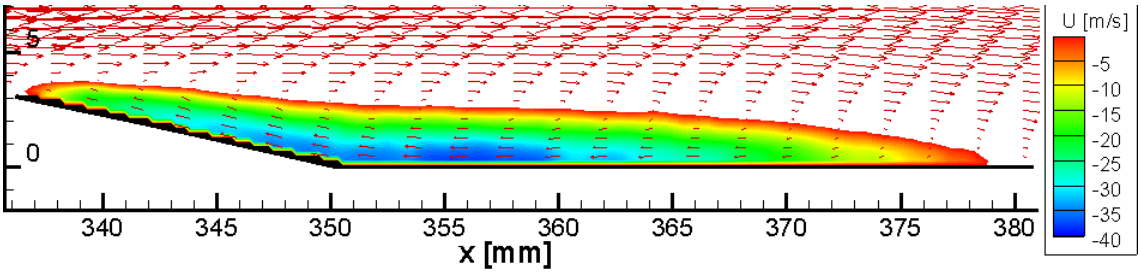

Figure 2.7: Mean velocity field, zoom on the separation bubble. Iso-contours correspond to the horizontal velocity component; Velocity vectors are down-sampled in horizontal direction, showing 1 out of 5 for clarity.

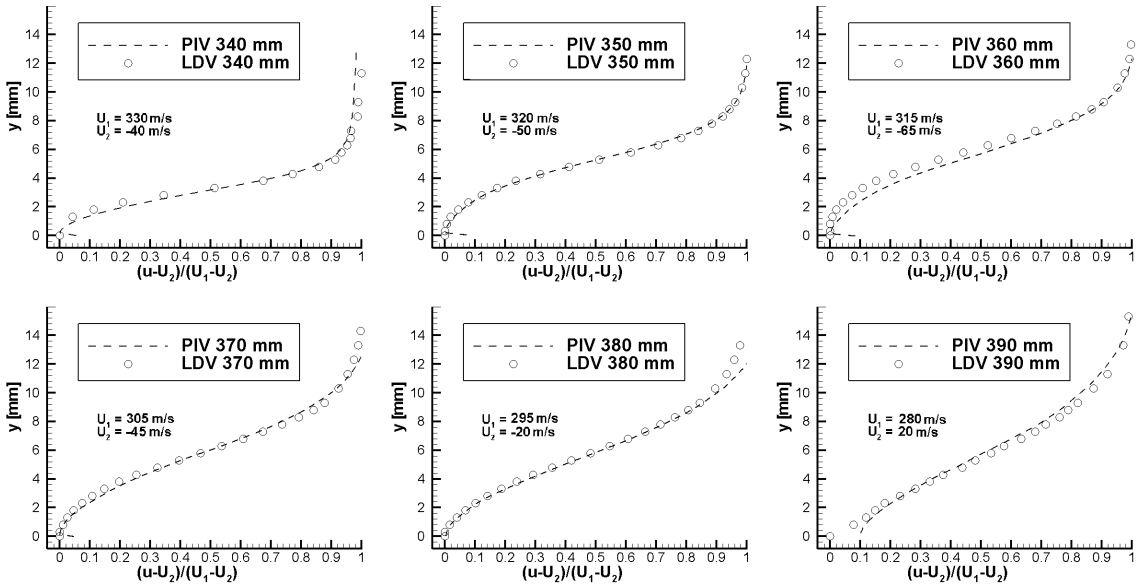

Figure 2.8: Comparison of mean velocity profiles inside the recirculating bubble, PIV data of the present study and LDV data of Délery (1983).

Following the lines of Piponniau et al. (2009), the profiles presented in figure 2.8 are given by $\frac{u-U_2}{U_1-U_2}$, where U_1 is the external velocity of each profile and U_2 is the highest in amplitude negative velocity inside the recirculation bubble. Such a presentation enables us to highlight the slight differences obtained with the two measurement techniques. Note that the velocity U_1 is different for each profile because the recirculating bubble is beneath the lambda shock inside the supersonic tongue, in a zone where the external velocity highly depends on the stream-wise position.

Figure 2.8 describes the velocity profiles along the vertical abscissa, from the separation point to the end of the recirculating zone. As indicated in the figure, the external velocity U_1 decreases constantly as progressing in the downstream direction. Meanwhile, the y position at which this external velocity is reached increases,

starting from $y = 6$ mm for the profile at $x = 340$ mm and attaining values up to $y = 16$ mm when considering the last profile. Regarding the internal velocity U_2, its value decreases as approaching the centre of the bubble, situated approximately at $x = 355$ mm and then begins to rise. The positive value of U_2 in the last profile indicates that the end of the recirculating zone is between $x = 380$ mm and $x = 390$ mm. Note that the boundary layer is not visible with the LDV measurements because of the low spatial resolution, whilst the dashed line, pertaining to the PIV measurements, shows in the very first part of the profile a gradual transition from the minimal LDV measured velocity U_2 to $u = 0$.

All the mean velocity profiles are very similar and resemble those observed in subsonic separated flows by Kiya and Sasaki (1983). They exhibit a quasi-linear behaviour in the central region, from $y = 4$ mm to $y = 8$ mm, where large convective eddies due to the Kelvin-Helmholtz instability develop and are shed downstream. The slope of this linear region decreases in the downstream direction from $x = 340$ mm to $x = 390$ mm, indicating an increase of the mixing layer thickness, that can be evaluated from

$$\delta_\omega(x) = \frac{U_1(x) - U_2(x)}{\partial u(x,y)/\partial y} \tag{2.5}$$

Such result can be used to give an appraisal of the spreading rate of the mixing layer, given by $\delta'_\omega = \delta_\omega(x)/x$. This quantity is found to be constant and equal to $\delta'_\omega \approx 0.105$. The value is not in good agreement with the spreading rate of the mixing layer proposed by Papamoschou and Roshko (1988) for the compressible turbulent shear layer, probably because the spreading rate is not correctly evaluated using the small-field obtained with the PIV investigation.

Turbulence properties evolution in the interaction region

The FOLKI-PIV software provides the r.m.s of the horizontal and vertical velocity fluctuation components. From these quantities one can derive the turbulent kinetic energy and the Reynolds shear stresses, that read for our two-dimensional study:

$$k = \frac{1}{2}(\overline{u'^2} + \overline{v'^2}) \quad \text{and} \quad R_{12} = -\overline{u'v'} \tag{2.6}$$

The evolution of the first quantity, normalised with the characteristic velocity $U_\infty = 300$ m/s, is presented in figure 2.9. The field shows that the turbulent kinetic energy is strongest in the shear layer, above the recirculating zone: this region also corresponds to the area where the medium scale turbulent structures are most evident in figure 2.2. Once k has achieved its maximum value, it rapidly decays, suggesting a redistribution of the fluctuations on all the components of velocity. Beneath the shear layer, from $x = 340$ mm to $x = 360$ mm, a low-level turbulence

zone indicates that the recirculating bubble presents a uniform recirculation at the end of the bump, characterised by a constant reverse flow.

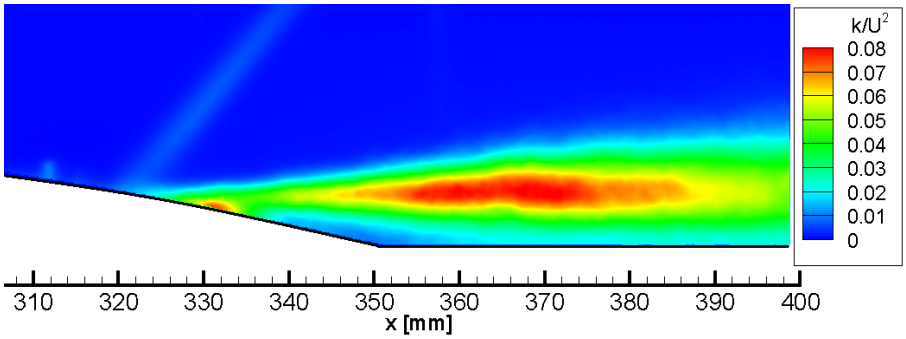

Figure 2.9: Evolution of the 2D turbulent kinetic energy k normalised with U_∞^2.

It is worthwhile to say that the strong values of k on the bump just downstream of the shock foot (from $x = 330$ mm to $x = 335$ mm) is deemed to be a small blemish: this spot is due to a heap of tracer, that forms a drop of oil which remains between the window and the bump. As the laser flashes on this drop, a random reflection disturbs the PIV images, and the result is a spurious value of the velocity fluctuations. This reflection affects the results only for the interrogation windows that surround the spot.

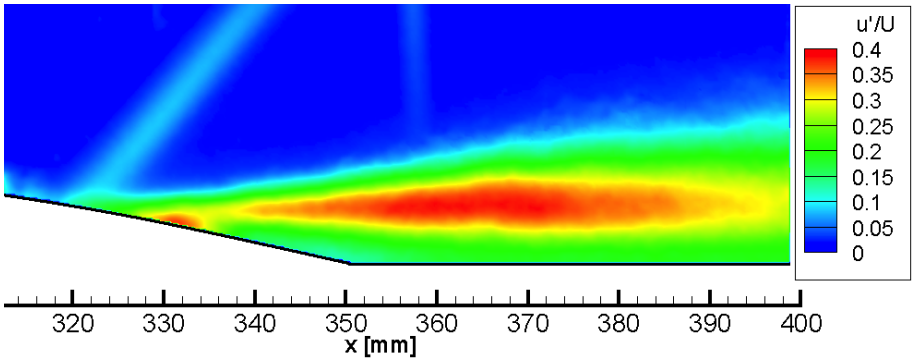

Figure 2.10: Evolution of the fluctuation for the normalised longitudinal velocity component $\sqrt{\overline{u'^2}}/U_\infty$.

To confirm the redistribution of fluctuation, it is useful to analyse separately the two components $u'/U = \sqrt{\overline{u'^2}}/U_\infty$ and $v'/U = \sqrt{\overline{v'^2}}/U_\infty$. Figures 2.10 and 2.11 show that the contribution of the longitudinal velocity is the most important (in order to see the relatively smaller values of $\sqrt{\overline{v'^2}}$, the colour-table has been changed in the two plots). The stream-wise fluctuations are three times larger than those of the vertical fluctuations.

This result is in contrast with those obtained in a plane mixing layer, where $\sqrt{\overline{u'^2}}$ is only 30% higher than $\sqrt{\overline{v'^2}}$, but similar observations are reported by Johnson et al.

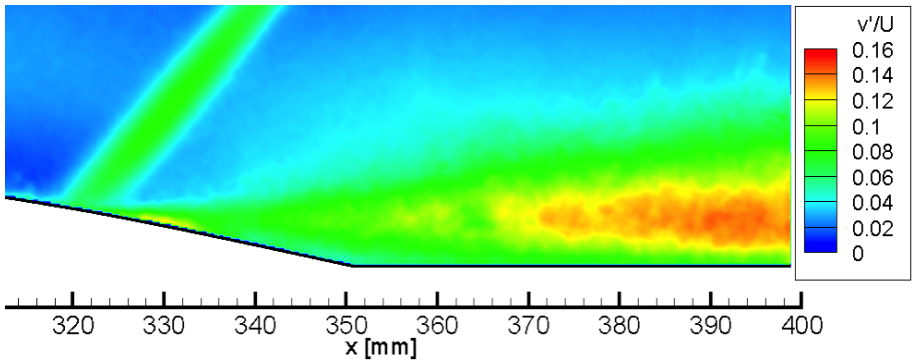

Figure 2.11: Evolution of the fluctuation for the normalised vertical velocity component $\sqrt{\overline{v'^2}}/U_\infty$.

(1981). This behaviour indicates the presence of a high turbulence anisotropy above the separation bubble. However, in the very last part of the field, where the shear layer ends and $\sqrt{\overline{v'^2}}$ achieves its maximal values, the energy is equally divided into the two fluctuation contributions. We can reasonably suppose that the decrease of the turbulent kinetic energy is due to a redistribution of the fluctuation from $\sqrt{\overline{u'^2}}$ to $\sqrt{\overline{v'^2}}$ and also to the unmeasured $\overline{w'}$, suggesting a return to isotropy.

The anisotropy of the flow plays a significant role in the turbulent production. For an incompressible flow, the production term of the $\overline{u'^2}$ transport equation is:

$$P_u = -2\overline{u'v'}\frac{\partial \overline{u}}{\partial y} - 2\overline{u'^2}\frac{\partial \overline{u}}{\partial x} \tag{2.7}$$

The results obtained are presented in figure 2.12. For the current transonic interaction the density presents a variation across the viscous layer of about $\rho_e/\rho_w = 0.85$, deemed to be small enough to neglect compressibility effects. In the first part of the interaction process the term involving the stream-wise derivative $\partial u/\partial x$ is as large as the term involving the strain rate $\partial u/\partial y$ due to the strong retardation of the whole dissipative flow: P_u is here the sum of two large positive terms. Downstream, the term involving $\partial u/\partial x$ becomes rapidly negligible. The results are in good agreement with Délery (1983). The contribution of the vertical derivative is linked to the development of the boundary layer: on the wall we can see upstream the detachment of a positive value, and in the reverse flow zone a negative value. Furthermore on the wall, downstream of the reattachment point, the production of turbulence begins to rise, suggesting the presence of a redeveloping boundary layer.

The most interesting result is the Reynolds shear stress $-\overline{u'v'}/U_\infty^2$, whose distribution is presented in figure 2.13. For compressible flows, the Reynolds shear stress is given by $-\overline{\rho}\overline{u'v'}$. However, for the transonic interaction under investigation, the change of density across the dissipative layer is small, so that $-\overline{u'v'}/U_\infty^2$ can be considered as a non dimensional Reynolds shear stress.

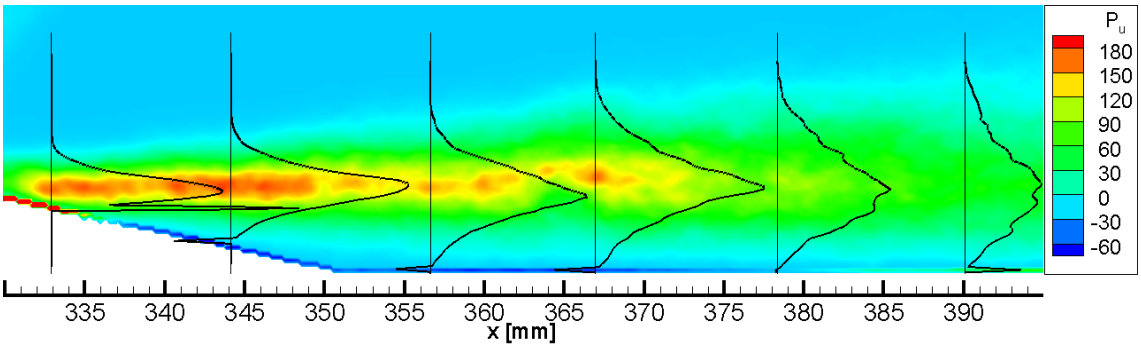

Figure 2.12: Turbulence production term of the $\sqrt{\overline{u'^2}}$ transport equation P_u.

The maximum value of the normalised turbulent shear stress is 0.023, in good agreement with the results obtained with LDV measurements (Bur et al., 2006; Délery and Marvin, 1986), where the maximal value in a similar configuration (shock in upstream position) was 0.026. Regarding the evolution in the shear layer, we can say that the maximum of the Reynolds shear stress is downstream of the recirculating zone: as suggested by Ardonceau (1984), the large values of the Reynolds shear stress imply the existence of large-scale eddies, consistent with the Schlieren visualisation of figure 2.2. In comparison to the turbulent kinetic energy, the strengthening of the shear stress appears downstream of the strengthening of k and the turbulent shear-stress reaches its maximum value downstream of the point where k culminates. For separated flows, the stream-wise location of maximum shear stress often coincides with the stream-wise location of the reattachment point (Délery, 1999), visible in figure 2.7.

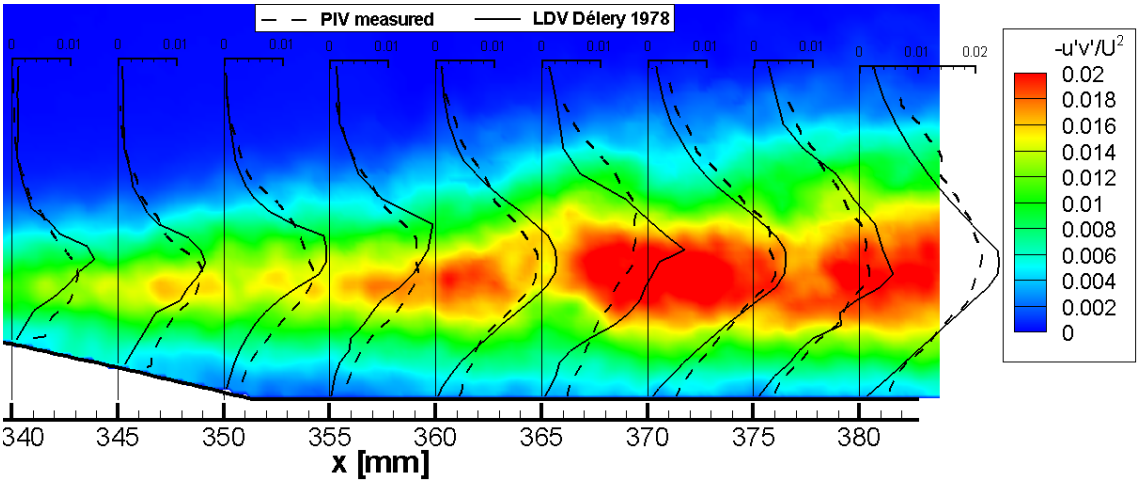

Figure 2.13: Evolution of the Reynolds shear stress $-\overline{u'v'}$, normalised with U_∞^2. Flow field and dashed line: PIV measurements (present study). Solid line: LDV measurements by Délery (1978).

The presence of the first branch of the lambda shock is always visible in the turbulent fields, particularly in the turbulent shear stress and in the $\sqrt{\overline{v'^2}}$ distributions: an oblique line upstream of the detachment point indicates a significant rise of the fluctuations immediately downstream of the shock wave and roughly parallel to it. These fluctuations highlight the unsteady behaviour of the leading shock. In this zone of the flow, as explained by Elsinga et al. (2005), the optical aberration effects introduced by the inhomogeneous refraction index may affect the measurements, as also observed in several other PIV studies (Humble et al., 2007; Mitchell et al., 2011). A part from the oblique line close to the shock, the results obtained for the Reynolds stress are in very good agreement with a similar study, made on the same configuration, by Délery (1978).

2.1.3 Boundary layer

This section discusses the boundary layer upstream of the shock. The results have been obtained with a particular lens, called telecentric, whose property is to filter all the oblique rays not parallel to the optical axis. This property can be exploited to reduce part of the laser reflections on the wall, whilst the light intensity of each image remains high because of the wide aperture of the objective. The resulting fields cannot be directly compared with other studies on the same configuration, because our PIV data has a much better resolution in the near wall region than the LDV measurements of Délery (1978). However, all the profiles presented below present the main features that can be observed in similar supersonic turbulent boundary layer investigations over a bump (Webster et al., 1996) or in shock reflection case (Dupont et al., 2008; Humble et al., 2007).

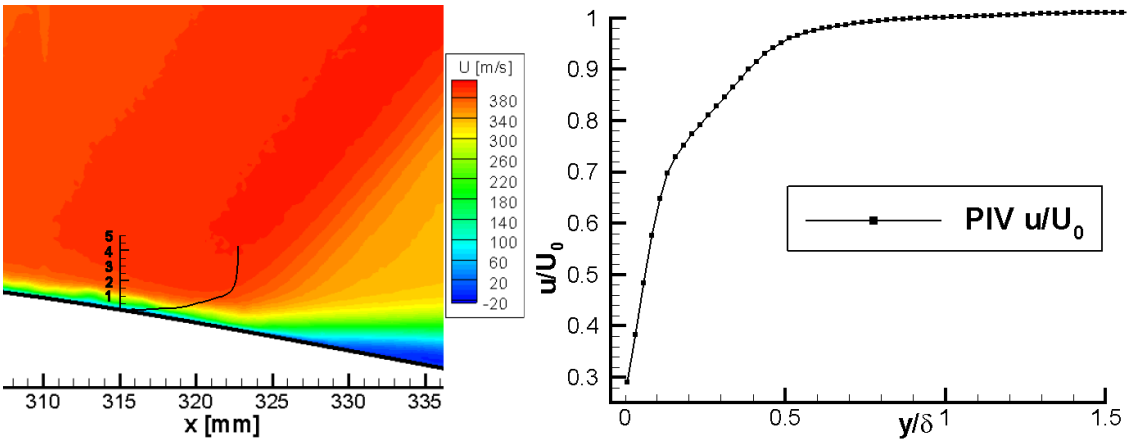

Figure 2.14: Mean longitudinal velocity measurement in the boundary layer upstream of the shock: on the left the iso contour of the mean flow and on the right a velocity profile referred to the position $x = 315$ mm.

The main problem of the present configuration is that the boundary layer is much thinner than in other similar studies. Even if the PIV system is able to measure up to 300 μm from the wall, in terms of normalised distance this means that the first reachable point is located at $y/\delta = 0.1$. In terms of non dimensional distance y^+, assuming a friction velocity of $u_\tau \approx 20$ m/s, the first PIV point is at $y^+ = 100$, but a departure of the experimental data from the profile expected from a classical boundary layer profile can be observed as soon as $y^+ > 200$. Notwithstanding, the spatial resolution and the wall approach are satisfactory for boundary layer investigations.

Even though some wall approach limitations exist, the velocity field could be almost entirely characterised as shown in figure 2.14: the mean longitudinal velocity in the boundary layer upstream of the shock is measured up to the wall, even if the results can be considered rigorously accurate only down to $y/\delta = 0.1$, because of the PIV resolution. Both the mean velocity and the turbulent profiles presented in this subsection have been extracted at $x = 315$ mm, the mean velocity has been normalised with the external bulk velocity, denoted with U_0, whose value upstream of the shock is about $U_0 = 380$ m/s. To compare turbulence results with those of the interaction investigation, the velocity fluctuations profiles have been normalised with the same U_∞ as the one used in the previous subsection.

Figure 2.15 presents a comparison between the two components of the velocity fluctuations. In this region, the boundary layer is not in equilibrium, and close to the separation. A comparison with other studies on a flat plate configuration such as Dupont et al. (2008) or Lapsa and Dahm (2011) is not possible. However, some qualitative remarks can be done: for the longitudinal velocity fluctuations, the region of high levels of turbulence starts near the wall and reaches its maximal values of $U_\infty/10$ at $y/\delta = 0.1$. The near wall peak described in figure 2.15 cannot be considered completely resolved because, as mentioned before, the first measurable point is located at $y/\delta = 0.1$. Nevertheless, we included in the plot a point at $y/\delta = 0.04$ even if this point is probably linked to an interpolation process between the point $u' = 0$ at the wall and the first completely accurate point at $y/\delta = 0.1$. To the authors knowledge, PIV measurements of a turbulent boundary layer have been reported with more accuracy only by Humble et al. (2006), who considered a boundary layer almost 10 times thicker, or more recently by Lapsa and Dahm (2011) but in a configuration with a supersonic flow without shock wave.

The near wall peak extends up to $y/\delta = 0.3$ and then the velocity fluctuations decrease constantly through the boundary layer. Concerning the vertical component v'/U, the maximum value attained is around $\sqrt{\overline{v'^2}}/U_0 = 0.03$ at $y/\delta = 0.2$, smaller than in the horizontal component. Both components reach their free-stream value

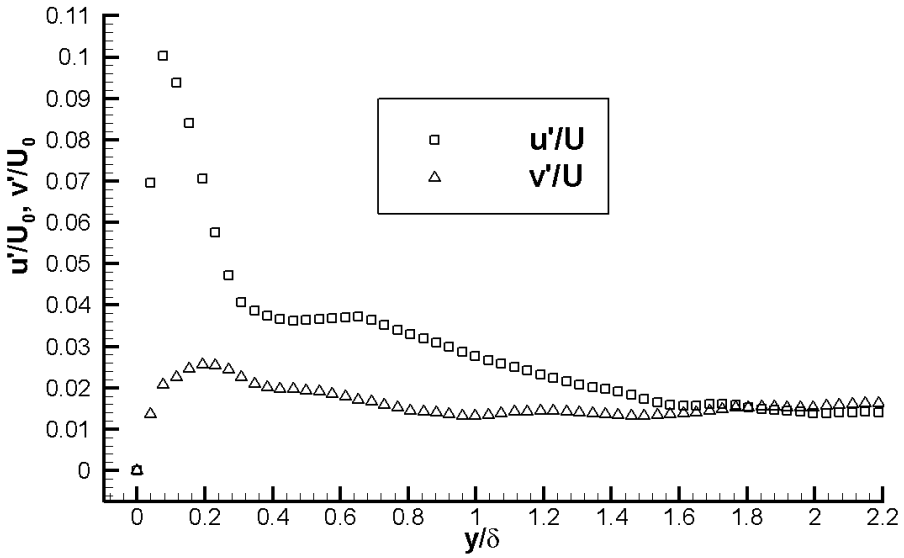

Figure 2.15: Velocity fluctuations in the boundary layer upstream of the shock.

around 0.02 starting from $y/\delta = 2$. This value is more likely the noise added by the PIV technique rather than the turbulence level of the wind tunnel.

To perform an accurate comparison with other configuration, more data are necessary. Moreover, the Morkovin representation (Elena and LaCharme, 1988) should be used, where the fluctuations are normalised using the friction velocity. However, the available data are not enough detailed to perform such comparison, so the main conclusion is that the PIV investigation in the boundary layer gives reasonable results (Dupont 2013, private communications).

2.2 Unsteadiness at the wall

In this section we characterise low- and medium-frequency fluctuations using sensors placed at the lower wall of the wind tunnel (the positions of the sensors are given in figure 2.16). Both Kulite and Hot-film sensors are used, giving access to pressure and skin-friction fluctuations, respectively.

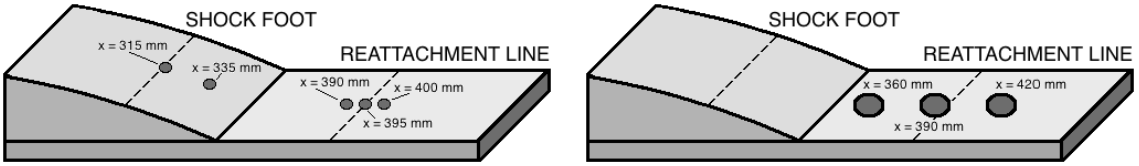

(a) Kulite sensors.

(b) Hot-Film sensors.

Figure 2.16: Sensors position on the bump.

The output was amplified and digitised at a sampling frequency of 100 kHz,

then Fourier analysis has been performed using 50% overlap and a Hanning window function, providing spectra using 500 blocks of 32768 samples each. This yields, for every spectrum and for both measurement techniques, a frequency resolution of $f = 3$ Hz. As it will be shown in the next section, the unsteadiness is not very energetic: for that reason, the use of 500 blocks to perform averaging on the spectra has been used to smooth the results. Figure 2.17 shows the effect of the number of blocks on a Kulite spectra at the shock foot: for this particular configuration, the use of 500 blocks (instead of 32 or 64, as commonly used) is required to converge the spectra.

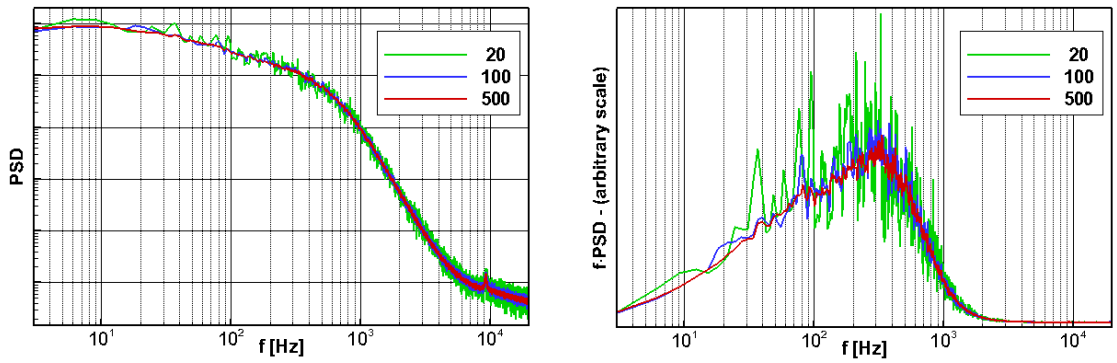

(a) Power Spectral Density.

(b) Premultiplied spectrum.

Figure 2.17: Effect of the number of blocks on the spectra.

Figure 2.17 presents another representation of the frequency content, called *weighted PSD*. When a spectrum does not present any peaks but only some bumps where the spectral density is higher than in other zones, it is usual to use this representation, where the product between the power spectral density and the frequency f is represented as a function of the log of the frequency.

$$E = \int \mathrm{PSD}\, df = \int \mathrm{PSD}\, f\, d\ln(f) \tag{2.8}$$

This representation, often called premultiplied spectrum, gives access to the frequency content of the energy fluctuations as the area below this curve.

2.2.1 Pressure fluctuations

Pressure fluctuations are investigated using high-frequency response pressure transducers[4] following the work of Dupont et al. (2006). As represented in figure 2.16, all the sensors were located on the lower wall of the test section: one at the shock foot ($x = 315$ mm), one inside the recirculating bubble on the bump ($x = 335$ mm), one

[4]Kulite series XCQ-093-15A, XCS-093-15D and XCS-093-5D.

on the reattachment point ($x = 395$ mm), and two next to it, respectively at $x = 390$ mm and $x = 400$ mm. The pressure range is 0-350 mbar and 0-1 bar, depending on the chosen pressure transducer, and the bandwidth of all transducers is around 20 kHz, sufficient to measure both low- and medium-frequency unsteadiness of the shock and the separated zone.

As shown in figure 2.18a, the spectra obtained indicate that the unsteadiness is broadband, without a single predominant peak. Moreover, all sensors display high PSD in the low-frequency range, regardless of the position. Then, depending on the distance to the shock-foot, the spectra can present a medium-frequency bump, with a power spectral density one order of magnitude lower than the one in the low-frequency zone. The high-frequency content due the turbulent structures in the boundary layer is probably at frequencies higher than 50 kHz, not measured because of the bandwidth of the sensors.

When considering the weighted PSD, represented in figure 2.18b, the pressure transducer at the shock foot indicates that most of the energy content is in the low-frequency range, whilst for the sensors in the separated zone medium-frequency motions are the most energetic, presenting a peak in the premultiplied spectra where the PSD presented a bump.

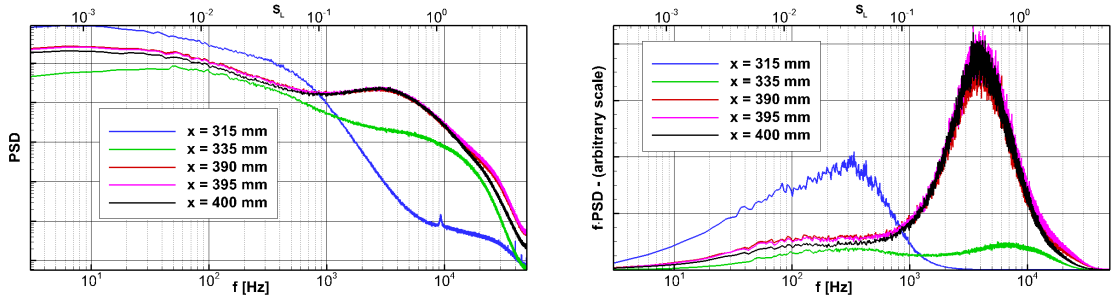

(a) Power Spectral Density.

(b) Premultiplied spectrum.

Figure 2.18: Wall-pressure fluctuations on the centreline of the test section: at the shock foot, between the separation point and the end of the bump, and around the reattachment point.

The horizontal axis of all figures present the Strouhal number, computed using equation (1.1) with a characteristic length $L = 35$ mm, corresponding to the distance between the separation point and the projection of the second shock on the wall, and a velocity of $U = 300$ m/s, corresponding to the speed of the flow above the recirculation bubble. This scaling yields, for the sensor placed at the shock foot, to a maximum of $f \cdot PSD$ around 0.04, that corresponds to a frequency of 300 Hz.

The green solid line corresponding to $x = 335$ mm in figure 2.18 indicates that the spectrum of a pressure transducer placed close to the shock just after the separation

point exhibits the low-frequency unsteadiness due to the shock but also the medium-frequency due to the mixing-layer zone. This behaviour suggests that the sensor was placed in an intermediary zone between the two separated phenomena. The last three sensors, who are placed close to the end of the separation bubble, display a very similar spectrum, indicating that pressure fluctuations inside the recirculation zone propagate downstream without change of their frequency content.

The most energetic perturbations in this zone are around 4000 Hz, that corresponds to a Strouhal number of 0.5. The scale in the premultiplied spectra of figure 2.18b are arbitrary, but the whole spectrum is known up to a multiplicative constant, and this constant is the same for all frequencies: the fact that the peak in the medium-frequency motions is more energetic than the one in the low-frequency indicates that shock motions contribute less to the total amount of unsteadiness present in the interaction. However, even if less energetic, low-frequency unsteadiness is present in the whole interaction, as indicated by figure 2.18a, where the power spectral density for low-frequency unsteadiness is high for all the sensors. Thus, even if the weighted PSD in figure 2.18b presents a peak in the low-frequency range only for the sensor at the shock foot, one can find low-frequency fluctuations even in the separated zone.

On the contrary, the PSD distribution at the separation point indicates that the shock foot present only low-frequency motions, suggesting a low-pass filter behaviour with a cut-off frequency around $f = 300 - 400$ Hz (that correspond to the peak in the weighted PSD of figure 2.18b): the shock passes low-frequency motions but attenuates all the pressure fluctuations arising from the separated zone.

2.2.2 Skin-friction fluctuations

The purpose of this investigation is to determine statistical quantities of the skin-friction fluctuations. To do that, thin metal film deposited on an electrically insulating substrate, called hot-film sensors, are used. As indicated in figure 2.16, three sensors were placed on the lower wall of the wind tunnel after the end of the bump: one inside the recirculating bubble ($x = 360$ mm), one around the end of the separated region ($x = 390$ mm) and one downstream of the recirculation bubble ($x = 420$ mm).

The sensors[5] were operated with a commercial constant temperature circuit (DISA 55M10) and the signals were amplified, digitised and processed as described in the previous section. Figure 2.19 presents the classic and weighted spectra for the three films: in all cases one can notice that, as for the Kulite measurements

[5]Glue-on probe model 55-R47. The sensor is a 0.1×0.9 mm nickel film deposited on a 0.05 mm thick polyimide foil carrying a 0.5 μm quartz coating.

downstream of the shock foot, the classic spectrum presents a high level of power spectral density in the low-frequency region, and a bump at medium-frequencies. When observing the weighted PSD, the bump is a broadband peak centred around $S_L = 0.03$, a slightly smaller value when compared to the wall-pressure fluctuations.

As for the Kulite investigation, when a sensor is placed inside the recirculation zone and close to the shock foot (solid line corresponding to $x = 360$ mm in figure 2.19) both low- and medium-frequency motions are clearly observed: the weighted spectrum presents a bump in the low-frequency range whose energy content has the same order of magnitude as medium-frequency motions. This low-frequency bump is still visible when the sensor is at the end of the recirculation zone and disappear completely for the most downstream hot-film.

Finally, the peak corresponding to $f = 50$ Hz present in all curves of figure 2.19 is a consequence of the commercial electric-power distribution system and is not linked to any physical phenomenon of the interaction.

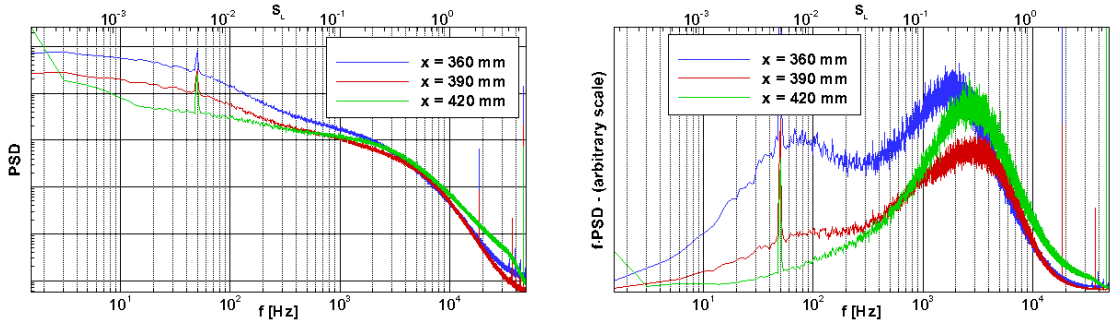

(a) Power Spectral Density.

(b) Premultiplied spectrum.

Figure 2.19: Skin-friction fluctuations on the centreline of the test section: inside the recirculation zone, at the reattachment point and after the separated zone.

As for the medium-frequency peak, the skin-friction fluctuations indicate that shock unsteadiness has a lower frequency with respect to the pressure fluctuations: the weighted PSD present a maximum value for $f = 70 - 100$ Hz when computed with Hot-films signals, whilst in the Kulite investigation of section 2.2.1 the peak was around $f = 300 - 400$ Hz. This shift is due to the different measurement technique and attenuates when considering transducers in the same position, as for medium-frequency motions: Kulite sensors indicate a maximum of premultiplied spectrum for $f = 4$ kHz, while the skin-friction measurements present a peak in $f = 3$ kHz.

Despite the small difference in the peaks of the weighted spectra, both measurement techniques confirm that this transonic SWBLI is characterised by low-frequency motions, mostly located at the shock foot but which are present also in the separated region, and medium-frequency motions, localised after the separation

point and not only limited to the recirculation zone. This observation compares favourably with all the SWBLI studies discussed in literature, and by scaling the frequency with the above mentioned characteristic length and velocity scales one can find a good agreement with other configurations in the supersonic regime such as compression ramps (Dolling and Brusniak, 1989; Wu and Martin, 2008) or shock impinging on a turbulent boundary layer (Dupont et al., 2006; Touber and Sandham, 2008).

2.3 High-speed Schlieren visualisation

Pressure and skin-friction measurements, although very reliable, are only at few points, and always located at the wall. In order to have a global description of the unsteady behaviour of the interaction, high-speed Schlieren visualisation is proposed. If Kulite measurements are too local, it has to be said that the Schlieren visualisation may suffer the opposite problem, as the image that we obtain is the span-wise integration of the light beam, so it may include three dimensional effects due for example to the boundary layers at the vertical walls of the wind tunnel. Despite the integration of these three dimensional effects that can be partially excluded by focusing the Schlieren image at the centreline of the wind tunnel, the images yield a detailed description of the unsteady behaviour of the whole interaction.

Schlieren visualisation is a technique based on the deflection of light by a refractive index, widely used to investigate the dynamics of the fluid structure. The flow index gradient is directly related to flow density gradient, and the deflected light is compared to undeflected light at a viewing screen by blocking the undisturbed light using a knife edge. The light that is deflected toward or away from the knife edge produces a shadow pattern that is a light-intensity representation of the expansions (low density regions) and compressions (high density regions) which characterise the flow. In particular, the magnitude of the observed gradient is proportional to the light intensity measured by the camera sensor: a dark point on the image corresponds to negative density gradient, whilst a bright point indicates the presence of a positive one.

A high speed camera[6] is placed on the side of the wind tunnel, and 60000 images (464×360 pixels) are recorded at 35 kHz frame rate. The magnification ratio is around 3.3 px/mm, producing an image whose length is 140 mm and spans the whole channel height. The results presented in the next sections stem from acquisitions with both horizontal and vertical knife-edge: the light intensity is proportional, respectively, to the vertical $\partial\rho/\partial y$ and horizontal $\partial\rho/\partial x$ components of the density

[6]Vision Research, Phantom V710. 7 Gpx/second throughput, 300 ns digital exposure.

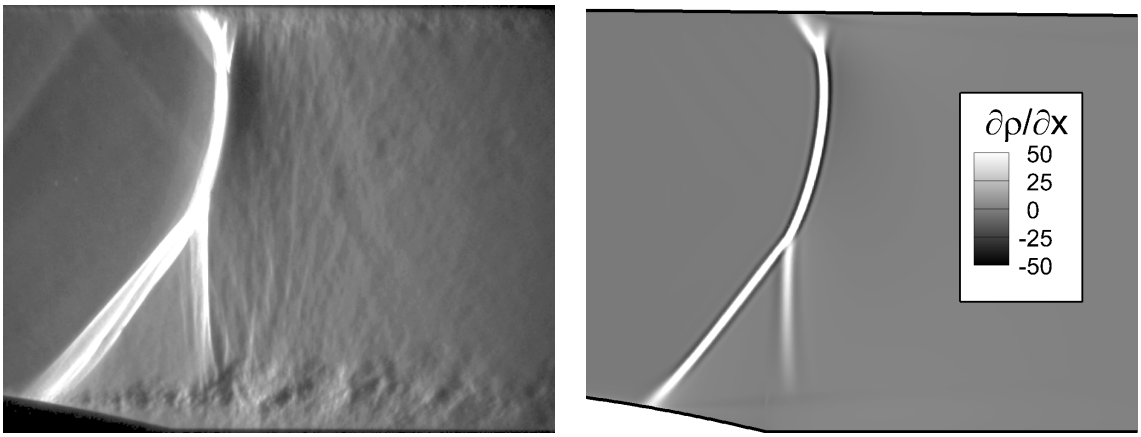

(a) $\partial\rho/\partial x$, Schlieren image. (b) $\partial\rho/\partial x$, numerical simulation.

Figure 2.20: Horizontal density gradient obtained with a Schlieren apparatus, using a vertically oriented knife edge, and by numerical simulation from chapter 3.

gradient, as represented in figures 2.20 and 2.21.

Figure 2.20a presents the horizontal density gradient, obtained with a vertically oriented knife edge: the shock wave has a positive density gradient, and is therefore white. The boundary layers are not visible, as they do not present any gradient in the stream-wise direction. The shock wave compares favourably with the density derivative in the stream-wise direction obtained from the mean flow computed in chapter 3, presented in figure 2.20b. In the instantaneous Schlieren image, the flow after the shock foot is characterised by the existence of the mixing layer, and presents a succession of positive and negative density gradients, due to the vortices that are shed from the separation point. In this zone there are the small-scale structures that are responsible for the high-frequency unsteadiness, not captured by the numerical simulation. Figure 2.20a also indicate that the mixing layer is the source of noise, whose presence can be seen under the form of Mach lines, almost vertical, that perturb the shock.

Figure 2.21a has been obtained with a horizontal edge-oriented knife: the boundary layer, that displays a positive gradient normal to the wall, is bright on the lower wall while it is dark on the upper one, corresponding to respectively positive and negative $\partial\rho/\partial y$, respectively. Considering the shock wave, the density gradient is positive in the flow direction: in almost all the channel, the vertical component of the velocity is slightly negative, due to the curvature of the bump on the lower wall. The density gradient is thus a vector whose vertical component is negative, except for the upper part of the shock (bright spot on the top of figure 2.21a). The mixing layer zone is characterised as before by a succession of small-scale structures and also, close to the shock foot, by a bright horizontal elongated zone, corresponding to

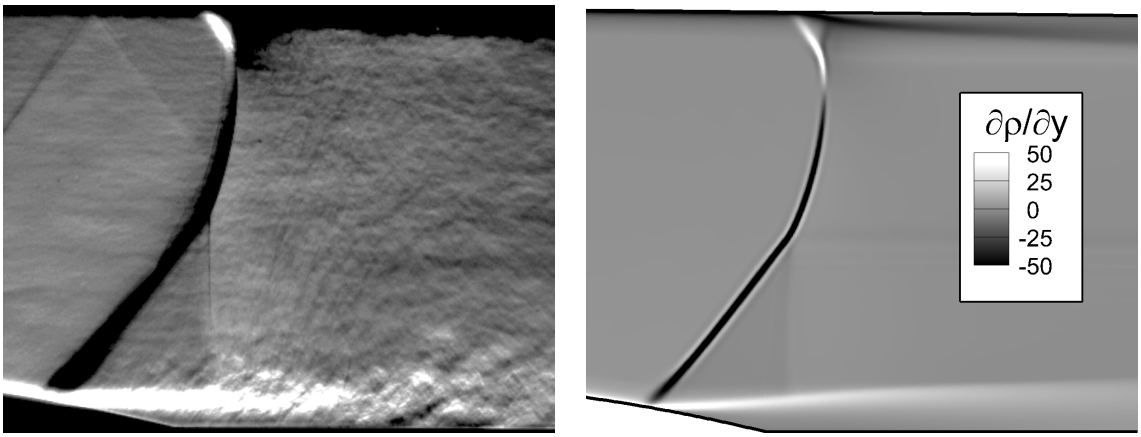

(a) $\partial\rho/\partial y$, Schlieren image. (b) $\partial\rho/\partial y$, numerical simulation.

Figure 2.21: Vertical density gradient obtained with a Schlieren apparatus, using a horizontally oriented knife edge, and by numerical simulation from chapter 3.

the mixing layer that was created by the boundary layer separation near the shock foot. This horizontal line defines clearly the extension of the separated zone. The numerical result presented in figure 2.21b confirms the presence of a shock wave almost completely characterised by a negative density gradient and the bright zone above the recirculation bubble due to the separation of the boundary layer.

In this section, we use Schlieren photography to get a better understanding of the spatial distribution of the unsteadiness of the flow, performing Fourier analysis and investigating the two-point correlations of the density gradient field on the whole image. If on one side flow-visualisation methods offer a good spatial and temporal description of the observed zone, for example giving access to 464×360 points at 35 kHz, on the other side the number of tonal values that are used to describe the light intensity is not comparable to the level of description obtained by other sensors, as for example the Kulite or hot-film sensors described in section 2.2. In our investigation the camera was equipped with a 12-bit colour depth sensor: the light intensity measured by each pixel is associated to a number between 0 and 4095. The available range is too small to describe at the same time both the strong density gradient due to the shock wave and the small density variations in the mixing layer caused by the vortex shedding. For this reason, the image often presents colour saturation, for example in figure 2.21a on the shock (black region caused by the absence of light) or at the beginning of the mixing layer (white region associated to too much light intensity). This problem can affect the results of the image processing, altering for example the Fourier modes (adding high-frequency energy in the saturated zone due to the signal truncation), or the correlation maps (showing 100% correlation because of the absence of texture in the images).

2.3.1 Fourier modes decomposition

FFT is the most important discrete transform, used to perform Fourier analysis. In image processing, the samples can be the values of pixels along a row or column of a raster image. The time resolved image sequence can be written as $I(i, j, n)$ where I is the light intensity of each image point (or pixel). In this study, i and j vary from 1 to 464 and 1 to 360, respectively, and n defines the snapshot number and varies from 1 to $N = 60000$. For a given position (i, j), the time series that represent the evolution of light intensity at a given pixel of the field can be written as $p_{ij}(n)$. Assuming a linear correspondence between light intensity and density gradient, one can compute the Fourier transform of $p_{ij}(n)$ using an FFT algorithm with Hanning window function, 60 blocks with 50% overlap of 2048 images. Due to the limited amount of data samples, the spectrum has a resolution of $f = 17$ Hz and does not present any peak; yet, relying on the informations obtained in the previous section, we consider in the following the spatial structure of a low- and a medium-frequency mode, corresponding to the peaks displayed in pressure spectrum of figure 2.18b.

Figure 2.22 shows the spatial structure of a low-frequency mode at $f = 300$ Hz, obtained with vertical and horizontal edge-oriented knives. The left side of the figure, referred to horizontal density gradient, indicates that low-frequency unsteadiness of the stream-wise density gradient is located on the whole lambda shock wave, without small scales structures after the separation point. Figure 2.22b shows the vertical density gradient associated to this low-frequency mode. It indicates that the mode has its maximum strength at the shock foot (see also upper wall shock foot), but that it is in general located on the entire shock wave pattern, mostly in the first leg, but also in the second one that forms the lambda pattern. Moreover, low-frequency fluctuations are found also in the core of the mixing layer, where the PIV investigation (section 2.1) indicates that the turbulence production has its maximal value. The absence of energy inside the shock is a consequence of the lack of light in the Schlieren images (as in figure 2.21a), and should not be interpreted as a steady region of the flow.

On both representations in figure 2.22, in the upper left side of the image two diagonal lines indicate the presence of compression waves in the supersonic zone, which are generated at the sonic throat and propagate across the flow at the Mach angle $\alpha = \sin^{-1}(1/M)$. As it will be shown by the global stability analysis, those compression waves are important in the flow dynamics because they represent the direction along which information propagates in the supersonic zone.

Figure 2.23 presents the Fourier mode at $f = 4000$ Hz, the frequency where pressure fluctuations reach their maximal value in the separated zone. On both density gradient components, the Fourier mode is located in the mixing layer region

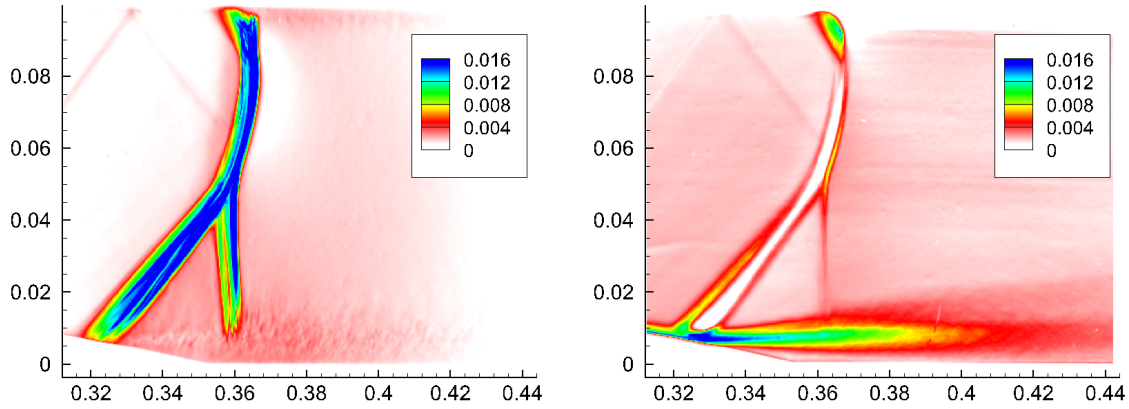

(a) Horizontal density gradient $\partial\rho/\partial x$. (b) Vertical density gradient $\partial\rho/\partial y$.

Figure 2.22: Fourier mode at low-frequency ($f = 300$ Hz) for the horizontal (a) and vertical (b) density gradient.

downstream of the separation point. Concerning the horizontal density gradient, figure 2.23a indicates the presence of some small-scale structures, located in the mixing layer. Similar structures are also visible on the upper wall. The mode shape in the shock region remains close to the shape of the low-frequency mode, with amplitudes decreased by a factor 4: this behaviour confirms results already discussed when analysing the pre-multiplied spectra obtained with wall measurements, where we observed that the strong peak observed at low-frequencies and close to the shock foot rapidly disappears as more downstream sensors are considered. Note that the energy levels change between figures 2.22 and 2.23: the maximum mode energy on the shock is 4 times lower than the energy in the low-frequency mode.

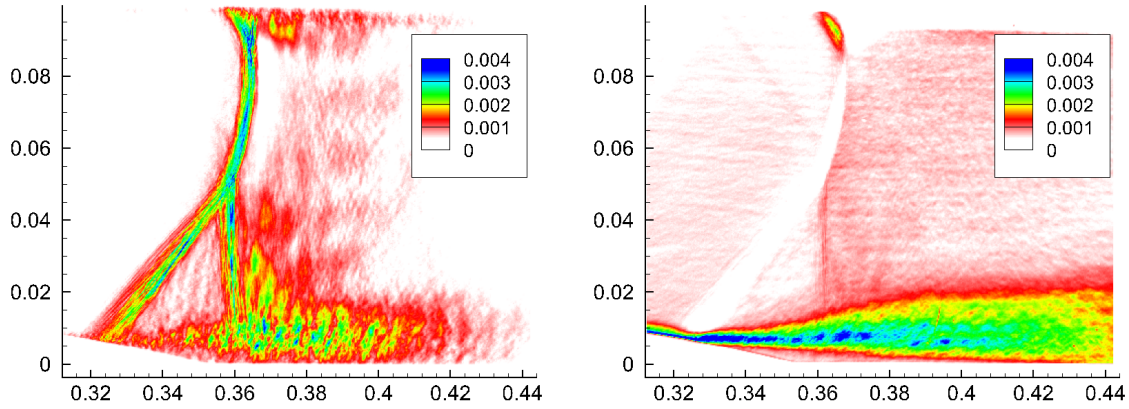

(a) Horizontal density gradient $\partial\rho/\partial x$. (b) Vertical density gradient $\partial\rho/\partial y$.

Figure 2.23: Fourier mode at medium-frequency ($f = 4000$ Hz) for the horizontal (a) and vertical (b) density gradient.

The vertical density gradient of the medium-frequency mode indicates that the most energetic fluctuations are in the mixing layer, whilst the shock does not present any medium-frequency unsteadiness at all. This result is in disagreement with what was observed in the Fourier mode decomposition of the horizontal density gradient, where medium-frequency motions were present inside the shock wave, too. This feature has been observed also in the DNS simulations of Wu and Martin (2008), who documented the presence of small-amplitude span-wise wrinkling on the shock, and by Agostini et al. (2012) in LES simulations. However, the energy in the medium-frequency Fourier mode on the shock could also come from the truncated signal due to colour saturation: the white zone in the Schlieren photography is always associated to high energy on the Fourier mode, whatever the frequency, whilst a saturated black zone corresponds to low energy. This feature can affect the result by adding non-physical mode energy: in the shock-wave region when investigating the horizontal density gradient, and the boundary layers when investigating the vertical one.

Although less detailed in frequencies, the Fourier modes decomposition confirms the presence of two characteristic modes, and indicates the spatial location of the unsteadiness: the shock wave seems to behave as a low-pass filter, displaying its maximum fluctuations at low-frequencies, even though some energy is still visible in the medium-frequency range. Low-frequency unsteadiness is located not only at the shock foot, as suggested by Kulite measurements, but also on the whole shock wave and also at the top of the recirculation bubble. This feature is not observable with wall pressure transducers and indicates that the mixing layer has energetic contributions for both low- and medium-frequencies. A similar result has recently observed in a compression ramp configuration (Grilli et al., 2012), where dynamic mode decomposition confirms the presence of a low-frequency mode associated to the pulsation of the separation bubble and accompanied by a forward-backward motion of the shock.

Medium-frequency unsteadiness is located in the mixing layer that develops after the separation point. Using LES flow fields, Pirozzoli et al. (2010b) performed a similar Fourier analysis and found a similar result in a shock-impinging supersonic configuration: the medium-frequency mode is energetic in the mixing layer that develops after the separation point. Concerning the presence of medium-frequency motions on the shock, further investigations are needed to understand if the shock behaves as a low-pass filter as indicated by the unsteady-pressure measurement in section 2.2 and by other studies (Plotkin, 1975; Touber and Sandham, 2011), or if the shock is just a mirror of the physical phenomena localised in the separated zone presenting both low- and medium-frequency motions (Wu and Martin, 2008;

Agostini et al., 2012).

2.3.2 Two-point correlations

In this section a set of $N = 20000$ images is used for analysing two-point correlations. Contrary to the analysis performed in the previous section, the correlation does not carry any information about the interaction in the frequency domain, but can give insights on the coherent structures present in the flow. As previously mentioned, the image series can be written as $I(i, j, n)$ where the light intensity of a given pixel at time n (indicated as $p_{ij}(n)$) is proportional to the horizontal or vertical flow-density gradient. If we consider another pixel on the image, whose coordinates are given by (k, l), one can compute the correlation between the time series at point (k, l), indicated as $p_{kl}(n)$, and the time series at all other points $p_{ij}(n)$. For image-processing applications where the brightness of the images varies due to lighting, the images have to be normalised by subtracting the mean and dividing them by the standard deviation. The cross correlation coefficient is given by:

$$C_{kl}(i,j) = \frac{1}{N}\sum_{n=1}^{N}\frac{\left[p_{ij}(n) - \overline{p_{ij}}\right]\left[p_{kl}(n) - \overline{p_{kl}}\right]}{\sigma_{ij}\sigma_{kl}} \tag{2.9}$$

Where $\overline{p_{ij}}$ indicates the mean value of the light intensity and σ_{ij} and σ_{kl} are the standard deviations at the pixels (i, j) and (k, l), respectively.

$$\sigma_{ij} = \sqrt{\frac{1}{N}\sum_{n=1}^{N}(p_{ij}(n) - \overline{p_{ij}})^2}$$

The result of this operation is a set of 464×360 fields that represent, for each interrogation point (k, l) the correlation map between the chosen pixel and the whole image. The approach proposed in this section consists in fixing an interrogation point, for example at the shock foot or in the mixing layer, and look at the zones of the flow where the density gradients are correlated to that point. Contrary to the correlation analyses based on wall pressure measurements (Dolling and Erengil, 1991; Dupont et al., 2006; Debiève and Dupont, 2009) or on numerical simulation data (Larchevêque et al., 2010; Touber and Sandham, 2008), the presently examined quantity is not directly linked to a physical quantity, but is just a qualitative association between light intensity and density gradient, without a calibration process.

Figures 2.24 (a) and (b) present the correlation maps for the horizontal and vertical density gradient, when the reference point is at the shock foot. On both Schlieren visualisations one can notice a strong correlation between the shock foot and the entire shock wave, suggesting that shock movements are, regardless of the frequency, rigid-body displacements centred on the shock mean position.

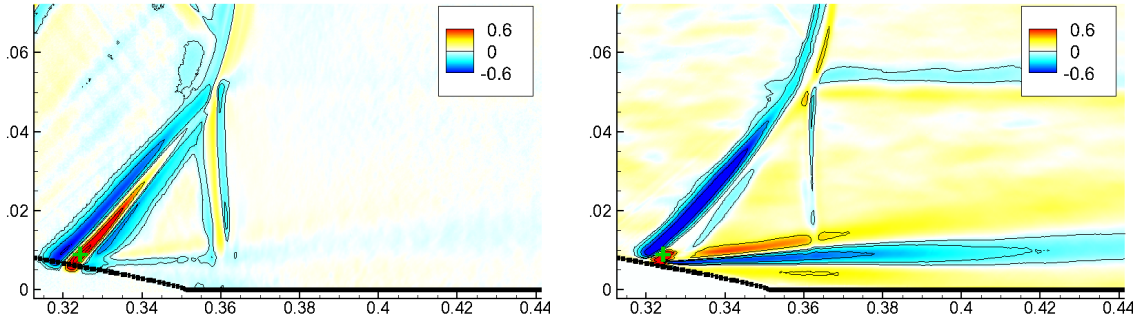

(a) Horizontal density gradient $\partial\rho/\partial x$.

(b) Vertical density gradient $\partial\rho/\partial y$.

Figure 2.24: Correlations for a reference point located at the shock foot for the horizontal (a) and vertical (b) density gradient. The correlation point is indicated by the + symbol.

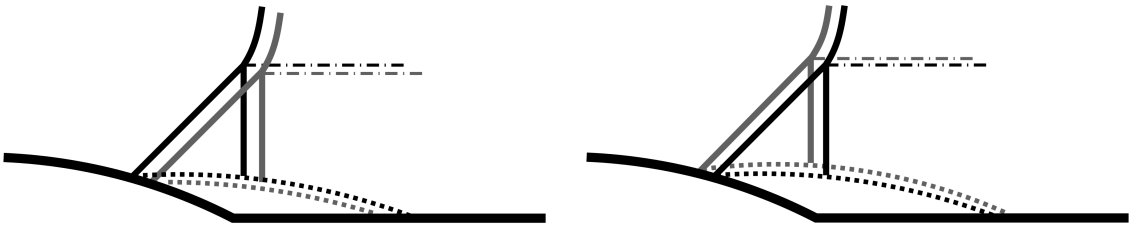

(a) Downstream displacement: smaller bubble.

(b) Upstream displacement: bigger bubble.

Figure 2.25: Relation between stream-wise shock displacements from its mean position and vertical movements of mixing layer and slip line.

The horizontally elongated regions observed in the mixing-layer in figure 2.24b indicate that shock movements are correlated to vertical displacements of the mixing layer, the separation point being located at the wall just downstream of the shock foot. Due to the bump slope, stream-wise shock movements correspond to vertical displacements of the separation point, that impact the recirculation bubble height. The consequences are contraction and expansion motions of the separated zone that were already observed with conditional analysis in a similar SWBLI: Kussoy et al. (1988) used two-component LDV to investigate a Mach number $M = 2.85$ flow past a flared cylinder. The shock wave position was determined using high-speed shadowgraph and pressure transducers. Simultaneous laser velocimetry and measurements of wall-pressure fluctuations showed that the so called breathing of the separated zone was synchronised with the motion of the front leg of the lambda-shock system.

The sketch in figure 2.25 explains how the horizontal shock displacements from its mean position are correlated to the contraction and expansion of the separated zone. This simplified model also links the stream-wise shock oscillations to the

vertical movements of the slip line, indicated by the correlation map in figure 2.24b. As this discontinuity in the flow does not display significant variations in density along the horizontal component of velocity, the slip-line unsteadiness is only visible when analysing vertical density gradients.

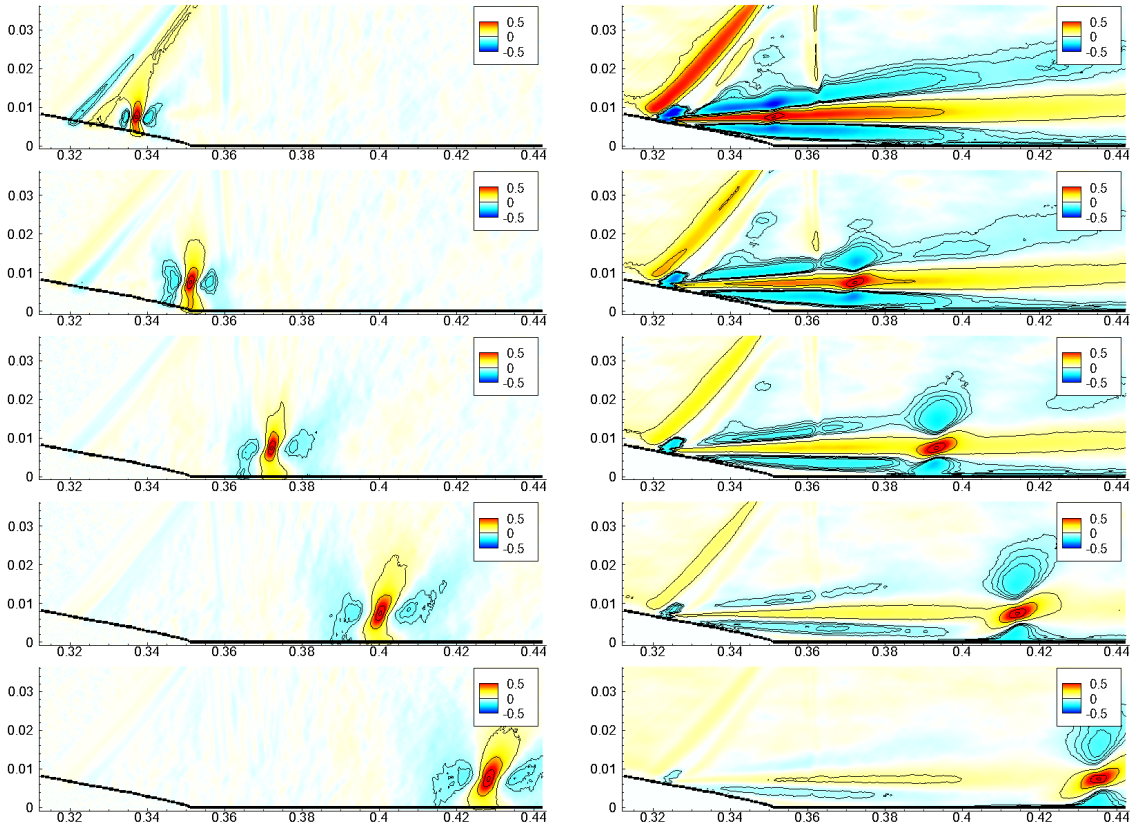

(a) Horizontal density gradient $\partial\rho/\partial x$. (b) Vertical density gradient $\partial\rho/\partial y$.

Figure 2.26: Correlations for a reference point in the mixing layer zone for the horizontal (a) and vertical (b) density gradient. The red dot indicates the correlation reference point.

The boundary layer fluctuations do not seem to be correlated to the shock or the mixing layer, even if this observation is limited by the spatial resolution of the Schlieren visualisation, that is not sufficiently accurate to investigate the small-scale structures of the incoming flow: when considering a point in the incoming boundary layer, the correlation coefficient is small everywhere in the flow except in the flow upstream the shock foot. On the contrary, when considering a point in the mixing layer, the spatial resolution of the Schlieren investigation is sufficiently detailed to correlate the vortex generated by the separation point.

Figure 2.26 presents the correlation maps for different points in the mixing layer: in this figure the reference pixel p_{kl} is always at the same vertical coordinate that

corresponds to the centreline of the mixing layer, and is moving downstream, starting from $x = 340$ mm in the figure on the top. When considering the horizontal density gradient, the correlation maps indicate the presence of large scale structures that can be linked to the vortex shedding caused by the separation point. The sketch in figure 2.27a helps understanding the horizontal density distribution caused by a vortical structure, and the effect of a fluctuation on those region. On the lower part of the image, the evolution of the density gradient is plotted for two position of the vortex. The correlation map highlights the zone in the mixing layer where we find similar density gradient distribution, due to the occurrence of a vortical structure. The result is a positive zone in the center of the vortex, where the correlation point is, flanked by two anti-correlated zone above and under the vortex. A similar behaviour can be observed in figure 2.27b where the anti-correlated zone are above and under the correlation point.

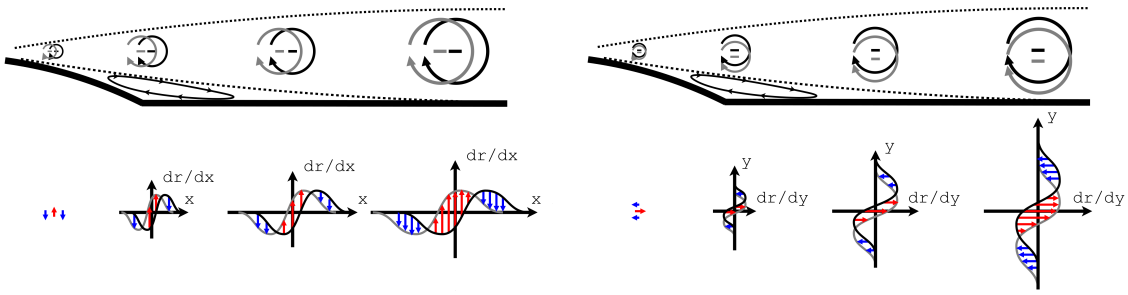

(a) Horizontal density gradient $\partial\rho/\partial x$.

(b) Vertical density gradient $\partial\rho/\partial y$.

Figure 2.27: Vertical and horizontal pressure distributions when vortical structures are shed in the mixing layer zone.

When considering the vertical density gradient of figure 2.26b the relation between the mixing layer movements and the shock displacement is more evident than in figure 2.26a: close to the separation point, the shock foot and the mixing layer are highly correlated, as indicated when the reference point was near the shock foot (figure 2.24). In this zone, the Fourier modes decomposition showed high energy at low-frequencies. Considering reference points more downstream in the mixing layer, the shock movements become less and less correlated with the fluctuations at these points, while some circular structures begin to appear in the mixing layer. As for the horizontal density gradients, the circular structures can be related to the vortices generated by the Kelvin-Helmholtz instability, that are convected along the shear-layer in the downstream direction. Similar circular periodic patterns have also been observed in a shock-reflection configuration by Agostini et al. (2012) and associated to medium frequency unsteadiness trough band-pass filtering.

2.4 Conclusions

The aim of the experimental study presented in this chapter was to characterise a transonic shock wave/boundary layer interaction over the Délery bump, focusing on both the mean flow and the unsteadiness. Two-component PIV measurements gave access to a full flow description, providing details on the turbulent velocity field in the interaction region. The results presented for the mean flow give a complete description of the shock-induced separation region, providing new insight in the SWBLI case of a strong shock interacting with a turbulent boundary layer. The accuracy of the measurements was validated through a comparison with a similar study on the same configuration where possible, and all the results are in fair agreement with similar investigations. The boundary layer is shown to be completely developed and its size increases while approaching the shock due to the curvature of the bump. The main effect of the shock wave is the flow detachment with consequent formation of a separated region. The boundary layer recovery starts gradually downstream of the recirculating bubble. Three regions of the flow, supersonic, subsonic and reverse flow, have been completely characterised, and the mixing layer has also been analysed starting from the shock foot.

The analysis of wall-pressure and skin-friction fluctuations give access to a local description of the unsteady behaviour of the interaction. Near the shock foot, low-frequency unsteadiness dominates the spectrum, while after the separation point medium-frequency fluctuations are most energetic. The recirculation zone presents both low- and medium-frequency unsteadiness. Similarly to other SWBLI configurations the fluctuations are broadband and weak in amplitude, and no single-peak frequency dominates the spectrum as in the buffet problem. Using a characteristic length and velocity, the flow unsteadiness can be scaled to obtain two Strouhal numbers representative of low- and medium-frequency unsteadiness, that compare favourably with other configurations, confirming that the frequency-selection process typical of SWBLI is present for this particular transonic case.

Fourier modes decomposition of high-speed Schlieren visualisation can give some spatial information about the zone of the field where low- and medium-frequency unsteadiness are more energetic. The results confirm the separations of temporal scales between the unsteadiness in the shock region and in the mixing layer: the shock wave seems to behave as a low-pass filter, even if some medium-frequency motions can be found in the shock region, whilst the mixing layer region is characterised by medium-frequency motions. When considering correlation maps obtained investigating the vertical and horizontal density gradients, one can observe that shock motions are solid displacement accompanied by expansion and contraction movements of the recirculation bubble. When considering the mixing layer region, correlation maps

can highlight the vortex shedding caused by the separation point, linking Kelvin-Helmholtz type instability to the medium-frequency unsteadiness observed with wall measurements. Moreover, the size of the structure is small if compared to the size of the recirculation bubble, indicating that the medium-frequency unsteadiness is associated to the so called flapping motion of the shear layer.

Chapter 3

Numerical approach

The configuration experimentally analysed in chapter 2 is now numerically considered. The domain is a two-dimensional reproduction of the S8Ch wind tunnel, from the convergent section up to the second throat, not included in order to avoid the second shock wave, whose role is to filter the noise arising from the wind tunnel engines in the experimental investigation.

In a general case of turbulent flow for which the scale decoupling assumption holds, the dynamics of the large scales may be captured using unsteady RANS equations. Following this approach, the impact of the small scales dynamics onto the large ones is accounted for by a turbulence model, which results in additional viscosity, called the eddy viscosity.

In the case of SWBLI, all the experimental result described in the previous chapter have shown that the most energetic fluctuations can be divided in two distinct phenomena: the low-frequency oscillations in the shock region and the medium-frequency motions, localised mostly in the recirculation bubble and in the shear layer downstream the separation point. Both phenomena exhibit characteristic frequencies below those that can be observed in the small-scale motions representative of turbulence. For this reason, even if the turbulence undoubtedly affects the observed unsteady motions, we believe that the dynamics of a shock-wave/boundary-layer interaction can be described by the temporal integration of Reynolds-averaged Navier-Stokes equations. This assumption does not imply the independence of low- and medium-frequency unsteadiness to the turbulence, but indicates that most of the interaction dynamics can be captured without a complete simulation of all the small-scale structures present in the flow.

In this chapter we first perform a numerical simulation solving RANS equations (section 3.1). The flow field converges to a steady-state solution, indicating that unforced RANS equations are not able to capture the low- and medium-frequency unsteadiness. The asymptotic two-dimensional numerical solution is compared with

the mean flow obtained by PIV investigation in section 2.1. The solution is then considered for a stability analysis: the linearisation of the equations is presented in section 3.2, together with the eigenvalue decomposition of the Jacobian matrix. Different model governing small-amplitude perturbations are compared by analysing the flow spectrum and the associated global modes.

Finally, in section 3.3 we propose a stability analysis based on the global Resolvent, which aims at analysing the convective instabilities arising in a flow subject to external forcing: this forcing can be seen as environmental noise that is naturally present in the case of a real flow; the investigation will highlight any physical mechanism that is able to select and amplify particular perturbations at given frequencies. Such an approach should be able to analyse the role of the shock, the mixing layer or the recirculation bubble, in the frequency-selection process, and if there is a link between the unsteadiness observed in experiments and the quantities computed during the stability analysis.

3.1 Numerical simulation

Shock-wave/boundary-layer interactions require an accurate model to reproduce the various dynamical features shown in the experimental chapter. Turbulence models remain widely used in this area as the computational cost to solve the Navier-Stokes equations using direct numerical simulation (DNS) drastically increases with the Reynolds number. The Reynolds-Averaged Navier-Stokes equations (RANS) are obtained considering turbulent flows for which scale decoupling assumption holds. The whole numerical investigation presented in this section is based on this assumption, considering that the impact of the small scales dynamics onto the large ones is correctly captured by an eddy viscosity μ_t.

The simulations were performed using the elsA v3.3 code developed at ONERA and CERFACS (Cambier et al., 2012). This software solves, among others, RANS equations with various turbulence models and relies on a finite volume formulation applied on structured grids. Numerical computations were performed in parallel over up to 64 cores on ONERA's supercomputer Stelvio, using 2.8 GHz Intel Xeon 5560 (Nehalem) processors.

3.1.1 RANS equations

After spatial discretisation the governing equations can be recast in the general conservative form:

$$\frac{d\mathbf{w}}{dt} = \mathcal{R}(\mathbf{w}) \tag{3.1}$$

where $\mathbf{w} \in \mathbb{R}^{\mathbf{N}}$ represents the set of conservative variables describing the flow at each spatial location of the mesh in the domain Ω and $\mathcal{R} : \Omega \in \mathbb{R}^{\mathrm{N}} \rightarrow \mathbb{R}^{\mathrm{N}}$ is derivable over Ω and represents the discrete residuals. Using a finite volume method, the dimension of $\mathbf{w}$ corresponds to the number of cells in the mesh times the number of variables. Note that all boundary conditions are included in the discrete operator $\mathcal{R}$.

In a more complete form, the Navier-Stokes equations in equation (3.1) can be rewritten as:

$$\frac{d}{dt}\begin{pmatrix}\mathbf{w}^{\mathrm{mf}}\\ \mathbf{w}^{\mathrm{tf}}\end{pmatrix} = \begin{pmatrix}\mathcal{R}^{\mathrm{c,mf}} + \mathcal{R}^{\mathrm{d,mf}}\\ \mathcal{R}^{\mathrm{c,tf}} + \mathcal{R}^{\mathrm{d,tf}} + \mathcal{T}\end{pmatrix} \tag{3.2}$$

where the superscripts $^{\mathrm{mf}}$ and $^{\mathrm{tf}}$ refer respectively to the mean and turbulent fields of the RANS equations. In particular, $\mathbf{w}^{\mathrm{mf}} = (\rho, \rho\mathbf{U}, \rho\mathbf{E})^{\mathbf{T}}$ where ρ designates the density, $\mathbf{U}$ the velocity and E the total energy of the flow. Terms $\mathcal{R}^{\mathrm{c}}$, $\mathcal{R}^{\mathrm{d}}$ and $\mathcal{T}$ correspond respectively to the convective and diffusive fluxes of the equations and the turbulence source term. The continuous form of the mean field fluxes in equation (3.2) are given by:

$$\mathcal{R}^{\mathrm{c,mf}} = -\begin{pmatrix}\rho\mathbf{U}\\ \rho\mathbf{U}\otimes\mathbf{U} + \mathbf{pI}\\ \rho E\mathbf{U} + \mathbf{pU}\end{pmatrix} \qquad \mathcal{R}^{\mathrm{d,mf}} = \begin{pmatrix}0\\ \boldsymbol{\tau} + \boldsymbol{\tau_r}\\ \boldsymbol{\tau}\mathbf{U} + \boldsymbol{\tau_r}\mathbf{U} - \mathbf{q} - \mathbf{q_t}\end{pmatrix} \tag{3.3}$$

with

$$p = \rho RT \quad \boldsymbol{\tau} = -\frac{2}{3}\mu\left(\nabla\cdot\mathbf{U}\right)\mathbf{I} + \mathbf{2}\mu\mathbf{D} \quad \mathbf{q} = -\frac{\mathbf{c_p}\mu}{\mathbf{Pr}}\nabla\mathbf{T} \tag{3.4}$$

$$\boldsymbol{\tau_r} = -\frac{2}{3}\mu_t\left(\nabla\cdot\mathbf{U}\right)\mathbf{I} + \mathbf{2}\mu_\mathbf{t}\mathbf{D} \quad \mathbf{q_t} = -\frac{\mathbf{c_p}\mu_\mathbf{t}}{\mathbf{Pr_t}}\nabla\mathbf{T} \tag{3.5}$$

p is the pressure, R the perfect gas constant, c_p the heat capacity at constant pressure, μ the viscosity, T the temperature, $\boldsymbol{\tau}$ the viscous tensor, $\mathbf{q}$ the heat flux, $\mathbf{D}$ and $\mathbf{I}$ the rate of strain and identity tensors respectively, μ_t the eddy viscosity (computed with the chosen turbulence model), $\boldsymbol{\tau_r}$ the Reynolds stress tensor, $\mathbf{q_t}$ the flux of diffusion of turbulent enthalpy, Pr and Pr_t the classical and turbulent Prandtl number assumed constants and taken respectively equal to 0.72 and 0.9. The preceding equations were derived using Boussinesq hypothesis and perfect gas relations. The viscosity is computed using Sutherland's law:

$$\mu = \mu_s\sqrt{\frac{T}{T_s}}\frac{1 + C_s/T_s}{1 + C_s/T} \tag{3.6}$$

with the constants $\mu_s = 1.71\ 10^{-5}$ Pa·s, $C_s = 110.4$ and $T_s = 273$ K. The variables $\mathbf{U}, \mathbf{E}$ are Favre averages whereas the other ones corresponds to the classical Reynolds average.

Turbulence model

Spalart-Allmaras (S-A) turbulence model (Spalart and Allmaras, 1992) has been used to provide closure for the averaged Reynolds stresses, introducing the kinematic viscosity transform $\tilde{\nu}$ with $\mathbf{w}^{\text{tf}} = (\rho\tilde{\nu})$. The model has been chosen because previous studies (Brunet, 2003; Deck, 2005; Crouch et al., 2007) proved its ability to correctly reproduce the challenging buffet configuration, indicating that this particular one-equation model compares favourably even with more complex non-linear low-Re eddy-viscosity models (Barakos and Drikakis, 2000). The turbulent fluxes and source terms are then given by:

$$\mathcal{R}^{\mathbf{c,tf}} = -\left(\rho\tilde{\nu}\mathbf{U}\right) \qquad \mathcal{R}^{\mathbf{d,tf}} = \left(\frac{\mu + \rho\tilde{\nu}}{\sigma_{\tilde{\nu}}}\nabla\tilde{\nu}\right) \tag{3.7}$$

$$\mathcal{T} = \left(Prod + Cross + Dest\right) \tag{3.8}$$

The source terms can be identified as:

- a production term $Prod = C_{b1}\tilde{S}\rho\tilde{\nu}$
- a cross diffusion term $Diff = \dfrac{C_{b2}}{\sigma}\nabla\rho\tilde{\nu}\cdot\nabla\tilde{\nu}$
- a destruction term $Dest = -C_{w1}f_w\rho\dfrac{\tilde{\nu}^2}{\eta^2}$

with, noting Ω the vorticity:

$$\tilde{S} = |\Omega| + \frac{\tilde{\nu}}{K^2\eta^2}f_{v2}, \qquad f_{v2} = 1 - \frac{\chi}{1+\chi f_{v1}} \qquad f_w = g\left(\frac{1+C_{w3}^6}{g^6+C_{w3}^6}\right)^{1/6}$$

$$g = r + C_{w2}\left(r^6 - r\right) \qquad r = \frac{\tilde{\nu}}{\tilde{S}K^2\eta^2}$$

The turbulent eddy viscosity is finally defined by $\mu_t = \rho\tilde{\nu}f_{v1}$ with:

$$f_{v1} = \frac{\chi^3}{\chi^3 + C_{v1}^3} \qquad \chi = \frac{\rho\tilde{\nu}}{\mu}$$

The values of the constants for the Spalart-Allmaras model are given in Table 3.1. The model is designed such that the turbulent variable $\rho\tilde{\nu}$ tends towards the eddy viscosity μ_t far from the walls.

C_{b1}	C_{b2}	σ	K	C_{w1}	C_{w2}	C_{w3}	C_{v1}
0.1355	0.622	2/3	0.41	$C_{b1}/K^2 + (1 + C_{b2})/\sigma$	0.3	2	7.1

Table 3.1: Constants used in the Spalart-Allmaras model.

Numerical scheme

We use the finite volume code elsA developed at ONERA (Cambier et al., 2012) to solve the steady RANS and unsteady URANS equations. The system defined in equation (3.2) is solved for each cell (i, j) of volume Ω and surface Σ in its integral formulation:

$$\frac{d}{dt}\mathbf{W_{ij}} = \mathcal{R}^{\mathbf{c}}_{\mathbf{ij}} - \mathcal{R}^{\mathbf{d}}_{\mathbf{ij}} + \mathcal{T}_{\mathbf{ij}} = \mathcal{R}_{\mathbf{ij}}, \tag{3.9}$$

with:

$$\mathbf{W_{ij}} = \frac{1}{\mathbf{\Omega}} \int_{\mathbf{\Omega}} \mathbf{W} \mathrm{d}\mathbf{\Omega} \qquad \mathcal{T}_{\mathbf{ij}} = \frac{1}{\Omega} \int_{\Omega} \mathcal{T} \mathrm{d}\Omega \tag{3.10}$$

$$\mathcal{R}^{\mathbf{c,d}}_{\mathbf{ij}} = \frac{1}{\Sigma} \oint_{\Sigma} \mathcal{R}^{\mathbf{c,d}} \cdot \mathbf{n} \mathrm{d}\Sigma = \frac{1}{\Omega} \left(\mathcal{R}^{\mathbf{c,d}}_{\mathbf{i+1/2,j}} + \mathcal{R}^{\mathbf{c,d}}_{\mathbf{i,j+1/2}} + \mathcal{R}^{\mathbf{c,d}}_{\mathbf{i\text{-}1/2,j}} + \mathcal{R}^{\mathbf{c,d}}_{\mathbf{i,j\text{-}1/2}} \right) \tag{3.11}$$

In particular $\mathcal{R}_{\mathbf{ij}}$ corresponds to the discrete residual operator.

A second-order AUSM+(P) upwind scheme is used for the mean convective fluxes (Mary et al., 2000). Roe and Jameson schemes were not considered due to poor shock treatment when investigating low-frequency dynamics. All numerical limiters where forced to be inactive. The convective flux associated to the turbulence equation $\mathcal{R}^{\mathbf{c,tf}}_{\mathbf{ij}}$ is discretised using the first-order Roe scheme with Harten's correction to prevent the occurrence of low eigenvalues (Harten and Hyman, 1983), whilst a central difference scheme is used for the turbulent diffusive flux. The viscous flux of the mean field is calculated at the interface by averaging cell-centred values of flux density which is computed from cell-centred evaluation of gradients. The source terms are discretised using estimates of gradients and variables at cell centres.

Steady-state solutions are obtained using a backward-Euler scheme with local time-stepping. Unsteady solutions are computed using second-order Gear's formulation with a physical time step fixed at $T_{st} = 5 \cdot 10^{-7}$, which corresponds, for the grid described in section 3.1.2 to maximum CFL numbers of about 15 in the boundary layer, and in most of the domain below 1. At least 8 Newton sub-iterations are required at each time step to decrease the norm of the residual by a factor of 10.

Boundary conditions

The boundary conditions are imposed directly in the fluxes evaluation at the boundary, and correspond to the experimental configuration as described in chapter 2: both

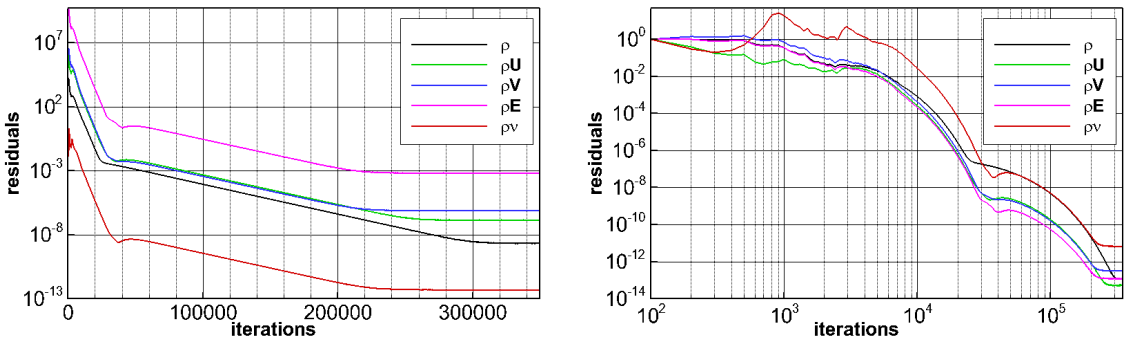

(a) Residuals computation.

(b) Normalised residual.

Figure 3.1: Evolution of the explicit residuals during a base flow computation initialising the flow with a uniform state.

upper and lower walls are considered as adiabatic and the boundary layers start developing in the settling chamber. As in the experimental investigation, a boundary layer develops at the upper wall and interacts with the shock wave producing an incipient separation bubble.

The inlet boundary condition matches the thermodynamical state of the flow in the settling chamber of the experiment: the total temperature is 300 K and the total pressure is 96500 Pa. The flow enters in the contraction at Mach number 0.1, given by a horizontal velocity of 35 m/s and no vertical velocity component. The boundary condition at the end of the domain is an outlet pressure condition, where the uniform pressure value has been imposed to match the shock-wave position on the bump (approximately p = 62 kPa at x = 0.65 m).

Convergence of the computation is assessed by ensuring that the explicit residuals of the mean and turbulent equations have decreased from their value at the first iteration (the computation is initialised with a uniform flow) by at least 8 orders of magnitude. A typical evolution of the residuals is given in figure 3.1 for the mesh described in section 3.1.2.

3.1.2 Computational grid

The computational domain is a single-block reproduction of the S8Ch wind tunnel. All the numerical simulations and the stability analyses are performed on the same structured grid, composed of 120000 nodes: 300 nodes in the vertical direction and 400 nodes in the stream-wise direction, 200 of whom in the vicinity of the shock, where the average distance between two mesh points is 0.45 mm. Considering the bump length c as a characteristic dimension, this corresponds to a resolution of $\Delta_x/c = 0.0016$ in the interaction region. In this zone, outside of the boundary layer,

the cells are almost square, the grid spacing in the boundary layer is refined in order to locate the first point always below $y^+ = 0.6$.

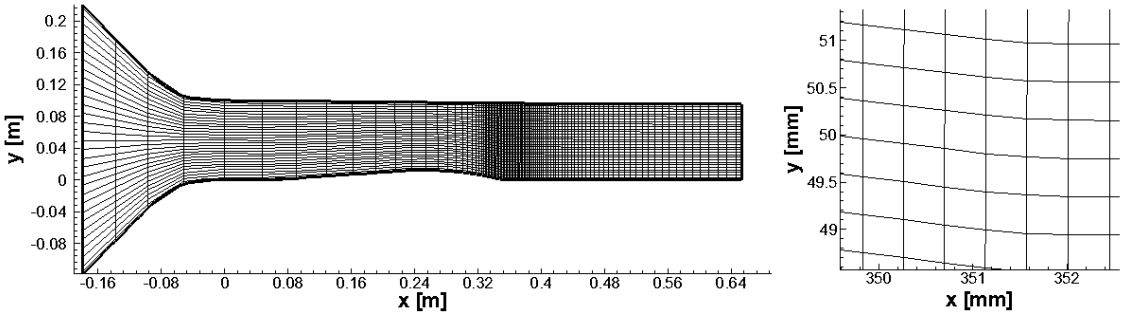

Figure 3.2: Left: whole domain, showing 1 point out of 4 in x and 1 out of 8 in y. Right: zoom in the shock region, showing all the points of the grid.

Figure 3.2 shows the whole domain used in the numerical investigation: on the left, one can see that all the channel is represented, from the convergent section to the test section. The shock region is refined using a constant point distribution in the horizontal direction (only one point out of 4 is represented in x and 1 point out of 8 in the vertical direction). The right part of figure 3.2 presents a zoom in the vicinity of the shock, where the cells are almost square, to obtain the same resolution for both the horizontal and vertical directions. To check the spatial convergence of the computations, four other meshes are considered, where we modified the number of points in the interaction region. Considering the mesh with 120000 points as the reference, two coarser and two finer grids are analysed. The characteristics of the different grids with the spacing between their nodes are summarised in table 3.2.

mesh name	I_{max}	J_{max}	Δ_x	Δ_x/c
mesh 1	340	300	0.69 mm	$2.4 \cdot 10^{-3}$
mesh 2	370	300	0.57 mm	$2.0 \cdot 10^{-3}$
reference	400	300	0.45 mm	$1.6 \cdot 10^{-3}$
mesh 3	450	300	0.34 mm	$1.2 \cdot 10^{-3}$
mesh 4	540	300	0.23 mm	$0.8 \cdot 10^{-3}$

Table 3.2: Characteristics of the computational grids.

All grids converge to the same RANS solution in terms of shock location, size of the recirculation bubble and separation point position. The effect of the grid refinement impacts the shock thickness: figure 3.3 presents the density jump across the shock obtained using the different grids. The points on the lines indicate nodes in the meshes. Stream-wise density profiles have been extracted at the point where the shock wave is normal to the flow direction, around $y = 0.08$ m. One can notice

that the shock is always described by the same number of points, and the shock location, marked in figure 3.3a by a vertical line, is independent of the grid spacing.

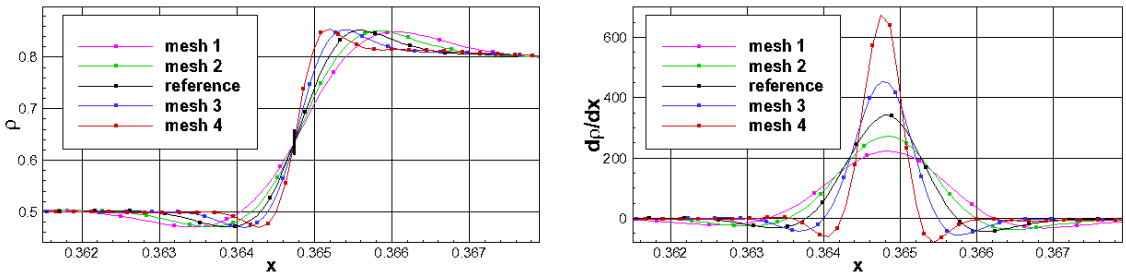

(a) Density across the shock wave.

(b) Density-gradient across the shock wave.

Figure 3.3: Density and density-gradient evolution across the shock wave.

However, the mesh refinement has a strong impact on the shock thickness: figure 3.3b presents the evolution of $\partial\rho/\partial x$ and indicates that coarser grids correspond to thicker shocks. As will be shown in the next sections, this will not impact the results of global-mode decomposition. On the contrary, the results of the stability analysis based on the global Resolvent will show a higher dependency on the grid spacing, as they consider the energy associated to the shock wave, that depends on its thickness. Despite this particular case that will be discussed in section 3.3, the computations show a good grid convergence, and if not specified, the results will refer to the reference mesh.

3.1.3 Results

The velocity field stemming from the RANS simulation is presented in figure 3.4. Superimposed to the isocontour plot of the stream-wise velocity field, the dashed-dotted line indicates the zone of the flow where the Mach number is equal to 1. The lambda-shock system can also be seen by observing the distribution of the horizontal and vertical density gradient, as shown in figures 2.20 and 2.21. On the upper wall the strong pressure gradient of the shock wave induces separation of the turbulent boundary layer, and a small separation bubble is visible. This feature cannot be confirmed by the experimental investigation since PIV results do not cover the whole channel.

Figure 3.5a presents a comparison between the horizontal velocity component obtained with the PIV investigation, as described in section 2.1, and the result of the RANS simulation. The shock position, even if not completely captured by the PIV frame, is correctly reproduced on the top of the test section, but in the numerical result the shock foot seems to be slightly more downstream. Moreover,

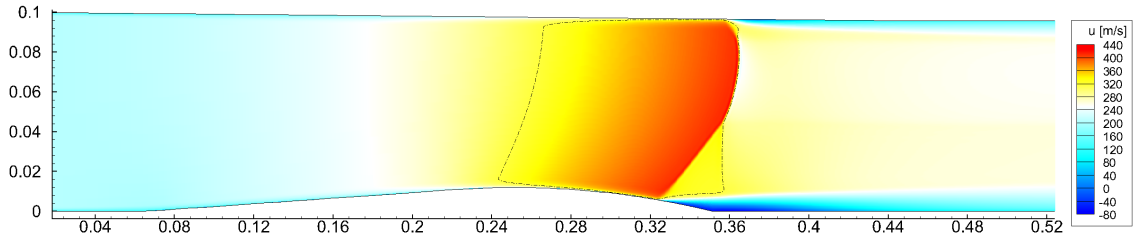

Figure 3.4: Stream-wise velocity field. Sonic line dash-dotted.

the PIV results indicates a thicker shock, but this can be caused by the integration of shock unsteadiness in the experiments. The supersonic tongue is underestimated by the RANS simulation, while the extent of the separation bubble is overestimated. Figure 3.5b presents the turbulent eddy-viscosity obtained with the Spalart-Allmaras turbulence model.

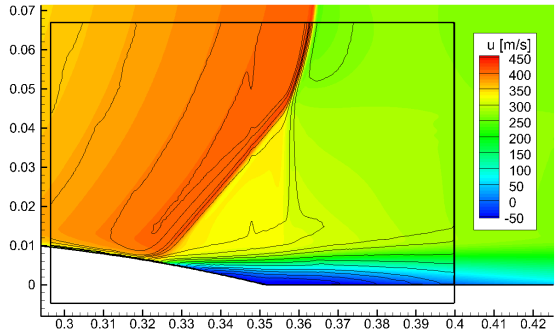

(a) Horizontal velocity field: RANS simulation versus PIV measurements (solid lines).

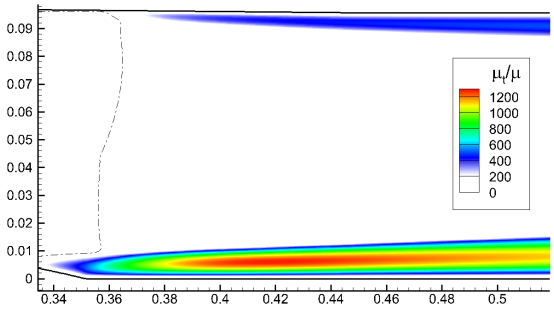

(b) Turbulent viscosity ratio.

Figure 3.5: RANS simulation results and comparison with PIV investigation.

Some other comparisons between the numerical and experimental results are presented in figure 3.6. Static pressure has been measured through 36 pressure taps in the centreline at the lower wall: numerical result, obtained representing static pressure at the first grid cell, are in a good agreement with the wind tunnel data: the flow acceleration on the convergent is correctly reproduced and one can observe a rise of static pressure starting from $x = 320$ mm, corresponding to the shock foot. The recirculation bubble is characterised by a small pressure plateau, and after the separated zone the static pressure reaches the value imposed at the downstream boundary condition.

Figure 3.6b presents two velocity profiles taken inside the recirculation bubble (at $x = 360$ mm) after the end of the bump. Starting from the wall, one can notice that the PIV investigation and RANS simulations are in agreement in the separated zone, with the PIV measurements indicating a smaller negative velocity inside the

bubble. This can be considered, as discussed in section 2.1, as a limitation of the experimental investigation, that tends to underestimate the velocity magnitude close to the walls. From $y = 10$ mm to $y = 50$ mm, the profile is between the first shock leg and the second shock. Here the velocity values obtained with RANS simulation are 5% smaller than those obtained in the experimental investigation. This discrepancy can be attributed to the different shock shapes obtained in the numerical and PIV studies. However, starting from $y = 60$ mm, the profile is in the supersonic zone before the shock wave (see figure 3.5), where experimental and numerical results indicate the same velocity.

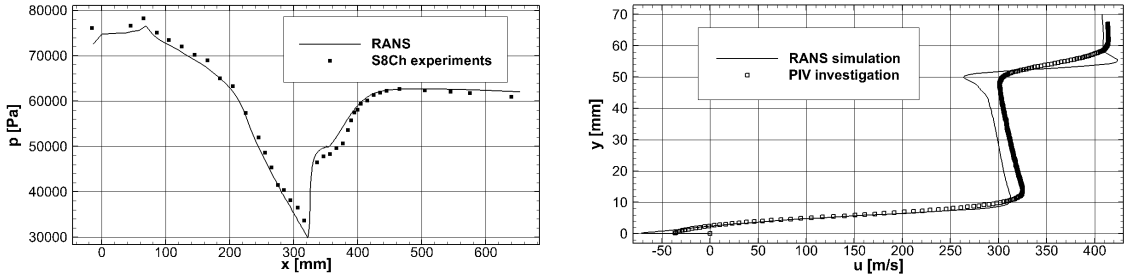

(a) Wall pressure.

(b) Velocity profiles.

Figure 3.6: Comparison between experimental and numerical investigation.

Overall, RANS computations are in a fair agreement with the experimental investigation, even if some discrepancy exists in the separation zone, probably caused by the tendency of PIV investigation to underestimate the size of the recirculation bubble, as discussed in section 2.1. However, the goal of the RANS simulation is not to reproduce the mean flow, but to obtain a base flow, sufficiently close to the experimental configuration analysed in chapter 2, in order to investigate the unsteadiness of this transonic SWBLI. In that respect, the characteristic length and velocity used in future sections to scale the frequency are the same as in the experimental investigation: $L = 35$ mm is taken as the interaction length, corresponding to the distance between the separation point and the projection of the second shock on the wall, and $U = 300$ m/s is considered again as the characteristic velocity, corresponding to the speed of the flow above the recirculation bubble, even if the numerical results indicate a slightly different value.

URANS computations indicate that the flow is steady. This result is not surprising since Knight and Degrez (1998) analysed the numerical prediction capabilities of RANS computations and stated that turbulent interaction predictions are only correct in terms of mean-pressure distribution: in this case, the RANS calculations fail to predict the intermittent separation stage and to capture the high levels of unsteadiness in the shock system.

Configuration without boundary layers

For reasons that will be clear in the next sections, we also considered a configuration with the same geometry, but with a slip boundary condition on both upper and lower walls, in order to remove the boundary layers and the separated regions from the base flow. The computational grid is the same as the one described in section 3.1.2, but without the grid refinement close to the walls. A new RANS simulation yields a transonic channel flow with a normal shock wave impinging on the bump. The outlet pressure was adapted in order to locate the shock at approximately the same position as the configuration with boundary layers.

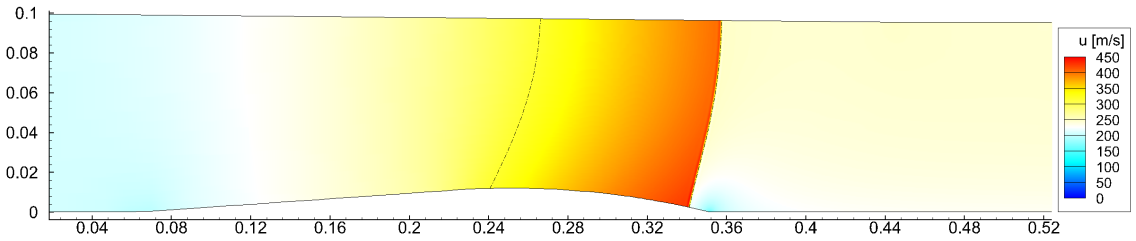

Figure 3.7: Configuration without boundary layers. Sonic line dash-dotted.

As can be seen from figure 3.7, the shock foot is at the end of the bump, approximately in the same position as in the configuration with boundary layers (figure 3.4). The absence of viscous effects yields a single curved shock without the characteristic lambda pattern observed in the previous case: the shock is now a normal strong shock always perpendicular to velocity vector. This configuration gives access to the effects of the shock wave independently from the separation bubble, and as will be seen in next sections, can give some useful insight on the acoustic resonances and on the shock response to external forcing.

3.2 Global-mode decomposition

In this section we describe the linearisation process that yields the Jacobian matrix, and then we perform a stability analysis based on the eigenvalue decomposition of the linear operator.

3.2.1 Theoretical formulation

In the following, the flow dynamics is governed by equation (3.1). RANS computations described in section 3.1 indicate that there exists a steady solution $\mathbf{w_0} \in \mathbb{R}^{\mathbf{N}}$, referred to as the base flow, defined by the discrete equation:

$$\mathcal{R}\left(\mathbf{w_0}\right) = \mathbf{0}. \tag{3.12}$$

In the examined case, the governing system contains the Spalart-Allmaras equations, thus the base flow $\mathbf{w_0}$ takes into account the Reynolds stresses involved in the turbulent model. The vector $\mathbf{w_0}$ thus represents

$$\mathbf{w_0} = (\rho_\mathbf{0}, \rho\mathbf{U_0}, \rho\mathbf{V_0}, \rho\mathbf{E_0}, \rho\nu_\mathbf{0})^\mathbf{T} \tag{3.13}$$

where $\rho\nu$ is introduced by the Spalart-Allmaras turbulence model and the subscript $_0$ indicates that the variables are referred to the steady solution found by RANS simulations.

The stability of the base flow is probed by analysing the evolution of a small amplitude perturbation $\epsilon\mathbf{w}'$ superimposed on the base flow: $\mathbf{w} = \mathbf{w_0} + \epsilon\mathbf{w}'$, with $\epsilon \ll 1$. In the case of governing equations involving a turbulence model, the perturbation also involves variations of the turbulent quantities, and the turbulence model equation is also linearised in the stability study. However, we will show in section 3.2.3 that some interesting results can be obtained considering other linearisation methods, where the fluctuation of the turbulent quantities are not taken into account when deriving the Jacobian matrix (frozen μ_t model), or where the turbulent variable is not considered at all (quasi-laminar model).

The equation governing the perturbation is given by the linearisation to the first order of the discretised equations (3.2):

$$\frac{d\mathbf{w}'}{dt} = \mathbf{J}\mathbf{w}' \tag{3.14}$$

The Jacobian operator $\mathbf{J} \in \mathbb{R}^{\mathrm{N}\times\mathrm{N}}$ corresponds to the linearisation of the discrete Navier-Stokes operator $\mathcal{R}$ around the base flow $\mathbf{w_0}$:

$$\mathbf{J_{ij}} = \left.\frac{\partial\mathcal{R}_\mathbf{i}}{\partial\mathbf{w_j}}\right|_{\mathbf{w}=\mathbf{w_0}} \tag{3.15}$$

where $\mathcal{R}_\mathrm{i}$ designates the i^{th} component of the residual, which is a priori a function of all unknowns $\mathbf{w_j}$ in the mesh. The $\mathbf{J}$ operator involves spatial stream-wise and cross-stream derivatives, which may be discretised with finite volumes to lead to a large-scale matrix. Since we use a finite volume method, the spatial discretisation stencil is compact and the i^{th} component of the residual only depends on few neighbouring unknowns. Hence, $\mathbf{J}$ is a sparse matrix in such cases. The proposed formalism does not assume homogeneity of the fluctuations in a given direction, and corresponds to the BiGlobal linear-stability analysis as introduced by Theofilis (2003).

A base flow or a matrix $\mathbf{J}$ is said to be asymptotically stable if the modulus of any initial perturbation tends to zero for large times; otherwise it is asymptotically unstable. Based on this definition, the stability of a base flow is determined by scrutinising the spectrum of the matrix $\mathbf{J}$. To this end, particular solutions of

equation (3.14) are sought in the form of normal modes $\mathbf{w}' = \hat{\mathbf{w}}\mathbf{e}^{\lambda \mathbf{t}}$, where $\lambda = \sigma + i\omega$ describes its temporal behaviour (σ is the amplification rate and ω the pulsation) and $\hat{\mathbf{w}} \in \mathbb{C}^N$ its spatial structure. Then equation (3.14) may be recast into the following eigenvalue problem:

$$\mathbf{J}\hat{\mathbf{w}} = \lambda\hat{\mathbf{w}} \tag{3.16}$$

If at least one of the eigenvalues λ exhibits a positive growth rate σ, then the base flow $\mathbf{w_0}$ is unstable. We refer to unstable flows as oscillators since the unstable mode will naturally grow and impose its dynamics to the flow regardless of any external perturbations. Noise amplifiers refer to globally stable flows, in which case an external forcing term is required to maintain unsteadiness.

3.2.2 Numerical strategy

To compute the linearised operator, we follow a strategy based on a finite difference method to obtain $\mathbf{Ju}$, where $\mathbf{u}$ is an arbitrary vector. More precisely, we evaluate the Jacobian matrix by repeated evaluations of the residual function. The code used to perform CFD simulation may then be used in a black box manner: assuming that the code generates a valid discrete residual $\mathcal{R}(\mathbf{u})$, one may obtain $\mathbf{Ju}$ with the following first order approximation:

$$\mathbf{Ju} = \frac{\mathbf{1}}{\epsilon}\left[\mathcal{R}\left(\mathbf{w_0} + \epsilon\mathbf{u}\right) - \mathcal{R}\left(\mathbf{w_0}\right)\right] \tag{3.17}$$

where ϵ is a small constant. By choosing a series of well-defined vectors $\mathbf{u}$, we can compute all the Jacobian coefficients involved in (3.15) solely by residual evaluations, which are provided by the numerical code. Moreover, the Jacobian structure is intrinsically linked to the discretisation stencil, which we chose to be compact, ensuring the sparsity of the matrix. The procedure is then optimised using a set of vectors $\mathbf{u}$ that take into account the stencil discretisation of the residual $\mathcal{R}$ in order to compute all the matrix $\mathbf{J}$ coefficients with only a few residual evaluations. More details on the numerical strategy can be found in Mettot et al. (2013).

Once we obtain the linearised Navier-Stokes operator, the eigenvalue problems in equation (3.16) are solved using Krylov methods combined with a shift-invert strategy (open source library ARPACK (Lehoucq et al., 1998)), so as to focus on the least-damped eigenvalues. Matrix inversions are carried out in the following with a direct sparse LU solver for distributed memory machines (MUMPS see http://graal.ens-lyon.fr/MUMPS/, or SuperLU-dist see http://acts.nersc.gov/superlu/). The inverses are quickly obtained but the drawback is the very high requirements in terms of memory, typically around 50 times the memory of the matrix to be inverted.

3.2.3 Results

The theoretical approach hereby described has been applied to the RANS solution presented in section 3.1. In order to ease the comparison between numerical and experimental investigation, we will present the results using the dimensionalised frequency f (expressed in Hertz, instead of the pulsation ω). The Strouhal number S_L, as introduced in equation (1.1), is also shown in the plots. By solving the eigenvalue problem in equation (3.16) we obtain a set of global modes, depicted in figures 3.9 and 3.11. The spectrum is obtained by computing the five closest eigenvalues with respect to a given shift. Several computations with a shift ranging from $f = 0$ up to $f = 7000$ Hz (corresponding to $S_L = 0.8$).

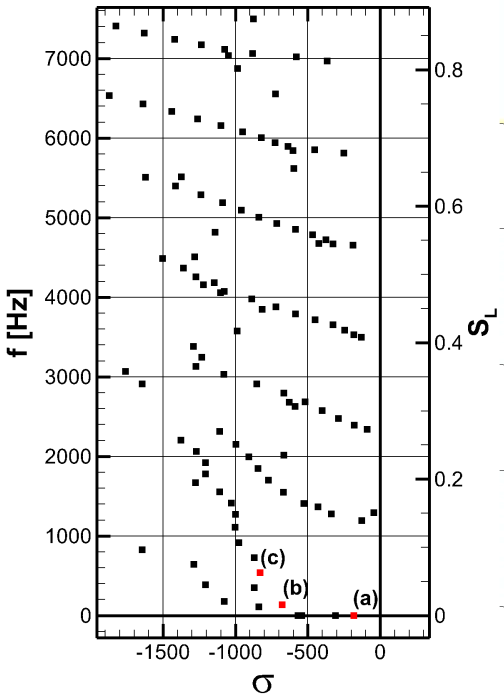

Figure 3.8: Eigenvalues.

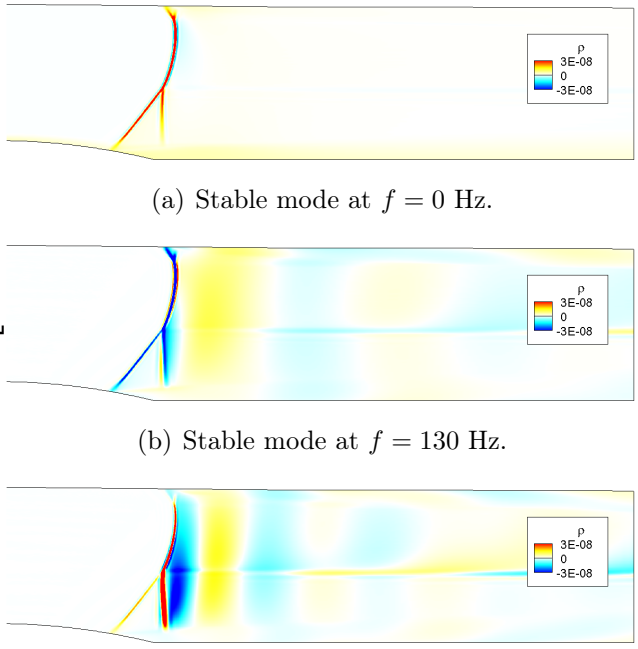

(a) Stable mode at $f = 0$ Hz.

(b) Stable mode at $f = 130$ Hz.

(c) Stable mode at $f = 540$ Hz.

Figure 3.9: Stable global modes.

As indicated in figure 3.8, all the eigenvalues display a negative real part, indicating that the global modes are damped. Among the stable eigenvalues (see red symbols) one can recognise a group of modes in the lower part of the spectrum, in the range of Strouhal number that corresponds to low-frequency unsteadiness. Figure 3.9 shows the real part of some of those modes (only the density component is depicted), that is located entirely on the shock wave. The first mode (figure 3.9a) is stationary, and does not carry any information about the unsteady behaviour of the interaction. The two other (figures 3.9b and 3.9c) are also located mainly on the shock as in the previous case, but with the addition of the slip line caused by the triple point and some sort of vertical structures after the shock. A possible interpre-

tation could be that those structures are acoustic waves that resonate with the test section, and the shock responds with a solid-body motion to those waves. However, despite the fact that the mode frequency is in the range of low-frequency motions, all the modes are stable, so the link between the low-frequency shock unsteadiness and those modes remains a hypothesis.

Considering higher Strouhal numbers, one can recognise that the eigenvalues in figures 3.8 and 3.10 (the eigenvalues are represented) are grouped in periodic quasi-horizontal lines, with some scattering as the damping rate becomes very strong. The spatial form corresponding to the first mode on each quasi-horizontal line (see red symbols) is presented in figure 3.11: the shock wave is still visible, but the circular structures present in each case suggest that the modes are probably linked to acoustic phenomenon.

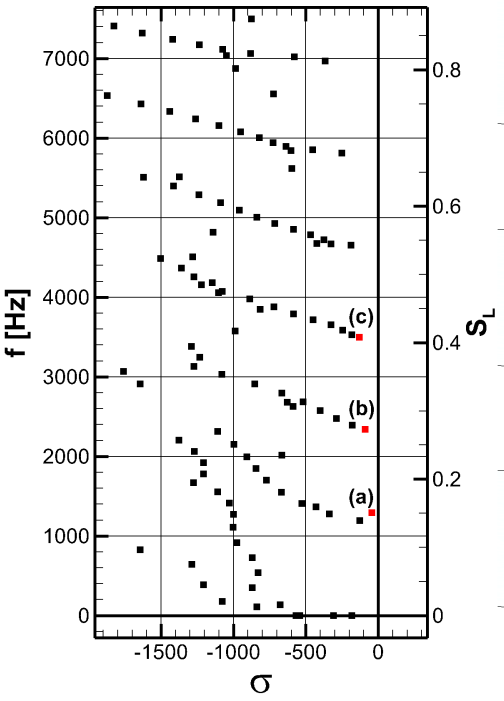

Figure 3.10: Eigenvalues.

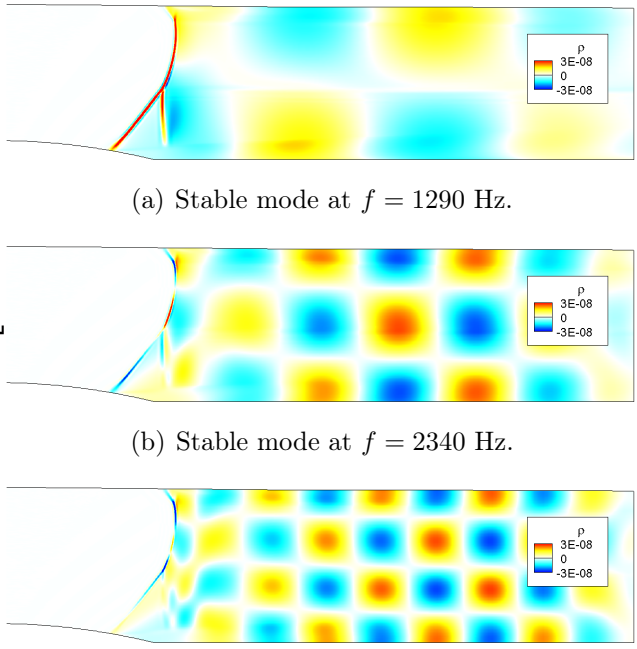

(a) Stable mode at $f = 1290$ Hz.

(b) Stable mode at $f = 2340$ Hz.

(c) Stable mode at $f = 3500$ Hz.

Figure 3.11: Stable global modes.

In this configuration, as for a generic flow in long ducts, if the acoustic wavelength has the same size of the characteristic device length, the acoustic standing-wave resonances may dominate the flow (Koch, 2005). As it will be shown in section 3.3, those resonances are independent from the interaction between the shock and the boundary layer, and scale with the channel height. Considering more damped eigenvalues, more than 100 eigenvalues have been analysed. Even if many modes can be found in the Strouhal number range that correspond to medium-frequency unsteadiness, none of them present a spatial structure that can be linked to mixing

layer instabilities as expected from the experimental investigation.

Grid convergence

As previously introduced, two finer and two coarser meshes have been considered to assess the grid dependency. In the numerical simulation of section 3.1.2, changing the spatial resolution in the interaction zone was directly affecting the shock thickness. Figure 3.12a shows the superposition of the spectra obtained with all the different grids, as described in section 3.1.2.

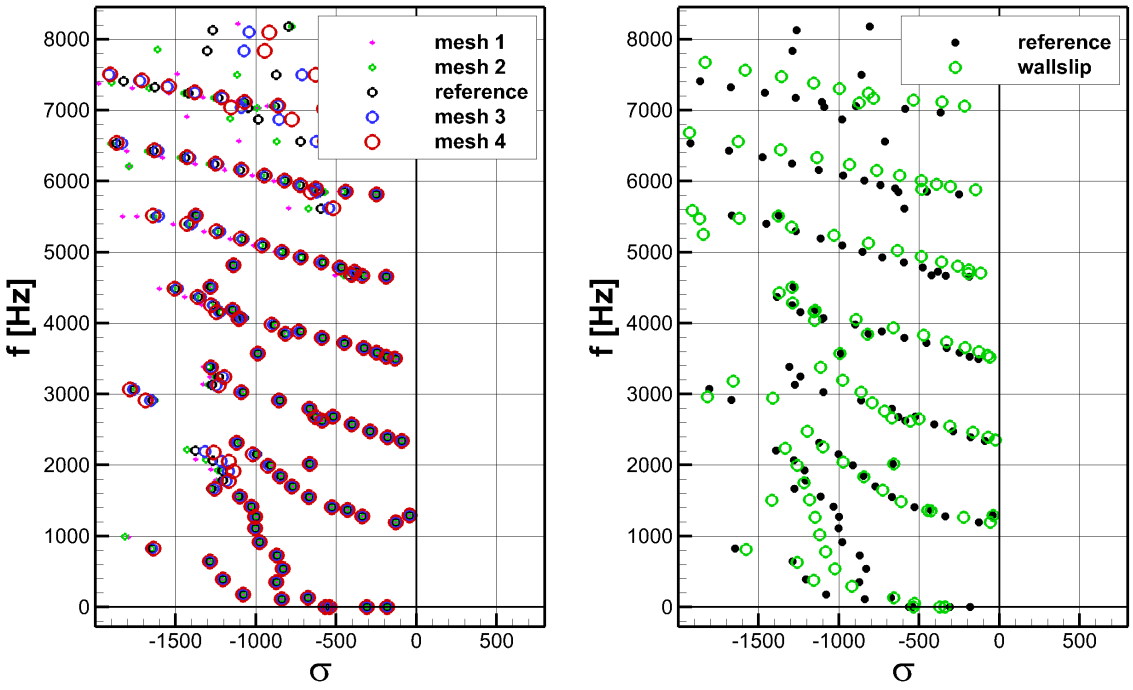

(a) Grid convergence.

(b) Configuration without boundary layers.

Figure 3.12: Eigenvalue decomposition for different grids and configurations.

On can notice a very small grid dependency of the eigenvalues. The modes can be considered converged in the lower part of the spectrum, while some discrepancies appear at higher frequencies, which is consistent with the fact that these modes are associated to small-scale structures. Coarser meshes can cause spatial filtering of those structures. However, the frequency associated to those structures are outside the range of interest of our study (the medium frequency unsteadiness occurs in the experiments around $f = 2 - 6$ kHz), so we consider that the *reference* grid is adapted for the purpose of the investigation.

Boundary-layer effects

Figure 3.12b presents the comparison between the eigenvalues of the reference case and the eigenvalues obtained when considering the base flow obtained with a slip condition on the walls, described in section 3.1. The absence of boundary layers barely impacts the eigenvalue distribution: one can still recognise that the modes are grouped in quasi-horizontal lines, confirming that these modes are neither linked to the boundary layer nor the shear-layer dynamics, but more to the acoustical features of the channel. Low-frequency eigenvalues are slightly more damped, and no high-frequency modes appear or disappear from the spectrum in this configuration, suggesting once again that the eigenvalue decomposition does not yield a complete characterisation of the dynamics of the SWBLI.

Other models governing the perturbation dynamics

All the results presented up to this point were obtained considering a linear model obtained by linearisation of the full equations, including the turbulence model: the imposed perturbations included fluctuations of the eddy viscosity μ_t'. We will now consider two different cases, where we treat differently the turbulence variable in the linearisation process.

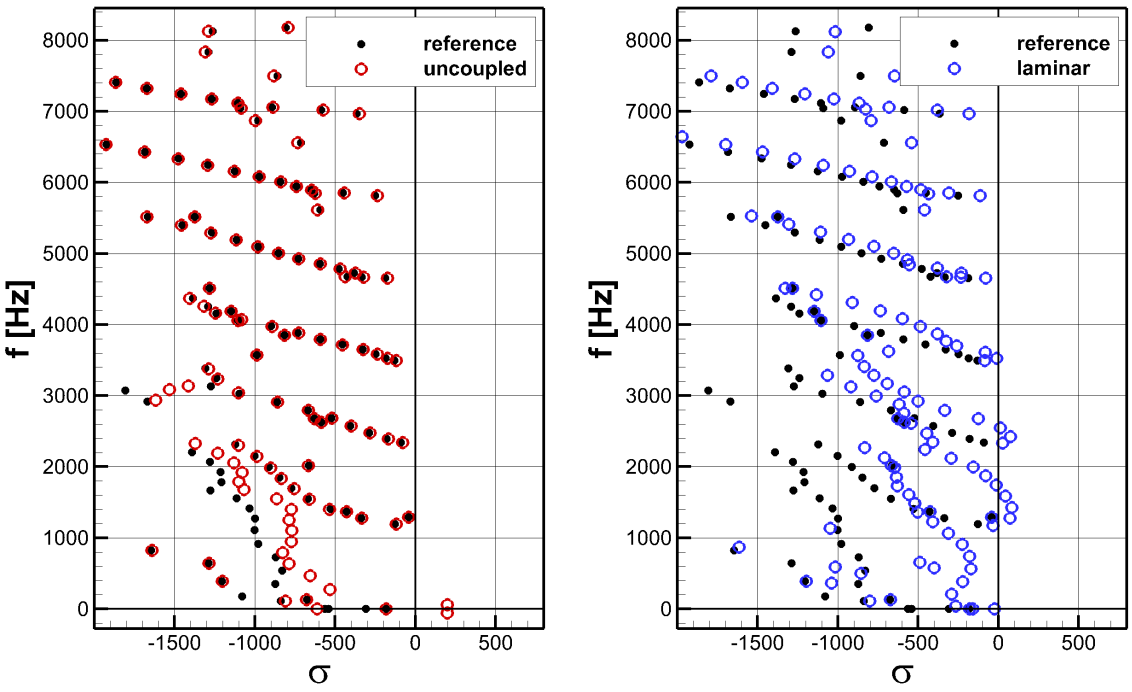

(a) Uncoupled spectrum.

(b) Quasi-laminar spectrum.

Figure 3.13: Eigenvalue decomposition for linearisation methods.

In particular, we will consider the so-called uncoupled and quasi-laminar system

as proposed by Reynolds and Hussain (1972). The first case is obtained when in the mean field equations (3.2) the turbulent variable is frozen in the linearisation process, so that the eddy viscosity is a spatial field that only depends on the coordinate system, without fluctuations μ_t' (Cossu et al., 2009; Juan and Javier, 2006). In the second case, turbulence is taken into account only for the determination of the base flow (RANS simulation), but during the linearisation process the eddy viscosity μ_t is neglected in (3.3). This is equivalent to assuming that, when analysing the evolution of the small amplitude perturbation, the turbulence affects the perturbations only indirectly, through the mean velocity profile, and not directly, through its stresses (Reynolds and Hussain, 1972). It's important to note that the base flow is always the same since $\mathbf{w_0}$ satisfies equation (3.12) as presented in section 3.1, but a different linearisation process leads to a different Jacobian matrix $\mathbf{J}$.

The eigenvalue decomposition of the Jacobian matrix for the uncoupled system is presented in figure 3.13a. In the same plot is also represented the spectrum obtained for the coupled system as discussed before, indicated as *reference*: an unstable global mode appears at $f = 57$ Hz. The mode, whose spatial distribution of density component is presented in figure 3.14a is similar to the stable mode obtained for $f = 0$ Hz but we also observe structures on the mixing layer and the slip line. The result suggests that the shock motions could be described by an unstable global mode. Yet, this is most likely not relevant to describe the broadband SWBLI unsteadiness, because it indicates that the flow spectrum should display a peak in the vicinity of the eigen-frequency, similarly to the shock buffeting problem considered in chapter 4.

(a) Unstable global mode at $f = 57$ Hz. Uncoupled Jacobian matrix.

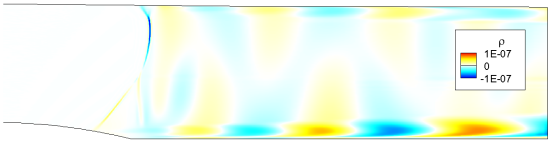

(b) Unstable global mode at $f = 1590$ Hz. Quasi-laminar Jacobian matrix.

Figure 3.14: Unstable global modes obtained with different linearisation methods.

A part from the unstable global mode, one can notice a very good agreement between the coupled and uncoupled system, for all medium frequency modes. When considering eigenvalues with frequencies less than 2000 Hz excluding acoustic modes, a small shift in the amplification rate is observed.

The eigenvalue decomposition of the quasi-laminar system, presented in figure 3.13b, yields similar results: most of the modes are grouped in lines as the acoustic modes in the reference case, whilst the others show a shift in σ. However, in this case

no low-frequency unstable modes are found, but concerning the medium-frequency range, a series of slightly unstable modes can be observed at frequencies where the reference case presented the least stable eigenvalues. The spatial distribution of the most unstable mode is presented in figure 3.14b: the density component shows periodic quasi-circular structures as for the acoustic resonance mode at a similar frequency in figure 3.11a, but with the addition of more energetic structures in the mixing layer zone.

Here again the result is interesting since it suggests that Kelvin-Helmholtz type instability could be described by the considered approach; yet such modes may not be relevant to discuss medium-frequency unsteadiness since in the experimental spectrum we observed broadband fluctuations, not linked to acoustic phenomena. As Reynolds and Hussain (1972), who considered the linear stability of the mean flow profile in a turbulent channel flow, we conclude that the eddy viscosity model is mandatory to take into account the impact of the small turbulent scales onto the perturbations dynamics.

3.3 The global Resolvent

Regardless of the fact that the Jacobian matrix $\mathbf{J}$ may or may not have unstable eigenvalues in equation (3.16), the flow may exhibit transient growth due to the non-normality of the linearised Navier-Stokes operator (Sipp et al., 2010). In the case of a noise-amplifier flow, all the eigenvalues of $\mathbf{J}$ are damped: an external forcing is required to sustain unsteadiness. In experiments, this external forcing may be the environmental noise naturally present in the wind tunnel, or some form of noise arising from the separated zone, which is not taken into account in the RANS and URANS simulation.

3.3.1 Theoretical formulation

Noise amplifiers dynamics can be analysed by considering the response of the base flow to a small amplitude forcing. For this reason we consider the RANS equations as in (3.1) where we add a small external forcing $\mathbf{f}'$:

$$\frac{d\mathbf{w}}{dt} = \mathcal{R}(\mathbf{w}) + \mathbf{f}' \tag{3.18}$$

The flow $\mathbf{w}$ can be seen as the superposition of the base flow $\mathbf{w_0}$ plus a response $\mathbf{w}'$, driven by the external forcing $\mathbf{f}'$:

$$\mathbf{w} = \mathbf{w_0} + \mathbf{w}' \tag{3.19}$$

If we introduce this decomposition in equation (3.18) and consider that the base flow $\mathbf{w_0}$ is a solution of the Navier-Stokes equations (thus $d_t\mathbf{w_0} = \mathbf{0}$) we have:

$$d_t\mathbf{w}' = \mathcal{R}(\mathbf{w_0} + \mathbf{w}') + \mathbf{f}' \tag{3.20}$$

Considering a first-order Taylor expansion of the Residual, which is valid for small amplitude forcing, the response $\mathbf{w}'$ is governed by the linearised Navier-Stokes equations, with $\mathbf{J}$ as the Jacobian matrix introduced in equation (3.14):

$$d_t\mathbf{w}' = \mathbf{J}\mathbf{w}' + \mathbf{f}' \tag{3.21}$$

We consider, at a given real frequency ω, a forcing $\mathbf{f}'(\mathbf{x},\mathbf{y},\mathbf{t})$ and a response $\mathbf{w}'(\mathbf{x},\mathbf{y},\mathbf{t})$ in the form $\mathbf{f}' = \hat{\mathbf{f}}(\mathbf{x},\mathbf{y})\mathbf{e^{i\omega t}}$ and $\mathbf{w}' = \hat{\mathbf{w}}(\mathbf{x},\mathbf{y})\mathbf{e^{i\omega t}}$: the harmonic forcing $\hat{\mathbf{f}}$ induces the harmonic response $\hat{\mathbf{u}}$, with $\hat{\mathbf{f}}, \hat{\mathbf{w}} \in \mathbb{C}^N$. Simplifying and re-arranging the equation for $\hat{\mathbf{w}}$ yields:

$$\hat{\mathbf{w}} = \mathscr{R}\hat{\mathbf{f}} \tag{3.22}$$

where $\mathscr{R}(\omega) \in \mathbb{C}^{\mathrm{N}\times\mathrm{N}}$ is the global Resolvent matrix:

$$\mathscr{R} = (i\omega\mathbf{I} - \mathbf{J})^{-\mathbf{1}} \tag{3.23}$$

$\mathbf{I}$ is the identity matrix, and the global-Resolvent matrix is defined for any real frequency ω since all eigenvalues of $\mathbf{J}$ are strictly damped.

The relation in equation (3.22) gives access, for a given frequency, to the harmonic response of the system when forced with a harmonic forcing of a given spatial form. We now introduce the gain G, function of the external forcing $\hat{\mathbf{f}}$, that is defined for every frequency as the ratio between the energy of the response and the energy of the forcing itself.

$$G(\hat{\mathbf{f}}) = \frac{\langle\hat{\mathbf{w}},\hat{\mathbf{w}}\rangle_{\mathbf{Q_e}}}{\langle\hat{\mathbf{f}},\hat{\mathbf{f}}\rangle_{\mathbf{Q}}} \tag{3.24}$$

For the forcing, the scalar product $\langle\cdot,\cdot\rangle_{\mathbf{Q}}$ is a discrete inner-product in $\mathbb{C}^{\mathrm{N}}$ based on a positive definite hermitian matrix $\mathbf{Q}$ such that:

$$\langle\mathbf{u},\mathbf{v}\rangle|_{\mathbf{Q}} = \mathbf{u}^*\mathbf{Q}\mathbf{v} \tag{3.25}$$

where * denotes conjugate transpose. The associated norm $\|\mathbf{u}\|_{\mathbf{Q}} = \sqrt{\langle\mathbf{u},\mathbf{u}\rangle|_{\mathbf{Q}}}$ will be used. For the flow response, as we want the numerator of the gain function (3.24) to be the kinetic energy $E = \int(u^2+v^2)\mathrm{d}x\mathrm{d}y$ of the response $\hat{\mathbf{w}}$, we define a pseudo scalar product $\langle\cdot,\cdot\rangle_{\mathbf{Q_e}}$ such that

$$\langle\mathbf{w},\mathbf{w}\rangle|_{\mathbf{Q_e}} = \mathbf{w}^*\mathbf{Q_e}\mathbf{w} = E \tag{3.26}$$

The computation of the matrix $\mathbf{Q}$ and $\mathbf{Q_e}$ is given in section 3.3.2, where we show in particular that the matrix is real, symmetric and semi-definite positive.

Among all the possible perturbations, we are looking for the forcing that causes the strongest response in the flow, thus the forcing which maximises the gain function, called the optimal forcing. Inserting equation (3.22) into (3.24) we obtain:

$$G_{max}(\hat{\mathbf{f}}) = \sup_{\hat{\mathbf{f}}} \frac{\langle \mathscr{R}\hat{\mathbf{f}}, \mathscr{R}\hat{\mathbf{f}} \rangle_{\mathbf{Q_e}}}{\langle \hat{\mathbf{f}}, \hat{\mathbf{f}} \rangle_{\mathbf{Q}}} = \sup_{\hat{\mathbf{f}}} \frac{\langle \hat{\mathbf{f}}, \mathscr{R}^\dagger \mathscr{R}\hat{\mathbf{f}} \rangle_{\mathbf{Q_e}}}{\langle \hat{\mathbf{f}}, \hat{\mathbf{f}} \rangle_{\mathbf{Q}}} \tag{3.27}$$

where $\mathscr{R}^\dagger$ is the adjoint operator. The previous ratio is a Rayleigh quotient since $\mathscr{R}^\dagger\mathscr{R}$ is an Hermitian matrix. For each frequency ω, this optimisation problem, that leads to the so-called optimal forcing, can be solved by using the singular-value decomposition of the global Resolvent $\mathscr{R}(\omega)$, given by:

$$\mathscr{R}^\dagger\mathscr{R}\hat{\mathbf{f}} = \lambda^2\hat{\mathbf{f}} \tag{3.28}$$

The optimal gain λ^2 is real and corresponds to the singular value of the global Resolvent $\mathscr{R}(\omega)$. In equation (3.28) the real eigenvalue λ^2 is related to the forcing $\hat{\mathbf{f}}$ of unit norm, and λ_{max} is related to the optimal forcing that maximises the gain function.

The gain function quantifies if the flow acts like a high-, low- or broad-band filter. The evolution of the gain, function of the frequency forcing, is given by the evolution of the most energetic eigenvalue λ_{max} of the global Resolvent $\mathscr{R}$. Once this optimal forcing has been computed, the associated optimal response $\hat{\mathbf{w}}$ can be obtained solving (3.22), that for the specific case reduces to $\hat{\mathbf{w}} = \mathscr{R}(\omega)\hat{\mathbf{f}}$.

Note that the gain G corresponds to the ratio of two quantities of different physical dimensions: the numerator refers to the kinetic energy of the response, whilst the denominator is an integration of the forcing over the domain. The gain G has been chosen because the optimisation problem introduced above is mathematically well-posed. The physical meaning of the gain G has been discussed by Sipp and Marquet (2012) through an energetic input-output approach on a transitional boundary-layer developing on a flat plate.

3.3.2 Numerical strategy

The global Resolvent discussed in this section is straightforwardly obtained, for each frequency ω, once we have the Jacobian matrix, derived in equation (3.17).

Scalar product Q

Let us consider two continuous complex functions $\mathbf{f}, \mathbf{g}$: $\Omega \in \mathbb{R}^{\mathrm{N}} \rightarrow \mathbb{C}^{\mathrm{N}}$. The domain Ω which corresponds to the mesh is discretised such that $\Omega = \bigcup_{i=1,N} \Omega_i$, and we designate by $\mathbf{F} \in \mathbb{C}^{\mathrm{N}}$ and $\mathbf{G} \in \mathbb{C}^{\mathrm{N}}$ the complex vectors corresponding to the discrete form of the functions $\mathbf{f}$ and $\mathbf{g}$ on $\bigcup_{i=1,N} \Omega_i$.

The discrete inner product $\langle \cdot, \cdot \rangle_{\mathbf{Q}}$ in equation (3.25) is defined as the discretisation of the continuous inner product inducing the $\mathcal{L}^2$ norm. That is:

$$\int_{\Omega} \mathbf{f}^* \mathbf{g} \mathrm{d}\mathbf{\Omega} = \sum_{\mathbf{i=1,N}} \mathbf{F_i^* G_i \Omega_i} = \mathbf{F^* Q G} = \langle \mathbf{F}, \mathbf{G} \rangle|_{\mathbf{Q}} \tag{3.29}$$

As a consequence, $\mathbf{Q}$ is a real diagonal matrix whose terms Q_i correspond to the volume Ω_i of the discretised cell i.

Scalar product $\mathbf{Q_e}$

Let us consider the two-dimensional laminar response at a given cell location of our mesh $\hat{\mathbf{w}} = [\rho', (\rho u)', (\rho v)', (\rho E)']^T$. As the response corresponds to small perturbations of the base-flow conservative variables, we will denote the fluctuation with $'$ to differentiate them from the base flow values. We aim at computing the kinetic energy $E = \int (u'^2 + v'^2) \mathrm{d}\Omega$ of the response at the considered cell of volume Ω. At first order we have:

$$(\rho u)' = \rho' u + \rho u' \tag{3.30}$$

$$(\rho v)' = \rho' v + \rho v' \tag{3.31}$$

In particular,

$$\begin{aligned} u'^2 &= (\rho', \rho' u + \rho u') \begin{pmatrix} a & b \\ c & d \end{pmatrix} \begin{pmatrix} \rho' \\ \rho' u + \rho u' \end{pmatrix} && (3.32) \\ &= a\rho'^2 + b\rho'^2 u + b\rho\rho' u' + c\rho'^2 u + d\rho'^2 u^2 + && (3.33) \\ &+ d\rho\rho' u u' + c\rho\rho' u' + d\rho\rho' u u' + d\rho^2 u'^2 && (3.34) \end{aligned}$$

which by identification leads to:

$$a = u^2/\rho^2, \quad b = -u/\rho^2, \quad c = -u/\rho^2, \quad d = 1/\rho^2 \tag{3.35}$$

Therefore the energy matrix Q_e is given by:

$$u'^2 + v'^2 = \hat{\mathbf{w}}^* \begin{pmatrix} \frac{(u^2+v^2)\Omega}{\rho^2} & -\frac{u\Omega}{\rho^2} & -\frac{v\Omega}{\rho^2} & 0 \\ -\frac{u\Omega}{\rho^2} & \frac{\Omega}{\rho^2} & 0 & 0 \\ -\frac{v\Omega}{\rho^2} & 0 & \frac{\Omega}{\rho^2} & 0 \\ 0 & 0 & 0 & 0 \\ 0 & 0 & 0 & 0 \end{pmatrix} \hat{\mathbf{w}} \tag{3.36}$$

The matrix Q_e is real, symmetric, and by definition semidefinite positive. Once all the matrices are obtained, the eigenvalue problem in equation (3.28) can be solved

using the algorithm of Lanczos and matrix inversions are obtained as described in section 3.2.2. Note that solution of the eigenvalue problem in equation (3.28) is found up to a multiplicative constant: we will only focus on the spatial structures of those modes.

3.3.3 Energy maximisation on the whole domain

We present here the results that have been obtained by choosing the scalar products in equation (3.24) without any restriction on the surface where we want to maximise the kinetic energy of the response: the scalar product in (3.26) is computed considering the whole domain Ω. The forcing is referred only to the momentum variables and is applied on the whole domain, perturbing thus at the same time the incoming boundary layer, the shock and the mixing-layer regions.

Gain function

The evolution of the three most energetic singular values of the global Resolvent, function of the forcing frequency, is presented in figure 3.15. In the range $1 - 8000$ Hz (Strouhal number between 10^{-4} and 1) the singular value λ_1 is always much greater than the other singular values λ_2 and λ_3, indicating that the flow dynamics in the frequency range where our study is focused on can be represented just by the most energetic λ_i.

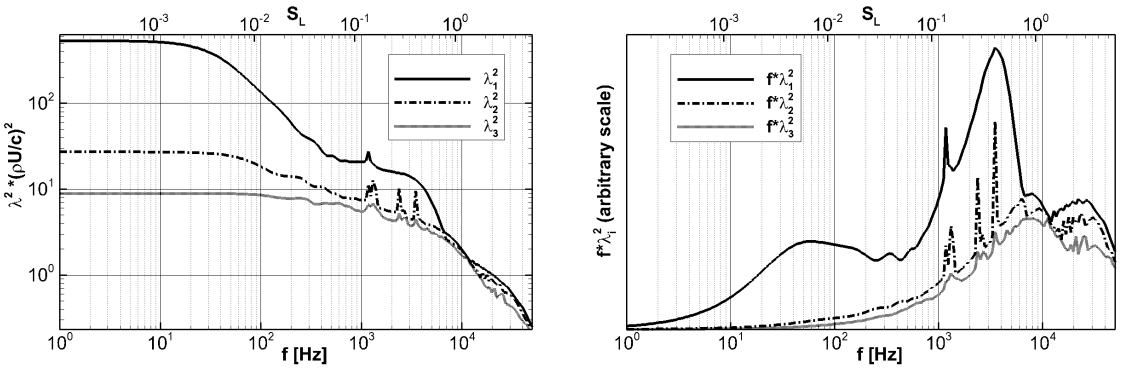

(a) Gain function, logarithmic scale.

(b) Normalised premultiplied optimal gain.

Figure 3.15: Most energetic singular values of the global Resolvent. Each λ_i represents the gain when the flow is forced, at the frequency f, with an optimal forcing.

The physical dimension of the singular values of the global Resolvent is given by the ratio between a kinetic energy and the time-derivative of momentum, both integrated on the domain. In order to ease the comparison with other studies, it is useful to normalise this quantity: in figure 3.15 as well as in all future plots,

the gain function has been normalised dividing the eigenvalues by a characteristic time and multiplying by a characteristic density. The first quantity is given by the ratio between the length of the bump $c = 0.286$ m and the reference velocity U_{ref} (the same used to compute the Strouhal number), whilst the second one is the flow density in the interaction zone, where $u = U_{ref}$, that is $\rho_{ref} = 0.73$ kg/m^3.

The value 1 of this particular gain function does not define a threshold between damping and amplification: the role of the gain curve is to indicate if there is a preferred range of frequencies associated to a strong response. In other words, if the flow is perturbed with a broadband environmental noise, it is more likely that the unsteadiness of the flow caused by that noise is located in the range of frequencies where we have strong gains.

Figure 3.15 also shows that the gain function is not constant, but is more energetic for low frequencies up to 50 Hz, then decreases rapidly to another plateau for $1 - 4$ kHz. The physical interpretation relies on the frequency-selection process typical of this noise amplifier configuration: if we force the flow with an optimal forcing at different frequency, the response is more energetic when we consider low frequencies up to 50 Hz, and medium frequencies in the range of $1 - 4$ kHz. The weighted gain in figure 3.15b presents a peak near $f = 50$ Hz, that indicates the frequency below which the gain function, or the PSD as observed in other studies (Dupont et al., 2006), has a slope of -1.

If we observe the gain behaviour at higher frequencies, we can notice a third bump in figure 3.15b starting from 10 kHz. This rise in the gain function could be associated to high-frequency motions related to turbulent fluctuations, but as the proposed model relies on a base flow that is solution of RANS equations, it is not legitimate to discuss the turbulence-related motions as they are introduced through the S-A turbulence model.

Low-frequency

The optimal forcing is shown in figure 3.16a: it is located mostly in the boundary layer on the divergent part of the bump and has its highest value on the shock foot. Starting from the top of the bump, where the flow becomes supersonic, the optimal forcing forms an oblique pattern that bounces upstream on the upper sonic line and then hits the shock foot.

To investigate the nature of this line we consider the well-known theory of characteristics (Liepmann, 1957): in the supersonic region inside the $M = 1$ line, outside the boundary layer, the viscous forces are negligible, and the equations of motions reduce to the Euler equations. The hyperbolic equations governing the compressible flow can be recast in the characteristic form. The main result of this approach is

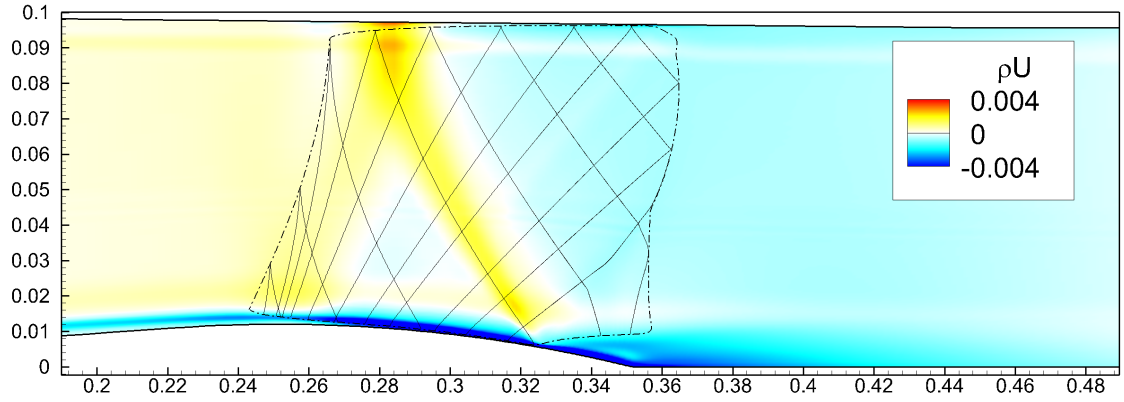

(a) Optimal forcing, frequency $f = 50$ Hz.

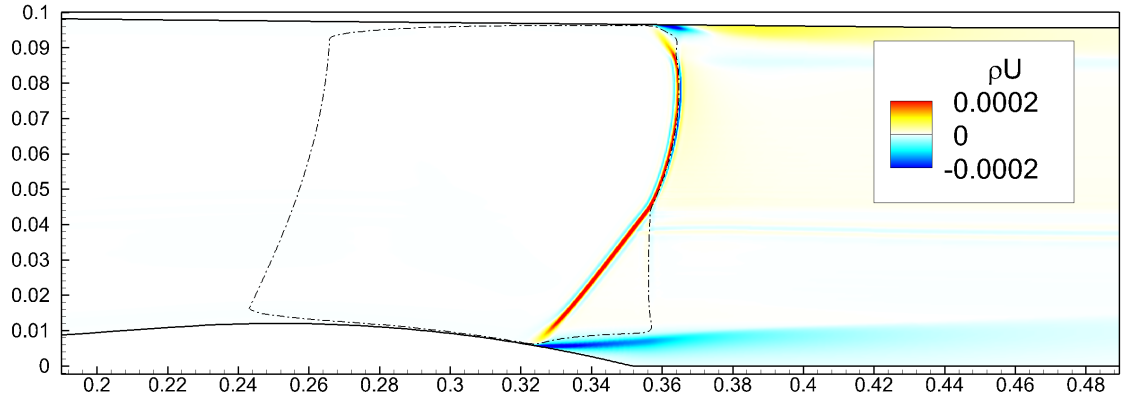

(b) Optimal response, frequency $f = 50$ Hz.

Figure 3.16: Real part of the optimal forcing and associated optimal response.

the existence of some typical lines, called the characteristic lines, along which information propagates inside the supersonic flow. The slope of those characteristic lines with respect to the flow direction is given by

$$\gamma = \pm \tan^{-1} \sqrt{\frac{1}{M^2 - 1}} \tag{3.37}$$

Figure 3.16a shows the superposition of the optimal forcing with the left and right characteristic lines, associated to the negative and positive sign in equation (3.3.3), respectively. The oblique part of the forcing follows exactly the right characteristic line that impacts on the shock foot, where the recirculation bubble begins. This feature can be interpreted as follows: the separation point has a fundamental importance in the dynamics of the flow, and forcing its position can influence the whole dynamics. As the information propagates along the characteristic lines, the optimal forcing is energetic in the zone of the flow where a perturbation can propagate and impact the separation point.

The real part of the optimal response for low-frequency forcing is presented in figure 3.16b: the mode is located mostly on the shock wave, with a spatial form

similar to what has been observed for the low-frequency Fourier mode of figure 2.22. Moreover, although less marked, the response is also located in the core of the mixing layer, with a horizontal structure of large wavelength: the low-frequency response is associated to a *breathing* of the recirculating bubble. The presence of a negative value of the mode in the mixing layer, associated to a positive value in the shock, indicates that the contraction of the bubble is related to a downstream motion of the reflected shock, whereas its expansions are related to intense reverse flow and, consequently, upstream motion of the reflected shock. This observation is consistent with the model proposed by Piponniau et al. (2009).

Medium-frequency

Following the same steps, we consider now a medium-frequency optimal forcing and its induced response, presented in figure 3.17. The optimal forcing has now a more elaborated spatial structure, but is still located both in the supersonic zone before the shock and at the beginning of the mixing layer. Moreover, the maximum value is again at the shock foot, where the pressure gradient causes the separation of the boundary layer. Here the optimal forcing is no longer located along the characteristic lines as for the optimal forcing at low frequency.

One can notice similarities of the optimal forcing and optimal response spatial structures with those obtained by Marquet et al. (2008a) on an incompressible rounded backward-facing step: we observe the Orr (Orr, 1907) and Kelvin-Helmholtz (Drazin and Reid, 1980) mechanisms respectively at play in the forcing and response. The medium-frequency forcing induces a response (figure 3.17b) that is mainly located after the interaction: the structures of the response start from the separation point around $x = 0.33$ mm and display a small wavelength: the size of the structure is small if compared to the size of the recirculation bubble, visible in figure 3.4, indicating that the medium-frequency unsteadiness is associated to the so-called flapping motion of the shear layer (Kiya and Sasaki, 1983).

The mode is still present but less visible in the shock wave: the physical interpretation relies on the fact that the most energetic response is in the mixing layer and that, as confirmed by the spectra in figure 2.18, it is the dominant medium-frequency motion. Moreover the mode wavelength inside the shock can be related to the convection velocity: the shock wave occurs at $u = 420$ m/s and the speed of sound is $a = 320$ m/s. Considering a convective velocity given by the difference between the speed of the flow and the speed of sound, we can estimate a wavelength $L = (u - a)/f$ of 30 mm for the considered frequency, that compares favourably with figure 3.17b. This results is consistent with the observation made by Robinet (2007), who found that when an oblique shock is disturbed, the perturbations

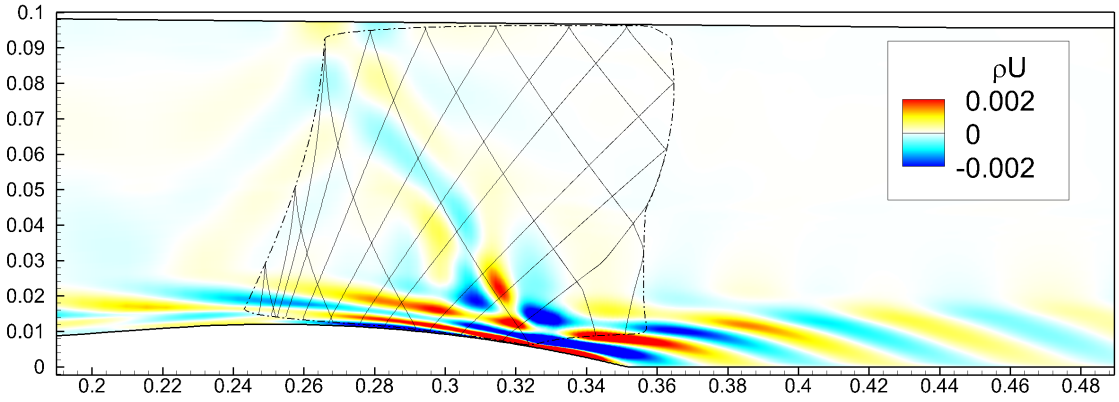

(a) Optimal forcing, frequency $f = 4000$ Hz.

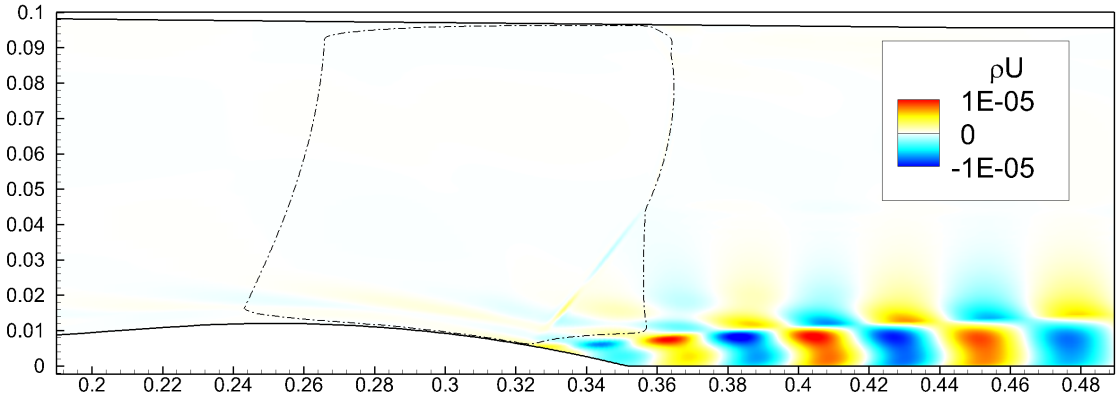

(b) Optimal response, frequency $f = 4000$ Hz.

Figure 3.17: Real part of the optimal forcing and associated optimal response.

propagate along the shock.

Density effects

Figure 3.18 shows the optimal response on the variable ρ: the spatial structure of the response indicates that the mode is located on the shock for low-frequency forcing and on the separated zone for medium-frequency, as previously mentioned for the variable ρU. However, considering the low-frequency mode, unlike figure 3.16b, the optimal response on the density (figure 3.18a) indicates that the second shock leg exhibits low-frequency unsteadiness as the other part of the shock, confirming the experimental result in the left part of figure 2.22. Near the separation point, the medium-frequency mode is less energetic, suggesting that the breathing of the bubble is linked to velocity fluctuation more than density perturbation.

For medium-frequency motions, figure 3.18b indicates again that Kelvin-Helmholtz instability characterises the mixing-layer zone, as previously inferred from figure 3.17b. In comparison with the mode on ρU, the response on the density component

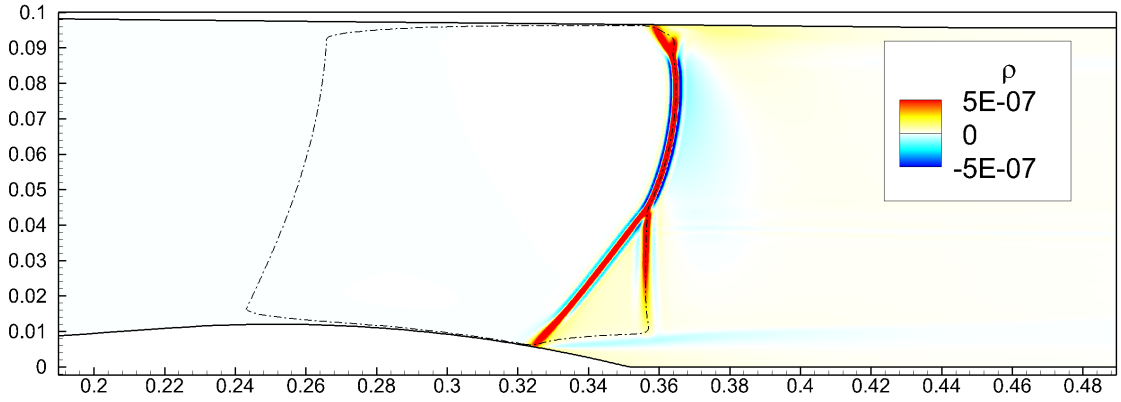

(a) Optimal response, frequency $f = 50$ Hz.

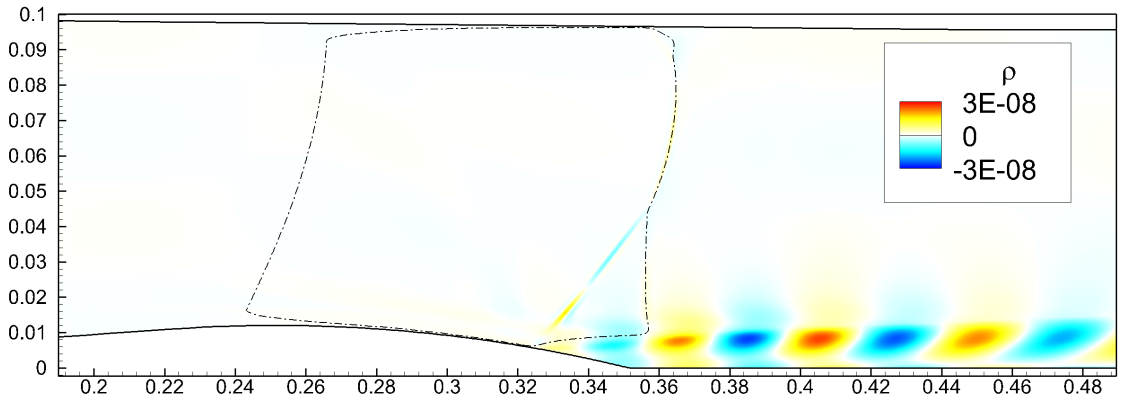

(b) Optimal response, frequency $f = 4000$ Hz.

Figure 3.18: Real part of the density component for the optimal response.

is more localised in the centre of the mixing layer, without significant contribution at the wall. If we compare this result with the correlation map in figure 2.24 obtained with Schlieren photography we can recognise a similarity in the pattern of the structure: although the experimental result does not rely on the flow density but on its gradients, in both cases we can observe periodical round structures that develop starting from the separation point. Moreover, the wavelength of those structures associated to an optimal response at 4000 Hz is of the same order of magnitude as the experimental one (see figure 2.26).

Acoustic resonances

For both low- and medium-frequency forcing, the optimal response resulting from the linearised approach compares favourably with the experimental investigation of chapter 2. In contrast with the experimental data, an isolated peak, located around $f = 1200$ Hz and its multiples, is visible in the gain function for all the singular values and indicates a resonance frequency. To investigate the nature of this peak

we consider again the *wall-slip* configuration introduced in section 3.1, where a slip condition at both walls avoids the development of the boundary layers.

For this configuration we obtain a new gain function, visible in figure 3.19a: the acoustic peaks are now more visible, and the gain function for the most energetic eigenvalue indicates that the resonance frequency does not change when not considering the boundary layers. The high value of the gain in the peaks indicates that for these frequencies the flow is very sensitive to external forcing, and the responses show (see figure 3.19) that acoustic resonance mechanisms are responsible for these phenomena.

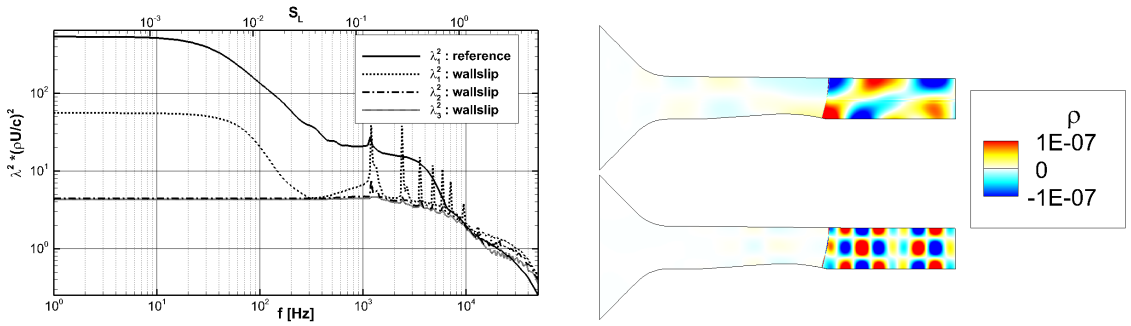

(a) Gain function. (b) Optimal responses at different frequencies.

Figure 3.19: Acoustic resonance on the configuration without the boundary layers.

The optimal responses associated to the resonance frequencies for this particular slip configuration are presented in figure 3.19b for the two first resonant peaks at $f \approx 41200$ Hz and $f \approx 2400$ Hz. For both frequencies, even if the optimal forcing and its response are located everywhere in the domain, only the zone after the shock has a significant energy content. Regarding the size of the structures in the modes, here again we can relate the response wavelength to the convection velocity through $L = |u - a|/f$, where u is the local flow speed. Furthermore, the structure of the optimal responses of figure 3.19b indicates that the mode actually corresponds to an acoustic resonance mode linked to the channel height and not to the channel length (Koch, 1985).

One can notice a similarity in the spatial structure between the optimal responses of figure 3.19b and the least stable global mode of figure 3.11: a part from the shock shape, which has been modified by the interaction with the boundary layer, both analyses (Jacobian eigenvalues and Resolvent singular values) highlight the acoustic resonances, with a fair agreement on the frequency prediction. This indicates that the acoustic phenomena in the channel-flow configuration cannot be neglected when studying the flow properties. However, the stability analysis based on the global Resolvent can describe the frequency-selection mechanism that cause shock

unsteadiness and Kelvin-Helmholtz type instabilities, while global-mode decomposition fails to predict both the low-frequency and medium-frequency motions.

Considering again the entire gain function, the evolution of the first singular value in the configuration without boundary layer still indicates a high gain for low-frequencies: the energy content of the optimal response remains high even without the separation, suggesting that low-frequency unsteadiness linked to the shock motions has an inviscid nature. This implies that low-frequency shock oscillations could be observed as a consequence of a broadband noise. In this case, even without the boundary layers in the incoming flow or the recirculation zone after the separation, the shock would amplify existing environmental broadband noise and react preferentially with low-frequency motions.

Finally, comparing the gain function with the reference configuration (solid line in 3.19a), one can notice that λ_1 is less energetic in the configuration without boundary layers: this could be due to the absence of the lambda shock as well as the mixing layer contribution (as can be seen in figure 3.18a) or to the different shock strength. Moreover, the grid spacing in the vertical direction changes between the *wall-slip* configuration and the reference. As it shown in section 3.1.2 and discussed in next paragraph, the grid spacing has a strong influence on the internal shock structure and on the singular values at low-frequencies.

Grid convergence

Similarly to previous sections, the grid dependency is verified with the introduction of four additional grids: two coarser (mesh 1 and mesh 2) and two finer (mesh 3 and mesh 4) meshes.

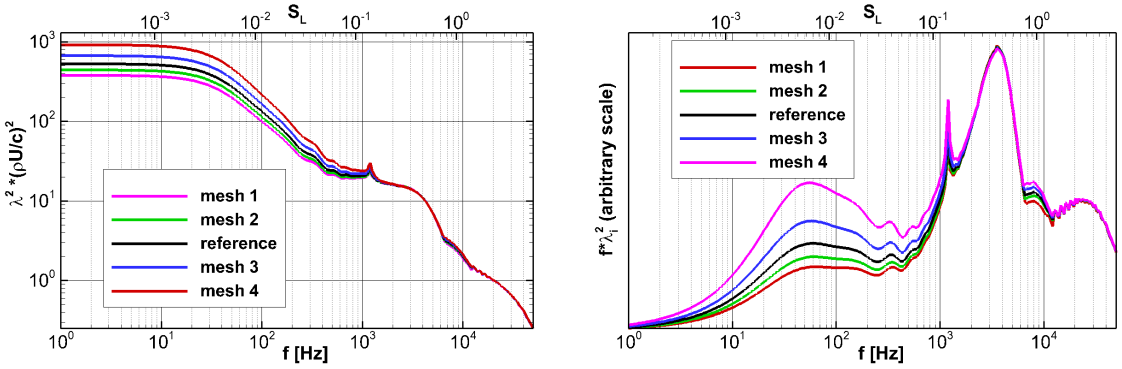

(a) Gain function, logarithmic scale.

(b) Normalised premultiplied optimal gain.

Figure 3.20: Gain function for different computational grids.

Figure 3.20 shows the superposition of the gain curves obtained with the grids described in section 3.1.2. Is it seen that the medium- and high-frequency motions

are well converged while some strong discrepancies remain at low-frequencies. The differences between the curves at low-frequency are more pronounced than those observed in modes distributions in the eigenvalue decomposition (figure 3.12a).

As previously shown, low-frequency gain is associated to a response in the shock wave, whose thickness is linked to the grid resolution. More importantly, a finer grid yields high values of density derivatives on the shock, as shown in figure 3.3. For low frequency, the most energetic eigenvalues of the global Resolvent are entirely on the shock: the consequence is a strong dependency on the grid refinement. This behaviour is even more remarkable when observing the weighted gain in figure 3.20.

The vertical shift associated to different grids in the gain function is equivalent to the horizontal shift in the spectra of figure 3.12a. A part from the discrepancy of the value of λ for low-frequency, the gain function still shows the behaviour observed in the previous section with the characteristic low-pass filter behaviour and a bump for high-frequencies. Moreover, medium-frequency λ values are not impacted by the grid refinements, and show the same peaks in frequency even in the weighted gain of figure 3.20.

3.3.4 Energy maximisation on a sub domain

Even if the forcing highest value is always located, for the discussed frequencies, in the shock foot region, a great amount of forcing is present both in the supersonic field upstream of the shock and in the mixing layer above the recirculation bubble. The investigation previously discussed, although capable of reproducing the experimental results of chapter 2, does not indicate the source of the unsteadiness, and whether if it is legitimate to suppose that the source is unique.

In order to analyse separately the receptivity mechanism associated to different zones of the flow (upstream boundary layer, recirculation bubble and shock wave), we consider now a gain function maximisation as introduced in equation (3.27), but using a restrained forcing term $\hat{\mathbf{f}}_\mathbf{s} \in \mathbb{S}$ that evolves in a subspace $\mathbb{S} \in \mathbb{C}^\mathrm{M} \subset \mathbb{C}^\mathrm{N}$ with $\mathrm{M} < \mathrm{N}$ of the flow configuration: the surface where the response kinetic energy is maximised is still the whole field, but the optimal forcing is now located only in a *subspace* of the entire domain, defined through a mesh subset, in order to exclude one or more elements of the interaction. The *sub-optimal* forcing is then applied on the momentum variables, as previously.

We thus introduce a prolongation matrix $\mathbf{P} \in \mathbb{C}^{\mathrm{N}\times\mathrm{M}}$ such that if $\hat{\mathbf{f}}_\mathbf{s} \in \mathbb{S}$ then $\mathbf{P}\hat{\mathbf{f}}_\mathbf{s} \in \mathbb{C}^\mathrm{N}$, whose action is to add 0 to the restricted term. Similarly we define the restriction matrix $\mathbf{P}^*$ such that if $\hat{\mathbf{f}} \in \mathbb{C}^\mathrm{N}$ then $\mathbf{P}^*\hat{\mathbf{f}} \in \mathbb{S}$. Note that by definition of these matrices we have: $\mathbf{P}^*\mathbf{P} = \mathbf{I}$. In particular, the response $\hat{\mathbf{w}}$ now verifies:

$$\hat{\mathbf{w}} = \mathscr{R}_\omega \mathbf{P}\hat{\mathbf{f}}_\mathbf{s} \tag{3.38}$$

The energy maximisation (3.27) remains a generalised Rayleigh quotient whose solution is given by:

$$\mathscr{R}_\omega^* \mathbf{Q}_\mathbf{e} \mathscr{R}_\omega \mathbf{P}\hat{\mathbf{f}}_\mathbf{s} = \lambda^\mathbf{2} \mathbf{Q}\mathbf{P}\hat{\mathbf{f}}_\mathbf{s}. \tag{3.39}$$

The solutions $\hat{\mathbf{f}}_\mathbf{s}$ of this eigenvalue problem are thus sought in the subspace $\mathbb{S}$ and then extended to our configuration with $\hat{\mathbf{f}} = \mathbf{P}\hat{\mathbf{f}}_\mathbf{s}$.

The main purpose of this subspace investigation is to isolate the unsteadiness: it has been shown that the shock acts as a low-pass filter of the external noise and the separation bubble is prone to both low and medium-frequency unsteadiness, but the forcing that caused each response was located in the whole domain. Following the different theories on the origin of SWBLI unsteadiness discussed in the introduction, we defined three zones, called subspaces, where we localise the optimal forcing.

These zones correspond the incoming boundary layer upstream of the shock wave, the recirculation bubble generated by the separation after the end of the bump, and a large zone that includes both the supersonic flow before and after the shock, but excludes the boundary layer and the separated zone. A sketch of these regions is presented in figure 3.21, where the solid black lines represent the velocity field of the base flow and indicate the shock position.

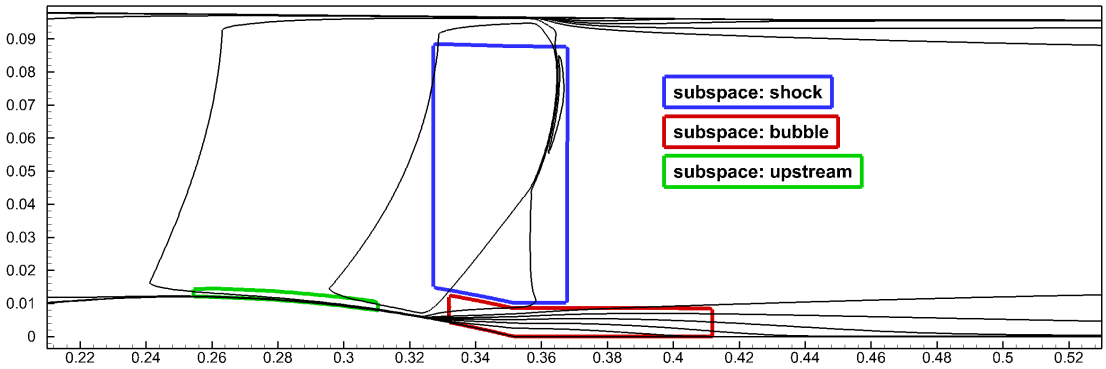

Figure 3.21: Sub-domains used for local energy maximisation, indicated in different colour. The solid lines indicate the base-flow velocity field.

The gain functions obtained using different subspaces are plotted in figure 3.22a. The main effect of the subspace is to reduce the energy gain, suggesting the trivial result that the more we force the flow, the more convective unsteadiness can be triggered. The strong difference in curves level is mainly caused by the fact that the subspaces do not involve the same surface area, so the values of λ are not comparable between the different cases.

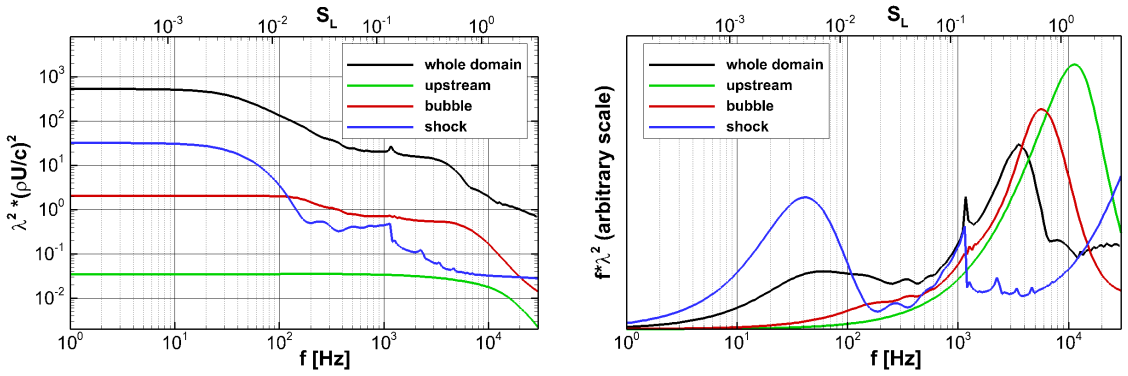

(a) Optimal gain, most energetic eigenvalue. (b) Normalised premultiplied optimal gain.

Figure 3.22: Gain function when the forcing is in different domains of the interaction.

For the subspace in the shock region, the λ reduction mostly affects the medium-frequency content of the gain, and an abrupt decrease is observed after the acoustic peak close to 1.2 kHz: the gain function is similar to that obtained for the configuration without boundary layers, confirming the low-pass filter behaviour of the shock wave, and also indicating that medium-frequency unsteadiness is linked to the separated region and cannot be triggered by forcing only the shock wave.

For the subspace in the recirculation zone (called *bubble*), the shape of the gain curve presents a behaviour similar to the *whole domain* configuration: the gain is most energetic for low-frequency, and the small bump is observed in the same medium-frequency range as the configuration without subspaces. This indicates that the mixing-layer zone is sensitive both to low- and medium-frequency forcing. If we consider now a subspace in the incoming boundary layer (called *upstream*), the associated gain function, green line in figure 3.22, shows that the frequency-selection process is no more present like in the other cases: an optimal forcing in this zone will not be able to trigger the low-frequency unsteadiness more than the medium-frequency.

Figure 3.22b presents the "premultiplied gain", where the product between the eigenvalue associated to the optimal forcing and the forcing frequency has been divided by a scale factor to ease the comparison. This plot indicates that the low-frequency unsteadiness has a preferred frequency between 40 and 60 Hz. The response associated to a forcing in this frequency range, linked to shock unsteadiness, is obviously more energetic when the forcing is imposed on the shock wave. However, this response is still present for the other configurations except when the forcing is on the incoming boundary layer.

If we focus on higher values of f, one can observe that when the subspace is in the recirculation zone, the peak on the weighted gain is shifted towards higher

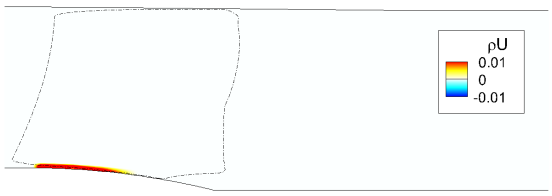

(a) Optimal forcing, $f = 50$ Hz.

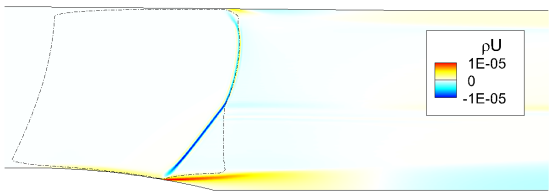

(b) Optimal response, $f = 50$ Hz.

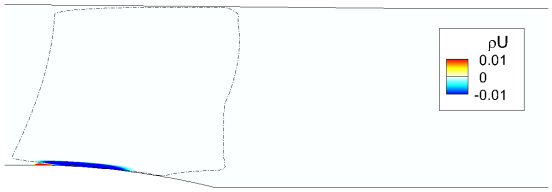

(c) Optimal forcing, $f = 4000$ Hz.

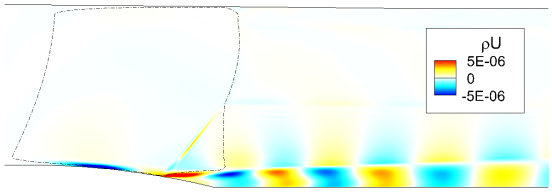

(d) Optimal response, $f = 4000$ Hz.

Figure 3.23: Subspace in the incoming boundary layer.

frequencies with respect to the configuration without subspace, but still in a range that compares favourably with the experimental results. When the subspace is in the shock wave, medium-frequency unsteadiness is not triggered. Regarding the gain function obtained when the forcing is in the incoming boundary layer, as mentioned for figure 3.22a, the energetic content of the response drops for frequencies higher than 10 kHz, suggesting that there is no preferred unsteadiness for this spatial form of the forcing.

However, the fact that there is no peak for medium-frequencies in this configuration does not mean that a forcing in this zone cannot trigger the medium-frequency instability: figure 3.23 presents the optimal forcing and associated response when the subspace is in the incoming boundary layer. In figure 3.23a and 3.23c one can see that the forcing is located only in a subset of the domain corresponding to the supersonic boundary layer on the bump. Figure 3.23b indicates that the low-frequency response is on the shock as for the configuration without subspace, even if the shock top il less energetic than the shock leg.

Considering the optimal response to medium-frequency perturbations (figure 3.23d), imposing a forcing only in the incoming boundary layer yields a Kelvin-Helmholtz type instability in the mixing layer as in the configuration without restrictions, despite the reduced size of the forcing.

A very similar behaviour is observed when the forcing is only in the mixing-layer zone (figures 3.24a and 3.24c): even if we do not impose the forcing directly on the shock, the perturbation can propagate upstream and trigger the shock unsteadiness. However, as for the previous case, the energy of the response in the upper part of the shock is smaller than in the lower part, suggesting that a perturbation located

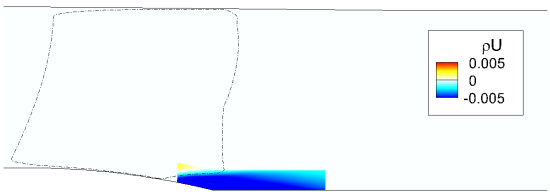

(a) Optimal forcing, $f = 50$ Hz.

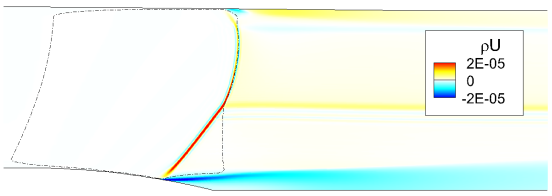

(b) Optimal response, $f = 50$ Hz.

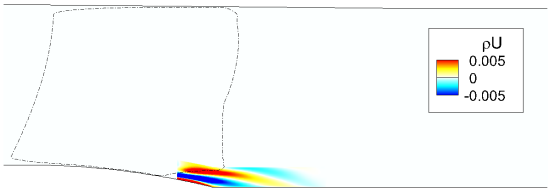

(c) Optimal forcing, $f = 4000$ Hz.

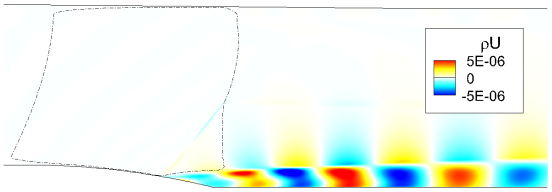

(d) Optimal response, $f = 4000$ Hz.

Figure 3.24: Subspace in the recirculation zone.

only on the bubble or in the incoming boundary layer does not cause a solid shock motion but rather oscillations of the shock leg.

As for the configuration with the perturbation localised only in the boundary layer upstream of the interaction, the low-frequency unsteadiness can be triggered without imposing a forcing directly on the shock wave, indicating that the shock is the mirror of the physical phenomena around him.

Considering figure 3.24d, the optimal response to medium-frequency perturbation of the mixing layer causes a Kelvin-Helmholtz type instability as for the configuration without subspace. This result is not surprising since we are forcing directly in the mixing layer zone.

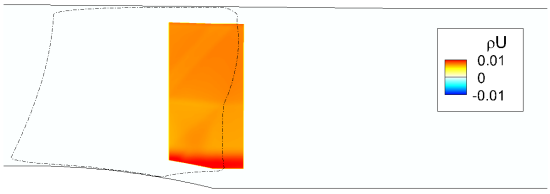

(a) Optimal forcing, $f = 50$ Hz.

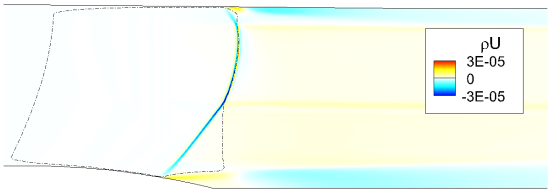

(b) Optimal response, $f = 50$ Hz.

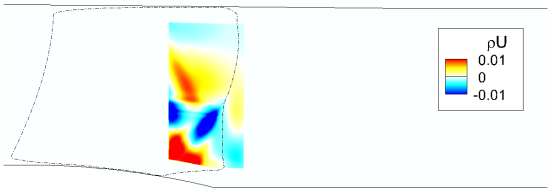

(c) Optimal forcing, $f = 4000$ Hz.

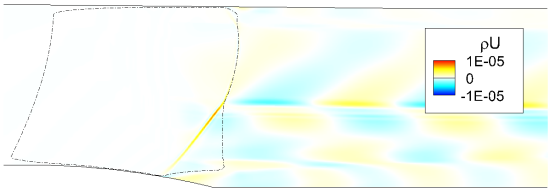

(d) Optimal response, $f = 4000$ Hz.

Figure 3.25: Subspace in the shock wave.

Figure 3.25 presents the final case of the subspace in the shock region, when the forcing (figures 3.25a and 3.25c) is not applied on the boundary layer or the separated region. Obviously the shock presents low-frequency response when excited with low-frequency: this response is uniformly distributed along the entire shock wave. However, forcing the shock with medium-frequency perturbations does not produce a response in the mixing layer, indicating that perturbations in the shock region are not able to trigger the unsteadiness to the separated zone.

This last observation confirms that the shock has a low-pass filter behaviour: if a local forcing is applied to it without involving the separated zone, the shock is not capable to trigger Kelvin-Helmholtz type instabilities in the mixing layer, and acts like a filter to medium-frequency perturbations.

3.4 Conclusions

The aim of the numerical investigation proposed in this chapter was to examine the transonic flow over the Délery bump using numerical simulation and stability analysis. The configuration experimentally investigated in chapter 2 is initially analysed using RANS simulation: the choice of the model is discussed with respect to the scale decoupling assumption, and the results are discussed in terms of grid convergence. In particular, we showed that the shock thickness is sensitive to the spatial resolution of the domain.

The mean flow obtained using a local time stepping approach is in accordance with PIV results presented in section 2.1. The solution gives a complete description of the transonic interaction, within the limitations of RANS approach (Knight and Degrez, 1998). When integrating the equation in time, URANS simulation converge to a steady state, and therefore fails to predict the unsteady behaviour of the interaction: no unsteadiness is found in the shock region nor in the mixing layer.

A stability analysis is then considered: the RANS equations are linearised around the base flow obtained with RANS simulation, and the Jacobian matrix is computed using residual evaluation in a discrete framework. The eigenvalue decomposition of the linear operator indicates that, contrarily to Robinet (2007) and Touber and Sandham (2011), no unstable global modes are present when considering coupled equations, and the least-stable eigenvalues cannot be linked to the unsteady dynamics.

The spectrum presents robust grid convergence properties. It indicates that most of the stable global modes corresponds to acoustic resonances, and reveals some interesting results when neglecting the effect of the turbulence equation. However, as recognised in other papers (Sipp and Marquet, 2012), if the configuration is

stable, a global-mode decomposition poorly describes the dynamics of the flow: the spectrum can give some insight on the presence of low-frequency shock motions, but a different stability analysis is required to perform a thorough characterisation of the unsteady aspects of the considered SWBLI.

The global Resolvent is then introduced, and convective instabilities are analysed by observing the receptivity of the flow to external forcing. This approach highlights the frequency-selection process typical of globally stable flows, and indicates that the considered SWBLI behaves as a noise amplifier. As indicated by the gain function, there exists some optimal forcing that can trigger low-frequency oscillations in the shock region, while medium-frequency perturbations can cause unsteadiness in the mixing layer zone.

The optimal forcings are shown to be concentrated in the boundary layer both upstream and downstream of the shock foot. In the supersonic region, low-frequency forcings are also located along the right characteristic line that impinges on the separation point. Since in supersonic flows information travels along the characteristic lines, this indicates that low-frequency unsteadiness can be triggered by upstream perturbations, as long as they are in the boundary layer or on a characteristic line that communicates with the shock foot. However, low-frequency shock motions don't need an upstream source to be present, since it has been shown that a sub-optimal forcing localised only in the separated zone is able to cause unsteadiness.

Concerning higher frequencies, the gain function indicates that medium-frequency perturbations can trigger Kelvin-Helmholtz type instabilities. The optimal forcing is still located close to the shock foot, but a significant amount of forcing can be observed in the mixing layer. The optimal response is located only downstream of the separation, and no solid shock motions are observed.

By perturbing the flow on the restricted forcing locations, it has been shown that both the incoming boundary layer and the separated zone can trigger Kelvin-Helmholtz type instabilities, but the shock acts as a low-pass filter and is not capable to cause mixing-layer unsteadiness if forced at medium-frequencies.

Grid convergence studies indicates that the optimal gains are not converged at low frequencies because of the shock discretisation. Yet, the method is capable of reproducing the spatial form of both low and medium-frequency motions, suggesting that the proposed model is well adapted for the configuration and could be applied to different SWBLI.

Chapter 4

Flow over the OAT15A profile

In this chapter, we will consider another type of two-dimensional SWBLI in a transonic flow, where a normal shock causes the separation of the boundary layer over the OAT15A supercritical profile. When the angle of attack is small, the configuration presents some aspect similar to the channel flow discussed in the previous chapters: the interaction between the strong shock and the turbulent boundary layer on the suction side of the profile causes the separation of the flow, the shock is characterised by the lambda pattern and a recirculation bubble is observed downstream the shock foot. As it will be shown, the interaction embodies all the aspects that can be found in other types of SWBLI, exhibiting both low- and medium-frequency unsteadiness.

When the angle of attack exceeds a critical value, the flow presents low-frequency oscillations, known as shock buffeting. These oscillations differ from the low-frequency motions typical of SWBLI because they are periodic and have high-amplitude. The buffet phenomenon presents an industrial interest and has therefore been the subject of numerous studies in the past (Pearcey, 1958; McDevitt and Okuno, 1985; Lee, 1990): the shock unsteadiness is a strong phenomenon that can lead to catastrophic consequences, and is maintained without any external input of energy. However, the periodic motions are still much lower than the timescales of the wall-bounded turbulence, so a numerical simulation performed solving RANS equations is justified.

For these reasons, recent numerical studies have revealed that unsteady RANS simulations can successfully reproduce the buffet unsteadiness using different turbulence models (Barakos and Drikakis, 2000; Brunet, 2003; Deck, 2005; Thiery and Coustols, 2006). Despite some discrepancy with the experimental investigation on the critical angle of attack that determines the buffet onset, numerical simulations can provide a complete description of this particular SWBLI, including the low-frequency unsteady behaviour.

An attractive alternative to the time-integration of the URANS equations has been proposed by Crouch et al. (2007), who applied global-stability analysis to

the buffet problem on a NACA0012 profile. The linearised approach has shown that, unlike other type of SWBLIs, the low-frequency unsteadiness can be linked to a global instability as for a generic oscillator flow (Crouch et al., 2009). In this chapter we will follow a similar approach considering an OAT15A profile, and apply the method described in chapter 3 to characterise the flow unsteadiness using global mode and singular-value decomposition.

The configuration is introduced in section 4.1, where we present the experimental results of the investigation performed by Jacquin et al. (2009) on the same configuration. Then, a wide range of angles of attack is numerically investigated by means of RANS and URANS simulations (section 4.2), spanning from $\alpha = 2.5°$ to $\alpha = 7.0°$, showing that the low-frequency shock oscillations can be reproduced using a turbulence model. In section 4.3 we will show how direct and adjoint modes decomposition can describe the main features of the flow, and that the buffet phenomenon is linked to a global instability. Finally, in section 4.4 we present some results obtained when performing a singular-value decompositions of the global Resolvent. As for the channel-flow configuration, the approach indicates that convective instabilities can arise in the medium-frequency range regardless of the presence of the buffet phenomenon.

To scale the results with other SWBLI, the dimensionless frequency discussed in this chapter is obtained scaling with the chord $c = 230$ mm and the reference velocity $U_{ref} = 240$ m/s. This velocity corresponds to the speed of the undisturbed flow, where the Mach number is $M = 0.73$.

4.1 Experimental investigation

The experiments were conducted in the transonic S3Ch wind tunnel of ONERA, a continuous closed-loop facility powered by a 3500 kW two-stage fan. The model is an OAT15A supercritical aerofoil characterised by a $c = 0.23$ m chord length, relative thickness of 12.3% and a 0.78 m span. The central region of the wing is equipped with 68 static pressure taps and 36 unsteady Kulite transducers. In their investigation, Jacquin et al. (2009) considered several combinations of Mach number and angles of attack, adjusted by means of adaptable walls. In the numerical study, we will only consider $M = 0.73$ with variation of the incidence α. The stagnation conditions were near ambient pressure and temperature, and the Reynolds number based on the chord length is around $Re_c = 3 \times 10^6$. The boundary-layer transition was triggered on the model using a Carborundum strip located at $x/c = 0.07$ from the leading edge.

Figure 4.1a shows the mean distribution of the wall pressure coefficient C_p around

the profile for four angles of attack. The upper part of the curves, that corresponds to the suction side of the profile, is characterised by a pressure plateau before the compression caused by the shock. Starting from $\alpha = 3.5°$ this pressure jump is smeared out along the profile, indicating an unsteady position of the shock. In figure 4.1a one can also observe the effect of the Carborundum strips located at $x/c = 0.07$ (on both pressure and suction sides of the profile), which create a compression wave particularly visible in the Schlieren image of figure 4.2.

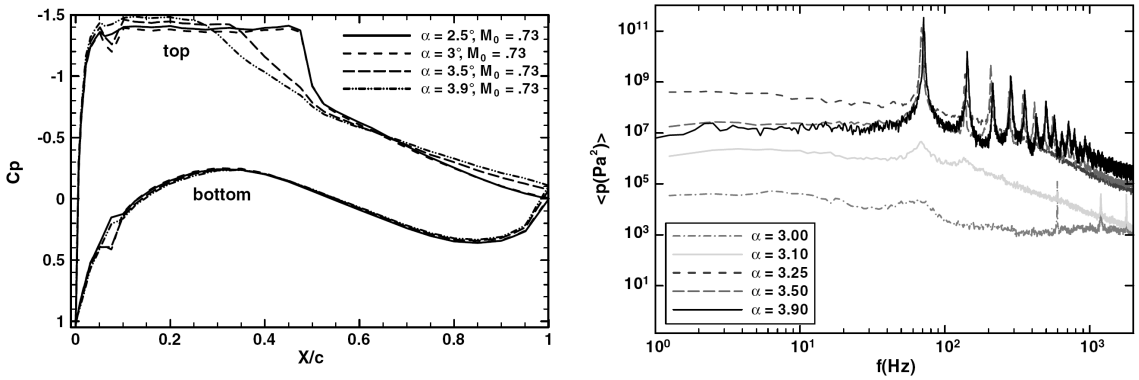

(a) Mean surface pressure coefficient.

(b) Power spectrum of pressure at $x/c = 0.45$.

Figure 4.1: Experimental investigation from Jacquin et al. (2009).

The buffet onset can also be noticed from the power spectra of pressure in figure 4.1b: for $\alpha = 3.0°$ the shock is steady, the signal energy remaining low and distributed among all frequencies. However, a bump can be detected between 40 and 100 Hz, the amplitude of this bump increasing with the angle of attack. For higher values of α, the bump becomes narrower and a peak that corresponds to the buffet frequency ($f = 69$ Hz) is visible from $\alpha = 3.25°$. When increasing the angle of attack, the peak frequency remains at $f = 69$ Hz, indicating that the buffet frequency does not depend on the angle of attack. On the contrary, as shown by other studies (Lee, 2001; McDevitt and Okuno, 1985), the buffet frequency is sensitive to the upstream Mach number. Regardless of the angle of attack, all the spectra are energetic in the medium-frequency range. Unfortunately the experimental studies focused only on the low-frequency unsteadiness, so all the spectra presented by Jacquin et al. (2009) do not give any information about a possible medium-frequency bump in the premultiplied spectra as those observed in other SWBLIs.

Figure 4.2 shows the instantaneous Schlieren images for the two extreme shock positions when the buffet is observed, at $\alpha = 3.5°$. On both images one can recognise the shock wave with the classical lambda pattern, as observed in the channel flow. When the shock is in the most upstream position (figure 4.2a) the separation involves half of the profile, and the recirculation bubble can be recognised by a bright zone

close to the profile under the mixing layer (darker zone that starts at the shock foot). When the shock is in the most downstream position (figure 4.2b) the separation is smaller, and the shock is better captured by the Schlieren image because of less three-dimensional effects.

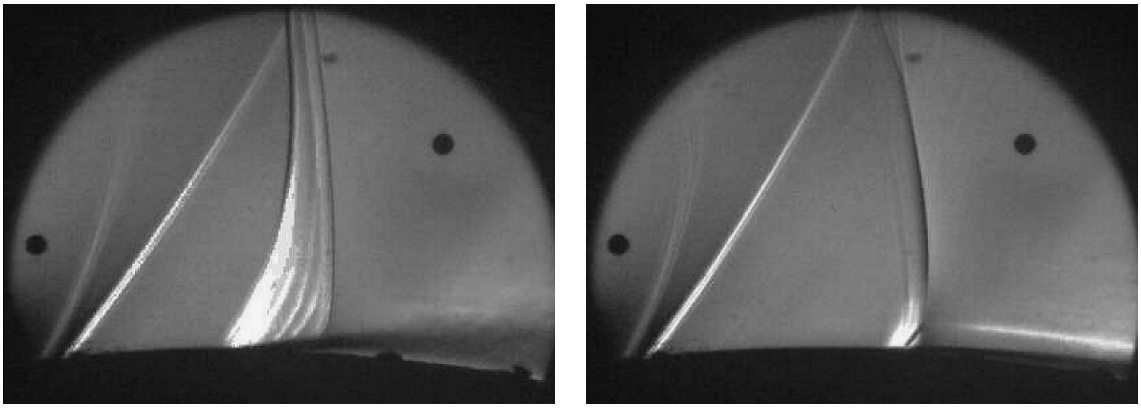

(a) Shock most upstream location. (b) Shock most downstream location.

Figure 4.2: Instantaneous Schlieren images from Jacquin et al. (2009).

Independent of the shock position, the compression wave caused by the Carborundum strip is always visible on the Schlieren image starting from the profile at $x/c = 0.07$. Slightly upstream, one can recognise in both cases of figure 4.2 a bright curved line: as it will be shown in next sections, this is a left characteristic line, that has a central role in the stability of the flow.

4.2 Numerical simulation

The numerical simulations were performed using the same approach as for the channel-flow configuration, described in section 3.1: RANS equations are solved using elsA v3.3 code (Cambier et al., 2012). The Spalart-Allmaras turbulence model (Spalart and Allmaras, 1992) has been used to provide closure for the averaged Reynolds stresses. Second-order AUSM+(P) upwind scheme and a first-order Roe scheme with Harten's correction are used for the mean and turbulent convective fluxes, respectively. A second-order central difference scheme is used for the diffusive fluxes.

A first-order backward-Euler scheme with local time-stepping yields steady-state solutions, whilst unsteady computations are performed using second-order Gear's formulation with a physical time step fixed at $T_{st} = 5 \cdot 10^{-7}$. This yields a maximum CFL numbers of about 13 in the boundary layer upstream the shock, 26 in the wake, and less than 1 in most of the domain.

Computational grids

Numerical simulations and stability analyses are performed on the same two dimensional structured grid, a C-type mesh where far-field conditions are imposed 50 chords away from the profile. The reference grid is composed of 70000 cells: 120 nodes in the direction normal to the profile, 90 nodes in the wake and 210 nodes on each side of the profile. The first mesh point in the boundary layer is below $y^+ = 0.9$ near the interaction. Two additional grids are considered for the mesh convergence, where the grid refinement has been changed in the shock region, in a similar way as done for the channel-flow configuration in section 3.1.2. Considering the chord length c as a characteristic dimension, the grid definition in the shock region is $\Delta_x/c = 0.003$ for the reference mesh, $\Delta_x/c = 0.002$ and $\Delta_x/c = 0.001$ for the convergence study.

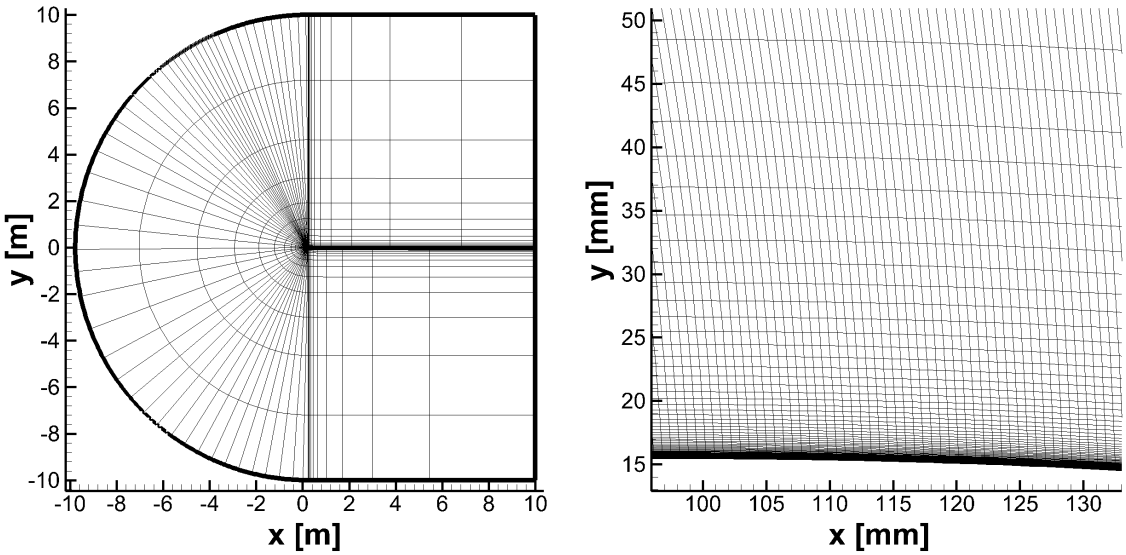

(a) Whole domain, showing 1 point out of 8 along the profile and 1 point out of 4 in the direction perpendicular to it.

(b) Zoom in the shock region, showing all the grid points around $x/c = 0.5$.

Figure 4.3: Reference mesh used for the numerical simulation and stability analysis.

Figure 4.3 shows the whole domain used in the numerical investigation: on figure 4.3a one can see the whole domain, where only one point out of 8 is represented in along the profile and 1 point out of 4 in the direction perpendicular to it for the reference mesh. The shock region is refined using a constant grid refinement in the stream-wise direction: figure 4.3b presents a zoom in the vicinity of the shock, showing all the grid cells. Similarly to the channel-flow configuration, the effect of the grid refinement impacts the shock thickness, but not the shock location.

Boundary conditions

The simulations mimic the wind-tunnel testing conditions described in section 4.1, with boundary conditions that match the experimental situation: the far-field pressure is 101325 Pa, the total temperature is 300 K and the Mach number is $M = 0.73$. The boundary layer on the profile is fully turbulent with a Reynolds number $Re_c = 3.2 \times 10^6$ based on the chord length. No transition term is imposed on the profile, that is considered as an adiabatic wall.

A set of 10 simulations is performed imposing different angles of attack, spanning from $\alpha = 2.5°$ up to $\alpha = 7.0°$ every $\Delta_\alpha = 0.25°$. The maximal Mach number (occurring before the shock) associated to the lower and upper values of α correspond to $M = 1.35$ and $M = 1.50$. This is done always on the same mesh by changing the velocity vector components in the far-field condition, given by $u = U_{ref} \cos\alpha$ and $v = U_{ref} \sin\alpha$, where u and v are the velocity components and $U_{ref} = 240$ m/s is the reference velocity modulus.

RANS results

By solving RANS equations using a local time step, the computation converges to a steady solution. Figure 4.4 presents the horizontal velocity field and the turbulent-viscosity ratio for the particular case of $\alpha = 3.5°$: the flow presents some similarities with the RANS solution obtained in the channel-flow configuration discussed in section 3.1.

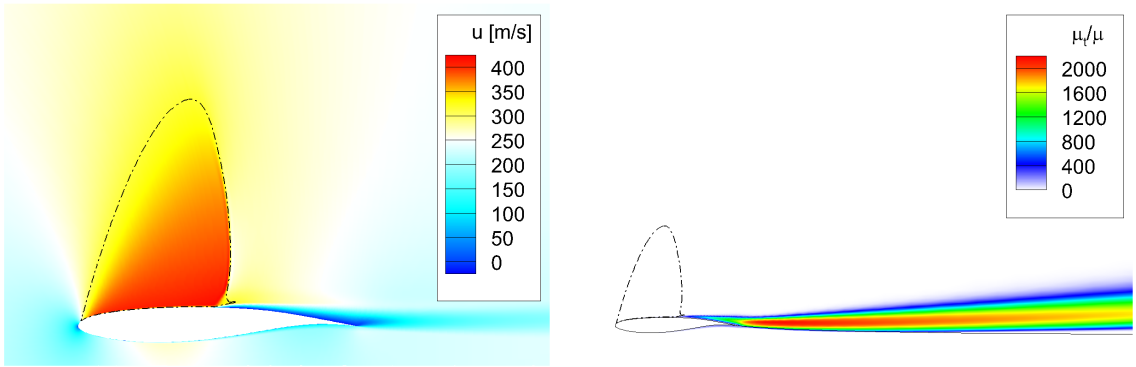

(a) Horizontal velocity field.

(b) Turbulent eddy-viscosity ratio.

Figure 4.4: RANS solution at $\alpha = 3.5°$ (buffet onset condition).

By comparing figure 4.4a with image 3.1a one can notice that on both cases the separation starts at the shock foot, and the recirculation bubble modifies the shock shape into a lambda pattern. However, in the channel-flow configuration the lambda is more accentuated due to the higher curvature of the bump with respect

to the profile. Contrary to the channel-flow configuration, where the end of the recirculation bubble is free to move in the stream-wise direction, the reattachment point is fixed by the end of the profile, and thus does not vary with the angle of attack. However, when the angle of attack is very high, the flow can never reattach. By comparing figure 4.4b with figure 3.1b one can also notice that the turbulent-viscosity ratio has similar values above the recirculation bubble (that is around $\mu_t/\mu \approx 1200$), but then in the profile configuration we can observe an increase in turbulent viscosity after the trailing edge. This feature could be introduced by the Spalart-Allmaras model, where the destruction term depends on the distance from the wall.

Figure 4.5a shows the distribution of the pressure coefficient along the profile for various angles of attack: within the limits of RANS computation, the results recover the experimental measurements of Jacquin et al. (2009) presented in section 4.1. As in figure 4.1a, the distribution of the wall pressure coefficient C_p around the profile is characterised by a pressure plateau before the shock. On the pressure side of the profile, the C_p does not present a strong dependency on the incidence.

The effect of the angle of attack is to decrease the pressure on the suction side of the profile (figure 4.5a presents -C_p), and move upstream the shock: a configuration with a high angle of attack will be characterised by a stronger shock that causes a greater recirculation bubble. Figure 4.6 presents a comparison between two RANS solutions obtained with the lower and higher angles of attack considered in this study.

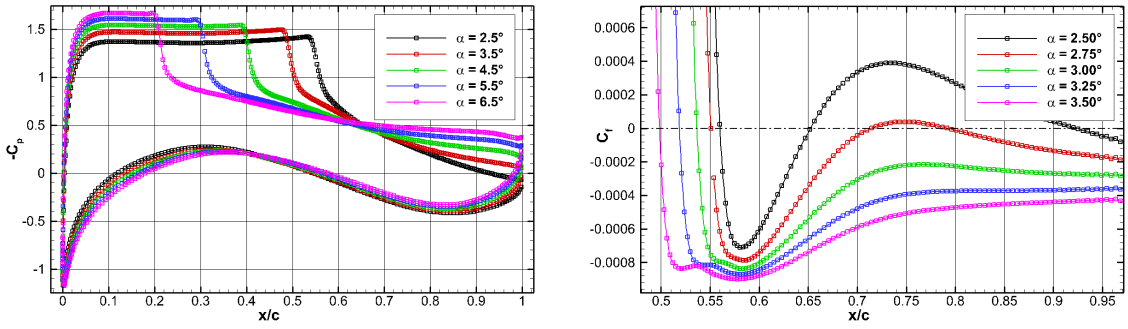

(a) Pressure coefficient.

(b) Skin-friction distribution.

Figure 4.5: Pressure and skin-friction distribution for different angles of attack.

The displacement of the separation point as α increases can be observed also in figure 4.5b, that presents the steady-state distribution of skin-friction coefficient for small angles of attack, up to $\alpha = 3.5°$.

Two separated zones are visible for $\alpha = 2.5°$ and $\alpha = 2.75°$: one at the shock foot and one at the trailing edge. For $\alpha = 3.0°$, the recirculation zone extends from the

shock foot to the end of the profile. In this case, as will be shown below, the unsteady RANS simulation still converges to a steady-state solution. This behaviour is not in agreement with the idea that buffet onset occurs once the separation bubble extends from the shock to the trailing edge, as proposed by Pearcey and Holder (1962). As previously stated by Crouch et al. (2009), the results do not show a clear link between buffet onset and the qualitative features of the flow separation.

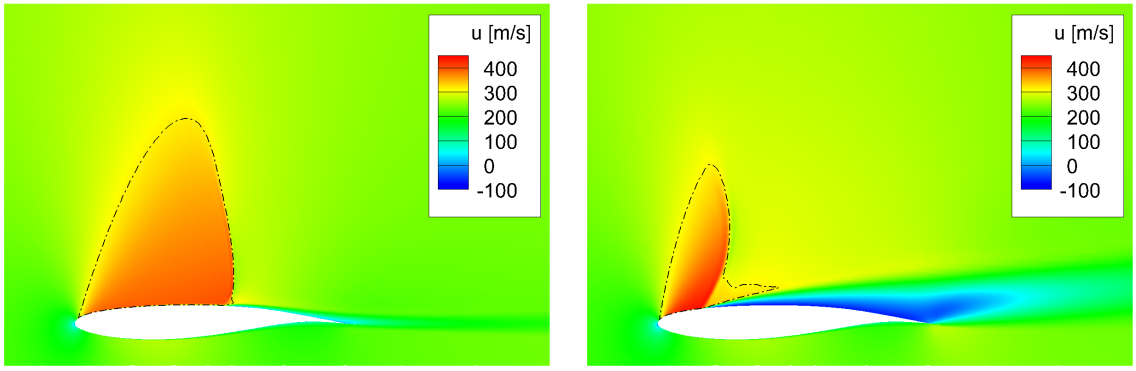

(a) Horizontal velocity, $\alpha = 2.5°$.

(b) Horizontal velocity, $\alpha = 7.0°$.

Figure 4.6: RANS solution at different angles of attack.

The configuration with angles of attack greater than $\alpha = 4.5°$, as the one presented in figure 4.6b, are not commonly investigated because of their limited industrial interest. However, as it will be shown in next sections, those configurations are interesting when considered from a stability-analysis point of view.

URANS results

URANS computations are initialised using the RANS solution obtained when the residuals attains the same value, fixed to 10^{-3}. When the angle of attack is small, temporal integration of RANS equations yields a steady solution, and as for the channel-flow configuration no unsteady phenomena can be observed in the interaction. Increasing the angle of attack, URANS simulations indicate an unsteady behaviour: for $\alpha \geq 3.5°$, the shock begins to oscillate back and forth with periodic motions.

Figure 4.7a presents the time evolution of the pressure coefficient for the buffet-onset configuration: the frequency of the unsteady phenomenon is around 77 Hz when the angle of attack is lower than 4.5°, and slightly increases up to 80 Hz for even higher values of α. The growth rates of the different configurations indicates that the less unstable configuration is obtained for $\alpha = 3.5°$ (note that the scale changes between figure 4.7a and 4.7b.

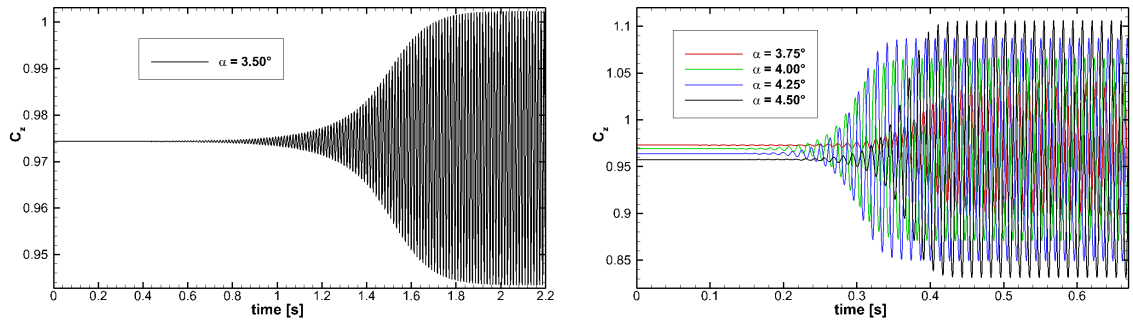

(a) Buffet onset condition ($\alpha = 3.5°$). (b) Evolution of pressure coefficient.

Figure 4.7: URANS solution at different angles of attack.

The amplitude of the shock oscillations increases as the angle of attack is increased, while the mean value of the lift coefficient, that coincides with the value obtained solving the RANS equations, decreases. The numerical simulations indicate that up to $\alpha = 6.0°$ the flow is unsteady: a further increment of the angle of attack corresponds to a steady solution, suggesting a return to a stable configuration. This phenomenon, known as buffet offset, has been observed in other studies (McDevitt and Okuno, 1985) but to the authors knowledge never documented for the OAT15A profile.

As it will be shown in section 4.3, the URANS simulations are in good agreement with the stability analysis. On the contrary, the critical angle of attack that defines the buffet onset found in this study (that is $\alpha = 3.5°$) is not exactly the same as in previous analysis. In the case of Jacquin et al. (2005) described in section 4.1 the threshold value was $\alpha = 3.25°$, whilst in the numerical reproduction of the same configuration performed by Deck (2005) by means of URANS equations the onset appears at $\alpha = 4.0°$. However, the value found in the present study is in agreement with the numerical investigation performed by Deck (2005) by means of zonal DES.

The discrepancy between these values could be due to the turbulent transition of the boundary layer, fixed by a Carborundum strip in the experimental case or numerically imposed in the case of Brunet (2003) and Deck (2005). However, as reported in other configurations (Thiery and Coustols, 2006; Huang et al., 2012), it is known that numerical simulations need a higher angle of attack to reproduce the buffet phenomenon.

4.3 Global-mode decomposition

As done in section 3.2 for the channel-flow configuration, we now consider a global stability analysis and perform an eigenvalue decomposition of the Jacobian matrix.

Both numerical and stability results show a fair grid convergence (square symbols in figure 4.8), so all the results discussed hereafter for the buffet problem are referred to the coarser mesh, presented in figure 4.3.

The linearisation that yields the matrix $\mathbf{J}$ is performed as described in section 3.2.2: for each angle of attack we obtain a base flow $\mathbf{u_0}$, that is a fixed-point of RANS equations satisfying $\mathcal{R}(\mathbf{u_0}) = \mathbf{0}$. As shown in the previous section, a steady solution can always be found. Note that the shock smoothing proposed by Crouch et al. (2007) was not required here since the linearised equations were obtained by a "discretise-then-linearise" approach rather than a "linearise-then-discretise" approach.

The adjoint problem

A Jacobian matrix $\mathbf{J}$ is thus obtained for each angle of attack that was considered. Additionally, in this chapter we also consider the adjoint problem: we define the adjoint Jacobian matrix $\mathbf{J}^\dagger$ such that, for any arbitrary vectors $\mathbf{u}$ and $\mathbf{v}$ we have:

$$\langle \mathbf{u}, \mathbf{J}\mathbf{v} \rangle = \langle \mathbf{J}^\dagger \mathbf{u}, \mathbf{v} \rangle \tag{4.1}$$

The scalar product $\mathbf{Q}$ is the same as in equation (3.25), defined by (3.29). The Jacobian matrix is non-normal if $\mathbf{J}\mathbf{J}^\dagger \neq \mathbf{J}^\dagger\mathbf{J}$, and the spectrum of $\mathbf{J}^\dagger$ is equal to the conjugate of the spectrum of $\mathbf{J}$. The solutions of the adjoint eigen-problem $\tilde{\mathbf{w}}$ are given by:

$$\mathbf{J}^\dagger \tilde{\mathbf{w}} = \lambda^* \tilde{\mathbf{w}} \tag{4.2}$$

where the quantity $\tilde{\mathbf{w}}$ is called the *adjoint global mode*, associated to the direct global mode $\hat{\mathbf{w}}$ (Sipp et al., 2010). If the global modes are non-normal, the convective non-normality results in a different localisation of the direct and adjoint global modes (Marquet et al., 2009).

The direct and adjoint problems can give an insight on where to put actuators to suppress the unsteadiness: passive control, to be most efficient, should be placed at location where direct and adjoint global modes overlap, whereas active control, by for example blowing and suction at the wall, should be placed where the adjoint global mode is maximum (Mettot et al., 2013). Moreover, the adjoint mode propagates upstream while the direct mode propagates downstream, which comes from the opposite sign of the transport equations in the direct and adjoint problems (Chomaz, 2005).

Results

The eigenvalue decomposition gives access to the spectrum presented in figure 4.8. All the stable eigenvalues are roughly independent from the configuration, except

one in the frequency range of the buffet phenomenon: a dash-dot line in figure 4.8 indicates the path that this eigenvalue takes while increasing the angle of attack. The flow is stable for small angles of attack, up to $\alpha = 3.25°$. Then, the least stable eigenvalue crosses the real axis between $\alpha = 3.25°$ and $\alpha = 3.5°$: the onset of instability is due to a Hopf bifurcation, as observed by Crouch et al. (2007), and the critical angle of attack that determines the offset of the buffet phenomenon is $\alpha = 3.5°$. A further increase in the angle of attack results in an increase in the instability growth rate, up to $\alpha = 4.0°$. Then, the growth rate begins to decrease and we can observe buffet offset after $\alpha = 6.0°$. To the authors knowledge this "return to stability" behaviour has never been documented in literature.

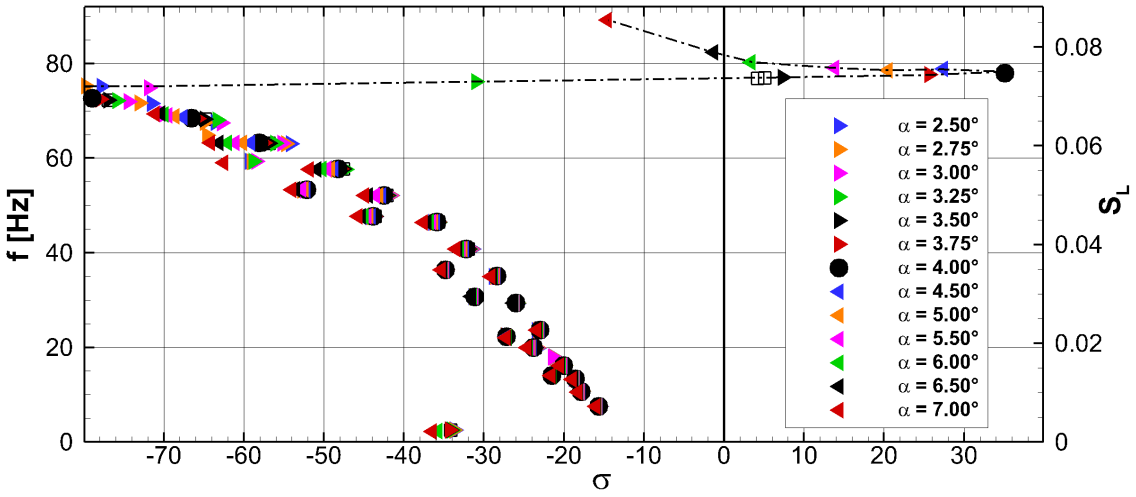

Figure 4.8: Stability analysis spectrum for the buffet configuration.

The physical frequency of the buffet phenomenon resulting from the eigenvalue decomposition at $\alpha = 3.5°$ is 77 Hz, satisfyingly close to the experimental value of 69 Hz found by Jacquin et al. (2009) in the same configuration. It is worth saying that a value of 77 Hz was found in the experimental investigation in the configuration where $M = 0.74$ instead of $M = 0.73$ like in this study. After the onset, the buffet frequency remains constant up to the most unstable configuration, and then increases up to 80 Hz for $\alpha = 6.0°$: the "return to stability" phenomenon is accompanied by an increase of the shock-buffet frequency. The angle of attack that defines the thresholds of buffet onset and offset, as well as the frequency of the unstable modes, compares favourably with the numerical results obtained with the URANS simulation presented in section 4.2.

When using frozen viscosity linearisation, no unstable modes are found. Crouch et al. (2009) documented the same behaviour, indicating that, as for the channel-flow configuration, the eddy-viscosity term presents a central role in the linearised dynamic. When considering different meshes, a small shift in the real part of an

eigenvalue is observed: in figure 4.8 the square points show the mesh dependency indicating the position of the first unstable eigenvalue, obtained when $\alpha = 3.5°$ for the others grids.

Figure 4.9 presents the spatial structure of the unstable global mode at $\alpha = 4.0°$ corresponding to the most unstable configuration. The mode structure is the most energetic in the shock for all the conservative variables, but a non negligible contribution is located in the mixing layer. In the stream-wise momentum components the mode is present also in the recirculation bubble, but we observe an opposite sign between the shock and the separated zone: this suggests that shock oscillations and bubble expansions are in phase opposition, similarly to what has experimentally been observed for the low frequency motions in the channel-flow configuration of chapter 2.

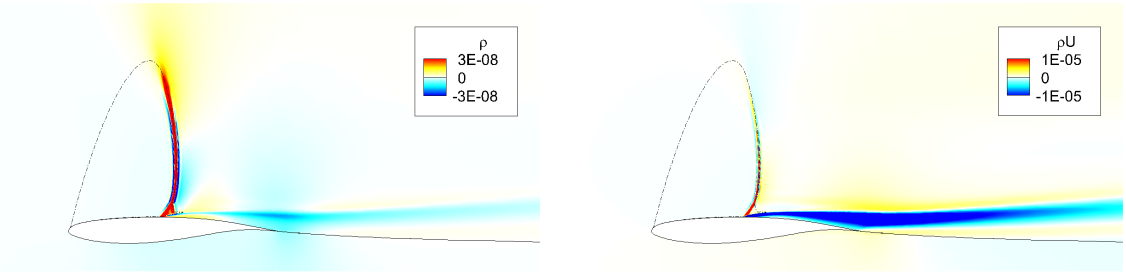

(a) ρ component.

(b) ρU component.

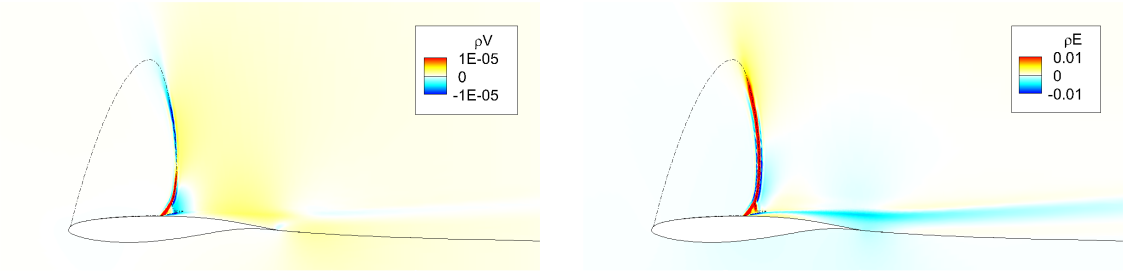

(c) ρV component.

(d) ρE component.

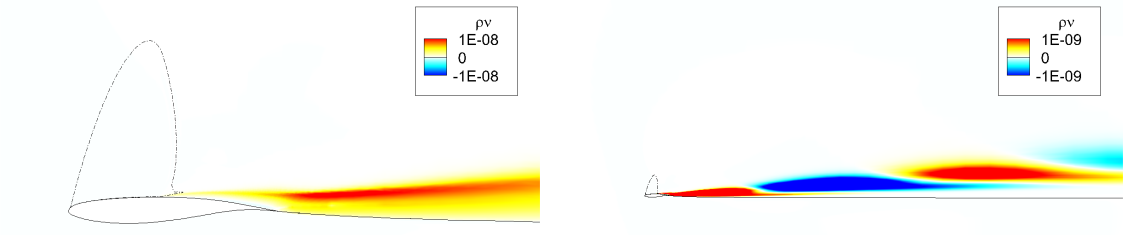

(e) $\rho\tilde{\nu}$ component.

(f) $\rho\tilde{\nu}$ component, domain.

Figure 4.9: Direct buffet mode for $\alpha = 4.0°$. Real part of different components.

If we look at the turbulence component in figure 4.9 we can notice that the

buffet phenomenon is associated to large scale fluctuation of the eddy-viscosity, that propagates in the wake. This feature is not linked to the Kelvin-Helmholtz type instability but is more likely the fluctuation of turbulence viscosity due to contraction and expansion of the recirculation bubble, caused by the shock displacement.

The adjoint problem of equation (4.2) yields the adjoint mode, that is depicted in figure 4.10 for the configuration with $\alpha = 4.0^\circ$ (corresponding to the most unstable configuration). The adjoint mode indicates the regions on the flow where we have maximum receptivity to momentum forcing and mass injection (Marquet et al., 2008b). In this configuration, those zones are localised in the boundary layer both upstream and downstream the interaction, mostly on the suction side. The adjoint mode in the supersonic flow has a triangular shape, whose edges follow the boundary layer, the upwind part of the sonic line, and an oblique line impinging the profile exactly where the boundary layer separates.

Figure 4.10a shows the superposition of the adjoint mode with the characteristic lines (obtained with equation (3.3.3)). The oblique part of the adjoint mode follows exactly the right characteristic line that impacts on the shock foot, where the recirculation bubble begins. This feature can be interpreted as follows: the separation point has a fundamental importance in the dynamic of the flow, and a modification of its position can influence the whole dynamics. The adjoint mode indicates the zone where the flow presents high receptivity to external forcing. As in supersonic flows information travels along characteristic lines, only the supersonic zone that is connected to the separation point trough a characteristic line can influence the separation point. A similar behaviour was observed in the channel-flow configuration when discussing the optimal forcing that induces low-frequency motions (section 3.3).

If we consider now the characteristic lines associated to the positive sign of equation (3.3.3), called the left characteristic, we can see that the adjoint mode follows those lines only in the upwind part of the supersonic zone and with very low energy. Then, these left characteristic lines reflect on the sonic line and propagate along the right characteristic that hit the separation point. This difference in the energy suggests that pressure disturbances that propagate along Mach waves from the profile to the sonic line have less impact on the buffet phenomenon than velocity disturbances that travel along characteristic lines and impact directly on the separation point. Although less energetic in the adjoint mode, this characteristic line has a central role in the buffet phenomenon as its presence can be seen also from the Schlieren image in figure 4.2.

Recently Agostini et al. (2012) have performed LES computations of a shock reflection on a turbulent boundary layer at Mach number $M = 2.3$. Using two-

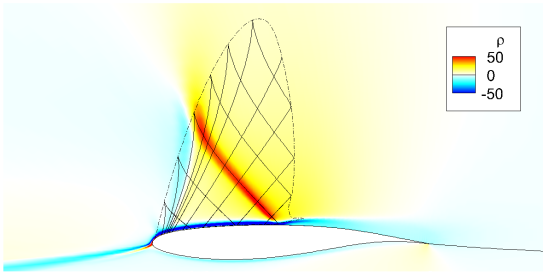

(a) ρ component.

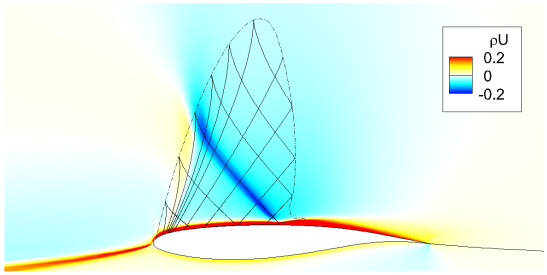

(b) ρU component.

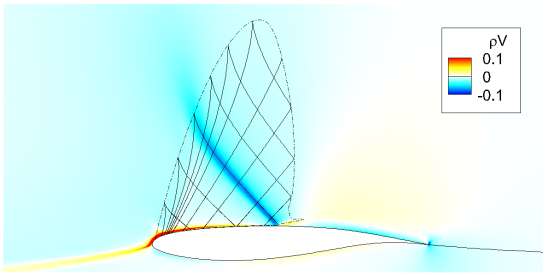

(c) ρV component.

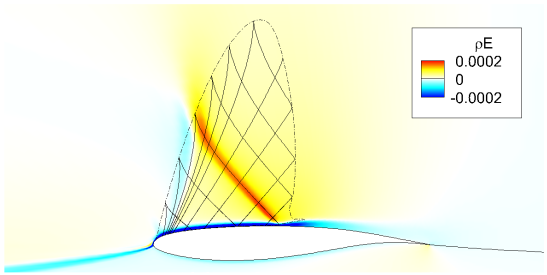

(d) ρE component.

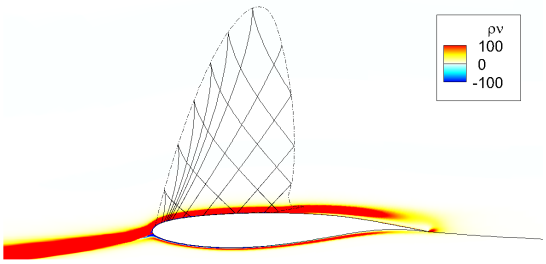

(e) $\rho\tilde{\nu}$ component.

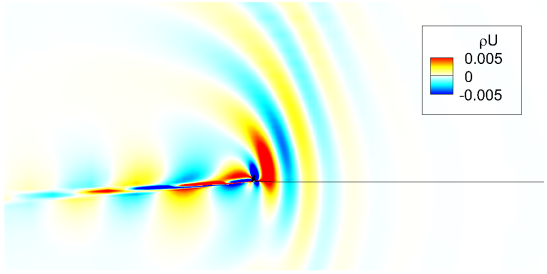

(f) ρU component, domain.

Figure 4.10: Spatial structure of the adjoint buffet mode for $\alpha = 4.0°$. Superposition of the sonic (dash-dotted) and characteristic (solid) lines.

point correlations they showed how some vortical structures in the mixing layer generate pressure fluctuations that propagate along the characteristic lines of the expansion fan. A similar analysis is not possible here (and neither in the channel-flow configuration) because of the transonic nature of the flow: after the shock wave the flow becomes subsonic, and the characteristic lines do not exist anymore.

In figure 4.10f we can also observe the adjoint mode spatial structure far away from the profile: the adjoint mode is located in the part of the incoming flow that will become the boundary layer around the profile, showing that variations of the incoming flow have a strong impact on the dynamics of the interaction. Acoustic effects due to the compressible nature of the equations are also visible: some acoustic waves come from downstream of the profile and propagate upwind towards the interaction.

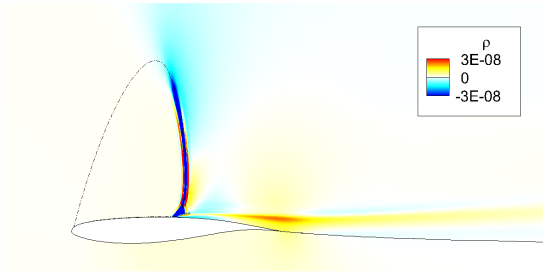

(a) Direct mode, $\alpha = 3.5°$.

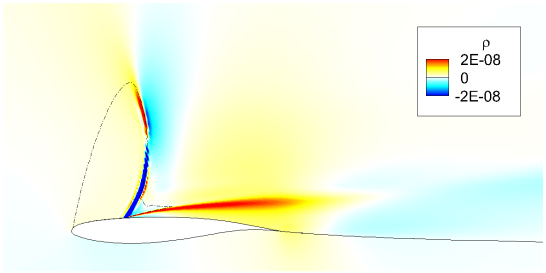

(b) Direct mode, $\alpha = 6.0°$.

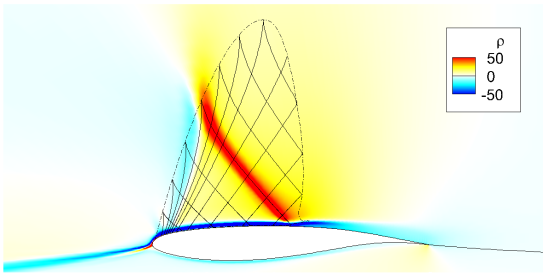

(c) Adjoint mode, $\alpha = 3.5°$.

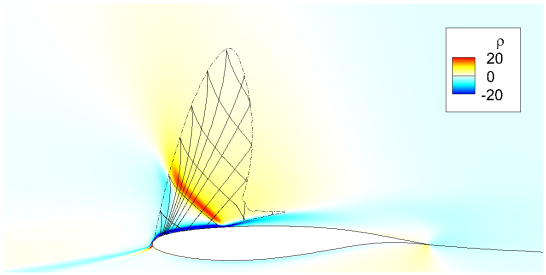

(d) Adjoint mode, $\alpha = 6.0°$.

Figure 4.11: Unstable global modes. Real part of density component.

Figure 4.11 shows the direct and adjoint global modes for the configurations that correspond to buffet onset and offset. Even if the base flow presents some differences in terms of shock position, separation point location and size of the recirculation bubble, one can notice some similar aspects that are present in each unstable configuration: the unstable global mode is always predominantly located on the shock wave, independently from the angle of attack. When considering configurations with a stronger interaction, the only difference between the different cases is the shock position and the size of the recirculation bubble.

Concerning the adjoint modes, figures 4.10 and 4.11 also indicate that the adjoint variables are continuous with zero gradient at the shock. This feature has been demonstrated in quasi-one-dimensional Euler equations by Giles and Pierce (1997), using a theoretical approach that relies on the derivation of a closed form solution to the adjoint equations. In the same paper, it is shown how a change in sign in either of the hyperbolic characteristic is responsible for a $\log(x)$ singularity at the sonic point. However, for two-dimensional configurations as the case of the current study, it is argued that there is no longer a singularity at a sonic line, as confirmed in the present case. This has been explained by considering the region of influence of points in the neighbourhood of the sonic line by Giles and Pierce (2001).

4.4 Global-Resolvent analysis

The numerical simulations of section 4.2 and the global-mode decomposition of section 4.3 indicate that the flow presents self-sustained oscillations when the angle of attack is between $\alpha = 3.5°$ and $\alpha = 6.0°$. In those cases the dynamic of the flow is dominated by the unstable global mode. However, that does not mean that the buffet unsteadiness is the only one present: the flow may still behave as a noise amplifier and a frequency-selection process such as that described in the channel-flow configuration may still be possible, regardless of the angle of attack.

In this section we apply the theoretical approach introduced in section 3.3.2 to the transonic flow over the OAT15A profile. From a mathematical point of view, the global Resolvent is defined when the determinant of $(i\omega\mathbf{I} - \mathbf{J})$ is different from zero. This condition is assured, for a given frequency ω, as long as there is no eigenvalue of the Jacobian matrix $\mathbf{J}$ with real part equal to zero, and imaginary part equal to ω. In this case, the leading singular value of the global Resolvent, and thus the gain function, tends to infinity.

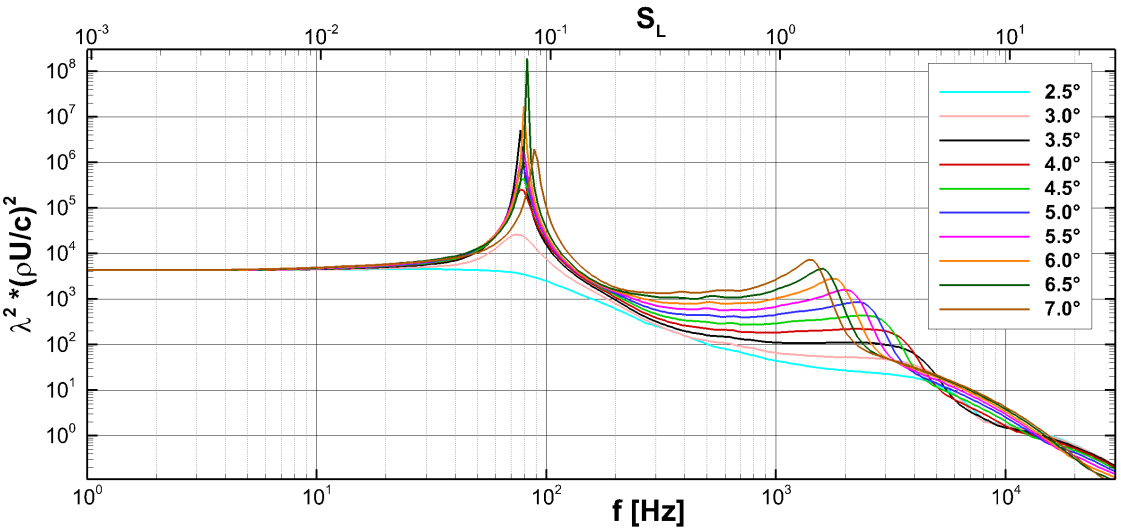

Figure 4.12: Gain function for different angles of attack.

The gain functions in figure 4.12 confirm this behaviour: considering the low-frequency range, the curves present the highest peaks when $\alpha = 3.5°$ and $\alpha = 6.0°$: in this configuration the buffet mode is the closest to the imaginary axis. The peaks that correspond to the most energetic gains are located at the frequencies which match those of the neutral eigenvalues. Considering the configurations displaying an unstable global mode, after $\alpha = 4.0°$ there is a slight rise in the buffet frequency, and the buffet offset is accompanied by a decrease in the oscillations period. This behaviour was already observed in the spectrum of figure 4.8. Since the profile is in the free-stream, acoustic resonances such as those observed in the channel flow are

not present. The gain function still presents a low-pass filter behaviour: regardless of the angle of attack, the very first part of the gain function is a straight horizontal line, as in the channel-flow configuration.

Considering low-frequency motions, even if the singular-value decomposition of the global Resolvent can be performed, there is no interest to compute the optimal forcing and associated response of the flow at a frequency where we have an unstable eigenvalue: in this case, the dynamic of the flow is dominated by the global mode, and no convective instabilities can in principle arise. For this reason we will discuss low-frequency motions only for the configurations where no unstable global modes are found.

Figure 4.13 presents the optimal forcing at $f = 80$ Hz and the associated response for two angles of attack: $\alpha = 2.5°$, before the buffet onset, and $\alpha = 7.0°$, after the buffet offset. One can notice a strong similarity between the optimal forcing at $\alpha = 2.5°$ and the unstable adjoint global mode at the buffet onset (figure 4.11c). Likewise, the optimal forcing at $\alpha = 7.0°$ has a space distribution similar to the adjoint unstable global mode of figure 4.11d, obtained for $\alpha = 6.0°$: despite the difference on the size of the recirculation bubble, the optimal forcing is always located in the boundary layer on the suction side, and on the supersonic zone along an oblique line that impinges on the shock foot. As for the adjoint global mode and the optimal forcing in the channel-flow configuration, the spatial structure in the supersonic zone is located along the right characteristic line that ends at the separation point. Close to the leading edge, the most upwind part of the forcing follows the left characteristic line.

Although in a different configuration, both optimal responses of the OAT15A profile present the same spatial structure as in the channel flow, yielding the same conclusion as in the previous section concerning the shock wave: if the flow is excited with some form of low-frequency forcing, the response will be on the shock, with the highest value close to the shock foot. Regarding the behaviour of the separated zone, the spatial structure of the response seems to depend on the angle of attack: if the height of the recirculation bubble is small compared to its length, that is the case for $\alpha = 2.5°$, the optimal response is energetic in both the mixing layer as well as inside the separated area. Note that, as indicated in figure 4.5b, in the $\alpha = 2.5°$ configuration the trailing edge separation and the shock induced separation are divided by a re-attached zone. When increasing the angle of attack, as for example when $\alpha = 7.0°$, the shock-induced separation merges with the separated zone at the trailing edge: the lambda shape of the shock is strengthened, and the separated zone is comparable in size to the channel-flow configuration. In this case, the optimal response after the shock is located only in the mixing layer above the recirculation

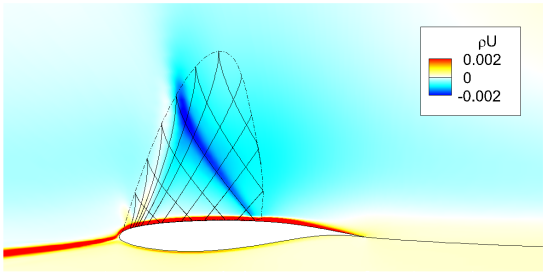

(a) Forcing, $\alpha = 2.5°$.

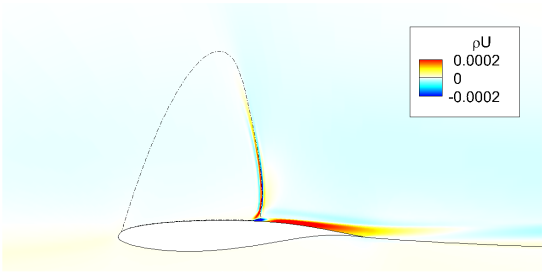

(b) Response, $\alpha = 2.5°$.

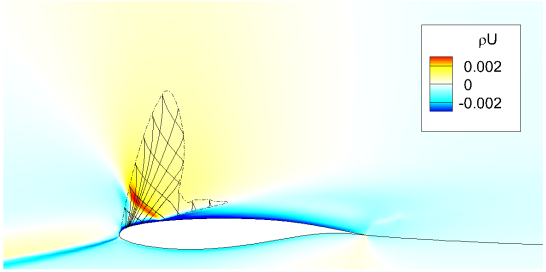

(c) Forcing, $\alpha = 7.0°$.

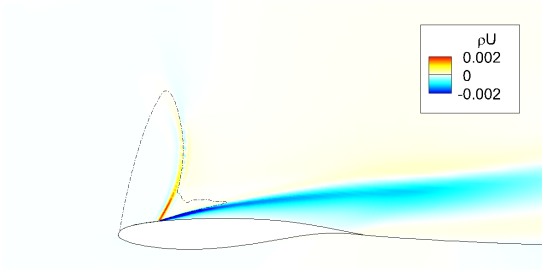

(d) Response, $\alpha = 7.0°$.

Figure 4.13: Optimal forcing and response for low-frequency unsteadiness ($f = 80$ Hz): before the buffet onset ($\alpha = 2.5°$) and after the offset ($\alpha = 7.0°$).

bubble, and not inside it as in the previously discussed case.

Despite this small detail on the spatial form of the optimal response, the singular-value decomposition of the global Resolvent indicates that low-frequency unsteadiness is mostly located in the shock wave, and associated to the so-called breathing of the mixing layer.

Considering again the optimal gains in figure 4.12, we can notice a rise in the medium-frequency range for all the angles of attack. As for the channel-flow configuration, the eigenvalue decomposition of section 4.3 did not indicate any unstable mode in the equivalent zone of the spectrum. The gain function for $\alpha = 2.5°$ presents the same bump as in the channel flow, so it is necessary to consider the premultiplied gain to see a peak in medium-frequency range. Increasing the angle of attack the premultiplied scale is not needed and an energetic bump can always be observed for higher α. As previously stated, the global Resolvent singular values tends to infinity as the real part of a Jacobian eigenvalue tends to zero. The fact that the medium-frequency bump becomes narrower as increasing the angle of attack may be linked to a global instability that could arise for higher α.

Figure 4.14 presents the optimal forcing for the peak frequency in the premultiplied gain function of four different configurations. Those frequencies are $f = 4000$ Hz for $\alpha = 2.5°$, $f = 3000$ Hz for $\alpha = 4.0°$, $f = 2000$ Hz for $\alpha = 5.5°$, and $f = 1400$ Hz for $\alpha = 7.0°$. The optimal forcing is located in the boundary layer (on the whole

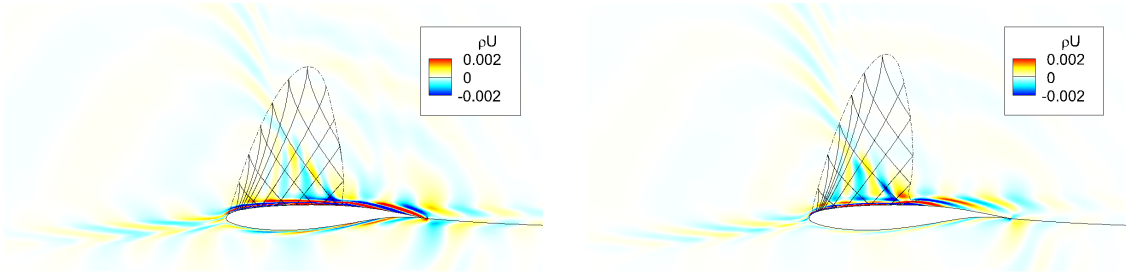

(a) $\alpha = 2.5°$, $f = 4000$ Hz.

(b) $\alpha = 4.0°$, $f = 3000$ Hz.

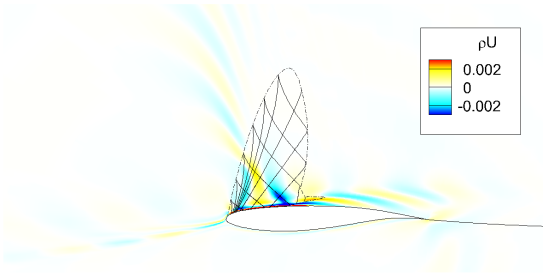

(c) $\alpha = 5.5°$, $f = 2000$ Hz.

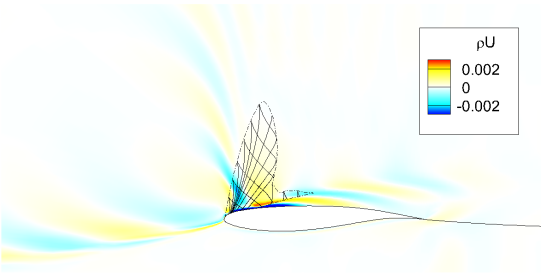

(d) $\alpha = 7.0°$, $f = 1400$ Hz.

Figure 4.14: Optimal forcing for medium-frequency unsteadiness.

suction side for low angles of attack, before the interaction for higher α), with a maximum value at the shock foot. In the supersonic zone, the forcing does not exactly follow the right characteristic line that ends at the separation point, but has a small-scale structure similar to the one observed in section 3.3.

The optimal responses associated to those medium-frequency forcing is presented in figure 4.15: it indicates that Kelvin-Helmholtz instabilities are still present in this configuration, regardless of the angle of attack. Contrarily to the channel flow case, two zones of the flow are affected by this medium-frequency motion: the mixing layer caused by the separated region and the mixing layer after the trailing edge. This last instability was not present in the channel-flow configuration because of the boundary walls, and may explain why the gain is higher in this configuration: a medium-frequency forcing can trigger at the same time Kelvin-Helmholtz type instability on two different zones of the flow.

Comparing the Kelvin-Helmholtz type response in figure 4.15 one can notice that the responses become more present as increasing the angle of attack, and the contribution of the separated zone is roughly the same as the contribution due to the trailing edge: the peak in the gain function indicates that medium-frequency instabilities are the most energetic for the frequency that can trigger at the same time both unsteadiness on the profile.

The evolution of the gain function in figure 4.12 indicates that the Kelvin-Helmholtz instability frequency becomes smaller when increasing α this behaviour

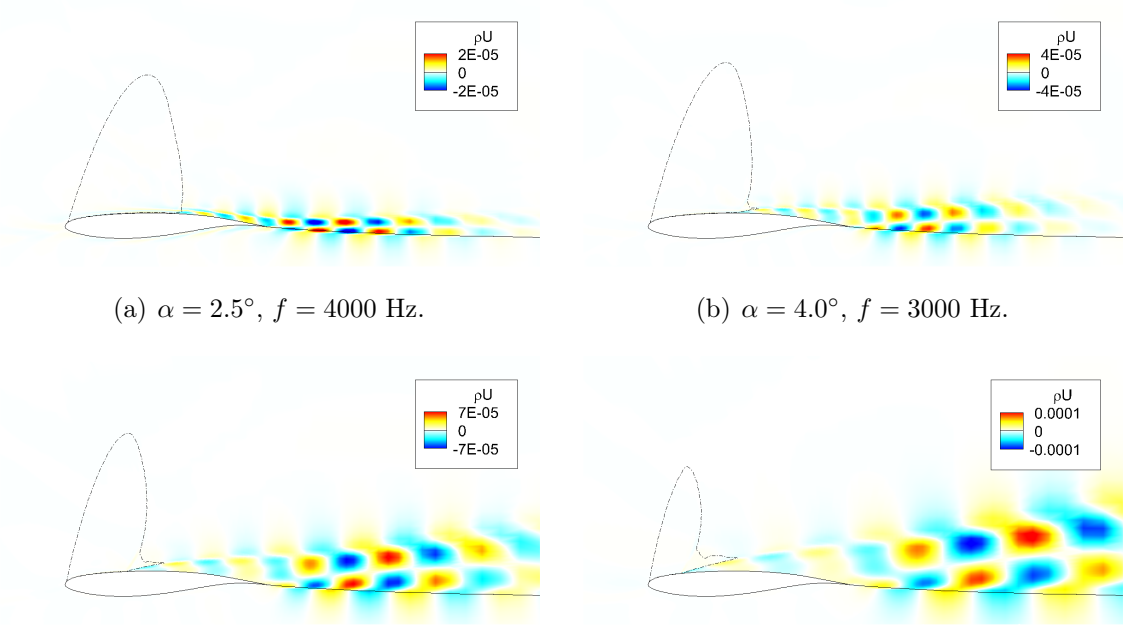

(a) $\alpha = 2.5°$, $f = 4000$ Hz.

(b) $\alpha = 4.0°$, $f = 3000$ Hz.

(c) $\alpha = 5.5°$, $f = 2000$ Hz.

(d) $\alpha = 7.0°$, $f = 1400$ Hz.

Figure 4.15: Optimal response for medium-frequency unsteadiness.

may be due to the fact that this unsteadiness depends on the mixing layer thickness: the higher the angle of attack, the larger the separated zone, and thus the smaller the frequency. However, the medium-frequency unsteadiness is broad band, indicating that in the flow Kelvin-Helmholtz type instabilities are present in the range $1 - 4$ kHz, similarly to the channel-flow configuration.

4.5 Conclusions

This chapter focused on the unsteady dynamics of the transonic interaction between a shock and a boundary layer over an OAT15A profile. The experimental investigation performed by Jacquin et al. (2005) is considered as reference and is used to compare the results.

Two-dimensional numerical simulations can reproduce the oscillatory motions of the shock wave known as the buffet phenomenon: when integrating the equation in time, URANS simulation can predict the unsteady behaviour of the interaction, and both the frequency of the periodic shock motions as well as the critical angle of attack that characterise the buffet onset are in fair agreement with the experimental investigation. Buffet offset is observed when the angle of attack exceeds $\alpha = 6.0°$. The results recover and extend the numerical results obtained in previous studies (Brunet, 2003; Deck, 2005). The mean flow obtained using a local time stepping is

then considered for a stability analysis.

The linearised Navier-Stokes operator is thus again obtained in a discrete framework. Global-mode decomposition indicates that the buffet phenomenon is linked to a global instability of the flow. The angle of attack that defines the threshold of the unsteady shock motions is in agreement with the numerical simulation, and the buffet offset is accompanied by a small rise in the buffet frequency. The direct global mode compares favourably with the stability analysis performed by Crouch et al. (2009), whilst the adjoint global mode, whose spatial distribution follows the characteristic lines in the supersonic region of the flow, can give an insight of where control should be placed to suppress the unsteadiness.

The eigenvalue decomposition of the Jacobian matrix indicates that the shock buffet is the only global instability present in the interaction. However, as observed in the channel flow configuration, convective instabilities can arise when the flow is subject to external forcing. For this reason, a singular-value decomposition of the global Resolvent is performed, and the gain function indicates that the interaction behaves as a noise amplifier: when the flow is stable, optimal forcing indicates that broad-band shock oscillations can be triggered by environmental noise.

Concerning medium-frequency motions, the global-Resolvent analysis indicates that medium-scale unsteadiness can arises from the separated zone. Similar motions have also been observed in the Délery bump, by means of correlation of Schlieren images and linear-stability analysis, and are linked to Kelvin-Helmholtz instability. However, despite the channel-flow configuration, the medium-frequency motions are present both in the mixing-layer above the separated region as well as in the mixing layer at the trailing edge of the profile. This unsteadiness is shown to be broad band and not related to the presence of the shock buffet phenomenon. Moreover, the intensity of the oscillations increase with the interaction strength while the peak frequency decreases as the angle of attack is increased.

Chapter 5

Conclusions

It is well established that SWBLIs are unsteady phenomena, characterised by low-frequency shock motions and medium-frequency unsteadiness linked to the separated zone. The main purpose of this study was twofold: to describe experimentally the unsteady dynamics of the transonic interaction between a strong shock and a turbulent boundary layer developing over the Délery bump, and to address the problem of the unsteadiness in SWBLI using stability analysis.

The experimental investigation presented in chapter 2 gave access to a full characterisation of the considered configuration: the flow has been investigated using PIV measurements, which gave access to the mean features of the interaction. Wall-pressure measurements indicated that the shock is affected by low-frequency unsteadiness, whilst medium-frequency fluctuations are typical of the separation-bubble dynamics, in agreement with other studies. A more global investigation using high-speed Schlieren photography yielded a complete characterisation of the unsteady behaviour of the interaction: medium-frequency fluctuations are located almost exclusively in the mixing-layer generated by the separation point, although low-frequency unsteadiness is found both in the shock region and in the recirculation bubble. The shock foots on both walls seemed to be the most affected by these fluctuations. By computing the Strouhal number, the frequencies of shock and mixing-layer motions compare favourably with other studies: the experimental measurements showed that the particular case of the transonic SWBLI over the Délery bump presents the typical unsteadiness observed in more common interactions.

Numerical simulations provided a base flow, that adequately represented the interaction as observed experimentally. Despite the limitations introduced by the turbulence model, a RANS approach could correctly reproduce the mean behaviour of the interaction, but no information could be deduced concerning the unsteady phenomena. A linear stability analysis has then been proposed: the absence of

unstable global modes indicated that the amplifier dynamics should be described by an optimal perturbation formalism and not by an eigenvalue decomposition as proposed by previous studies: a forcing is always required to maintain unsteadiness.

A theoretical formulation based on a singular-value decomposition of the global Resolvent has then been proposed: it has been shown that the non normality of the linear operator has a great importance in describing the frequency-selection process observed experimentally. The main result of this approach is the confirmation that the low-frequency unsteadiness does not come from a global instability, but is the response of the shock to existing environmental noise: the energy growth observed experimentally is caused by the non normality of the stable linearised Navier-Stokes operator and not by an unstable eigenvalue. Regarding low-frequency motions, the singular-value decomposition of the global Resolvent indicated that the optimal forcing is at the shock foot, but a forcing in the separated zone or in the incoming boundary layer could also trigger the shock unsteadiness. In particular, the optimal forcing that can trigger the largest flow response has been shown to be located along the characteristic line that impacts the shock foot. Considering medium-frequency unsteadiness, the unsteadiness is linked to a Kelvin-Helmholtz type instability, that exists regardless of the presence of the shock wave.

From a broader perspective, it has been shown that SWBLI are amplifier flows: in a global framework, they should be characterised by analysing the singular values and vectors of the flow, and not the eigenvalues of the Jacobian matrix. This approach, conceptually simple because based on a robust and very general concept, yielded a direct link with receptivity studies since the spatial location of the optimal forcing identifies sensitive regions of the flow. The results obtained confirm that the problem of the unsteadiness can be analysed with a linear approach, that the scale decoupling assumption holds, and that a 2D configuration can be a good representation of the experimental cases.

Concerning the separated zone, both the experimental investigation and the stability analysis indicated that low-frequency unsteadiness is responsible for the so called “breathing” of the mixing layer, whilst the recirculation bubble is primarily affected by medium-frequency motions. The behaviour of the shock wave is more complicated: on one side, the wall-unsteadiness investigation indicated that the shock is uniquely affected by low-frequency motions, but the Fourier-mode decomposition has shown that medium-frequency unsteadiness could be present, with a lower energy content, even on the shock wave. This last observation is in agreement with Agostini et al. (2012), and indicates that the shock kinematics is the mirror of the physical phenomena localised in the separated zone. However, the presence of the shock in the medium-frequency Fourier modes could come from some three

dimensional effect captured by the Schlieren investigation, or form the image saturation caused by inappropriate lighting. When considering the stability analysis, the gain function indicated that the shock wave is not prone to medium-frequency motions, exhibits high energy only for low frequency, and filter the high-frequency motions arising from the environment. In conclusion, we believe that, at first order and in a two-dimensional configuration, the shock wave acts like a low-pass filter.

Regarding the source of unsteadiness, the linearised approach does not fully answer the question on the origins of the shock motions. Nevertheless, it has been shown that both perturbations on the incoming flow and on the recirculation bubble are linked to the shock unsteadiness, implying that the source of low-frequency motions may not be unique. This result is an indication that the superstructures existing in the upstream boundary layer (Ganapathisubramani et al., 2009) are not necessary for the low-frequency SWBLI dynamics: as observed by the numerical simulations of Touber and Sandham (2009b), the interaction exhibits low-frequency unsteadiness even without the presence of the turbulent eddies in the incoming flow. We support the idea that interaction responds as a dynamical system that is forced by external or internal disturbances: if forced by an external agent, such as for example the incoming flow, the shock will respond. However, even in the absence of this forcing, low-frequency oscillations can be caused by coupling between the dynamics of the separation bubble and the shock (Dussauge and Piponniau, 2008).

The global modes decomposition of the Jacobian matrix indicated that shock unsteadiness is not an intrinsic property of the global system (Touber and Sandham, 2011) that can be explained by the presence of an unstable global mode (Robinet, 2007; Touber and Sandham, 2009b; Pirozzoli et al., 2010b). These last works can be seen as an extension to the supersonic domain of the existence of stationary global instabilities inside recirculation bubbles, but the stationary global modes can not give any information about unsteadiness of the interaction as it comes from a response to existing disturbances.

The approach applied to the Délery bump configuration has then been used to investigate the similar transonic SWBLI of a flow over the OAT15A profile. The high-amplitude periodic shock motions, when present, can correctly be reproduced by the RANS approach, and the eigenvalue decomposition can predict the low-frequency instability (Crouch et al., 2009). By comparing the results of the stability analysis with the experimental investigation performed in the same configuration, a good agreement on frequencies is found. The many angles of attack considered gave access to a complete description of the interaction for the chosen combination of Mach and Reynolds numbers, shedding new light on the buffet offset. Moreover, it has been shown the spatial form of the adjoint global mode linked to the buffet

phenomenon: the mode is linked to the characteristic lines and indicate the zone of the flow that can be relevant for control purposes.

When focusing on the pseudo-resonance phenomena, the singular-value decomposition indicated that the flow is prone to low-frequency unsteadiness even before the buffet onset. However, besides the periodic shock motions, the most energetic sources of unsteadiness are the mixing layers developing from the separation point and the trailing edge: here medium-frequency motions, linked to Kelvin-Helmholtz type instabilities, are observed. Moreover, the importance of those unsteadiness on the flow increases when increasing the angle of attack.

The flow over the OAT15A profile presented some similarities with the channel-flow configuration: when considering a small angle of attack, in both cases a numerical approach based on RANS simulations failed to predict the shock motions, and the eigenvalue decomposition indicated that the linearised Navier-Stokes operator is stable in a global framework. The unsteadiness has been linked to convective instabilities, and it was shown that the singular-value decomposition of the global Resolvent is capable of describing both low- and medium-frequency motions. However, when increasing the angle of attack the buffet phenomenon appears, and the flow over the OAT15A profile is characterised by the presence of an unstable mode. The shock motions are shown to be periodic, and the unsteady behaviour no longer presented the noise-amplifier dynamics typical of shock-wave/boundary layers interactions.

5.1 Perspectives

Concerning the experimental study, PIV measurements could be used not only to investigate the mean flow, but also to have access to the unsteady motions of the shock. Although 1000 pairs of images are enough to obtain a good description of the interaction, some interesting results could be obtained when applying the cross-correlation technique as for the Schlieren images to PIV results. To do that, at least 5000 images are necessary. Moreover the use of PIV-3C or tomographic PIV could extend the correlation analysis to the span-wise velocity component, and give access to three-dimensional structures that can arise in the interaction. Given the time scales of the unsteady phenomena, PIV-RT may not be adapted to characterise the medium-frequency motions.

The high-speed Schlieren visualisation have shown the potential of the Fourier modes decomposition and correlation technique, but further work is needed: the images quality have to be improved, for example by the use of 16-bit camera sensors that increase the results definition, and image saturation have to be avoided, because

of its strong impact on the Fourier modes decomposition. Moreover, the quality of the results increases when considering longer data samples: a better memory allocation in the image processing could give access to spectra with higher frequency definition. The assumption of the linear relation between light intensity and density gradients have to be discussed in details to obtain a deeper physical meaning of the results. Finally, the shadowgraph technique could be used as an alternative to Schlieren visualisation, to obtain a clearer definition of the medium-scale structures of the mixing layer, without the decomposition in horizontal and vertical density gradients.

Concerning the numerical investigation on the Délery bump configuration, the natural evolution of this work consists in the computation of the sensitivity gradients, that would give access to the zone of the flow where passive control should be placed to suppress the unsteadiness. Moreover, the theoretical method applied on the considered transonic interaction could be used to investigate more common configurations: an interesting application could be the IUSTI shock-reflection case, well documented in literature, where the unsteady behaviour of shock wave and mixing-layer region depends on the shock intensity (Dupont et al., 2006). In particular, a stability analysis could explain if the unsteadiness comes from an unstable global mode or from a frequency-selection process. Interesting results could be obtained by linking the high-amplitude shock oscillations of the "massive separation", obtained when considering a high deviation angle, to an unstable global mode. On the contrary, it could be shown that the frequency-selection process observed in the "incipient separation" case, caused by small shock angles, can be explained by a singular-value decomposition of the global Resolvent, as for the Délery bump configuration.

The buffet phenomenon has been investigated for a flow at a given combination of Mach and Reynolds number over the OAT15A profile. However, the phenomenon is sensitive to the incoming-flow conditions, and a complete characterisation of the interaction for a wide range of Mach and Reynolds numbers would be interesting and could give some insight on the origins of the unsteadiness. The results of the global modes decomposition have shown the importance of the characteristic lines in the supersonic region, so a finer grid spacing is required in the whole suction side of the profile, not only in the vicinity of the shock. Similarly, the singular-value decomposition of the global Resolvent has shown that medium-frequency unsteadiness are mostly located in the mixing layers developing downstream the trailing edge: a finer mesh that is able to describe the medium scale structures in this particular region of the flow would suit better further studies.

Still concerning the buffet phenomenon, another natural step would be the evalu-

ation of the impact on the unstable eigenvalue of a modification of the base flow due to the presence of a stationary force. To this end, the computation of the sensitivity gradients would give access to control maps that can suggest where the actuators should be placed in order to perform open loop control.

5.2 Acknowledgements

The author would like to acknowledge the experimental and fundamental aerodynamic department of ONERA for the facilities and the computational time provided. First of all, I am grateful to Denis Sipp, who sustained every singular part of the work and elaborated the theoretical method for the stability analysis, and to Clement Mettot, who took care of the numerical implementation of the linearised approach. The experimental investigations would not have been possible without the support of Reynald Bur and the excellent post-processing tools provided by the MTRO unit leaded by Yves Le Sant.

I would also like to acknowledge the "supersonic group" of the IUSTI lab in the Aix-Marseille University for their expertise in the SWBLI domain. A special thanks to Jean-Paul Dussauge, who provided a constant guidance and a thorough support from the beginning to the end of the PhD. For the buffet configuration, I also wish to thank Sébastian Deck, from the ONERA DAAP department, for his helpful advices on the RANS simulations.

In addition, I would like to acknowledge the financial support of the French agency ANR (Agence Nationale de la Recherche) through the DECOMOS program (*DÉcollemnts COMpressibles et OScillations auto-induites*[1]), project number ANR-10-BLANC-914. I am also grateful to the DECOMOS-project partners for the helpful advices that they gave me during the periodic meetings, with a special thanks to Jean-Christophe Robinet and Pierre Dupont for their constant availability and wise suggestions.

Finally, I want to thank all the friendly PhD students and the young researchers of the DAFE department, with a special thanks to Benjamin Leclaire, who has become a constant source of help even if he wasn't supposed to work in this project. Last but definitely not least, I must acknowledge with deep thanks my office mate Claudio Ottonelli: these three years wouldn't have been the same without his daily support, his jokes, and the 15 kg of Italian coffee that we drank together.

[1] Compressible separated flows and self-sustained oscillations.

Appendix A

Résumé en français

Résumé

Dans cette étude nous considérons l'interaction entre une onde de choc et une couche limite turbulente dans un écoulement transsonique sur une bosse d'un point de vue expérimentale et théorique, ainsi que dans un écoulement autour d'un profil d'aile.

Dans le premier cas, des mesures ont permis de montrer que l'interaction est caractérisée par la coexistence de deux fréquences distinctes, mais l'origine des oscillations basse fréquence est controversée. Des simulations numériques s'appuyant sur les équations RANS permettent une description de l'écoulement moyen, mais ne sont pas capables de reproduire le comportement instationnaire de l'interaction. Nous proposons une étude de stabilité globale : une décomposition en valeurs propres de l'opérateur de Navier-Stokes linéarisé au tour d'un champ de base RANS indique que l'interaction est un phénomène stable, et la dynamique de l'écoulement ne peut pas être décrite par un mode global instable.

Nous considérons ensuite une approche linéarisée, où la réceptivité de l'écoulement à un forçage externe est analysée à travers une décomposition en valeurs singulières du Résolvant Global. Cette approche est proposée afin d'expliquer la sélection de fréquence dans cet écoulement, et montre que l'interaction filtre et amplifie le bruit résiduel existant : certaines perturbations sont plus amplifiées dans la couche de mélange, tandis que le choc semble se comporter comme un filtre passe-bas.

La même approche est enfin appliquée sur un cas d'écoulement transsonique autour d'un profil d'aile, qui peut présenter des oscillations périodiques de l'onde de choc. La décomposition en valeurs propres de l'opérateur de Navier-Stokes linéarisé est capable de décrire la dynamique instationnaire quand un mode instable est présent. Cependant, la décomposition en valeurs singulières du Résolvant Global peut indiquer la présence des instabilités convectives qui sont responsables du comportement instationnaire à moyenne fréquence de l'écoulement.

A.1 Introduction

L'interaction d'une onde de choc avec la couche limite conduit à une perte de performance et est responsable d'effets indésirables comme l'augmentation de la traînée, la formation du décollement et des charges aérodynamiques instationnaires (Délery and Marvin, 1986). La physique de ce phénomène, qu'on peut observer sur un profil d'aile ou dans une prise d'air d'un aéronef, est loin d'être bien comprise, notamment pour les aspects qui concernent les oscillations de choc induites par l'interaction (Dolling, 2001).

Dans le domaine des interactions onde de choc/couche limite (IOCCL), trois configurations sont couramment étudiées : la rampe de compression (Ardonceau, 1984; Selig et al., 1989; Thomas et al., 1994; Wu and Martin, 2007), la reflection d'une onde sur une plaque plane (Dupont et al., 2006; Touber and Sandham, 2009a; Humble et al., 2006), et l'onde de choc normale à la paroi (Bur et al., 2006; Bruce and Babinsky, 2008; Pirozzoli et al., 2010a). Dans les deux premiers cas, une onde faible et oblique interagit avec la couche limite et l'écoulement en aval de l'interaction est supersonique. Notre étude se focalise sur une onde de choc forte et normale à la paroi qui interagit avec la couche limite turbulente et devient subsonique après l'interaction. Dans le présent travail, nous considérons une géométrie bien documentée comme la bosse de Délery (Délery, 1978; Loyau et al., 1998; Sandham et al., 2003). L'interaction se caractérise par l'existence d'une onde de choc en lambda qui provoque une séparation massive à partir du pied du choc.

De nombreux études expérimentales (Bogar et al., 1983; Piponniau et al., 2009; Souverein et al., 2010) et numériques (Garnier et al., 2002; Wu and Martin, 2008; Agostini et al., 2012) ont montré la coexistence de deux fréquences caractéristiques distinctes : d'un côté, le battement de l'onde de choc implique généralement une oscillation à basse fréquence, de l'autre côté, la couche de mélange qui se développe après le décollement bat à des fréquences qui sont plus élevées que celles du mouvement de choc, mais plus basses que celles qui sont observées dans la couche limite amont. Pour décrire les instationnarités, la fréquence adimensionalisée ou nombre de Strouhal est couramment utilisée (Erengil and Dolling, 1991b). Avec cette adimensionalisation, Dussauge et al. (2006) ont montré que des valeurs typiques de $S_L = 0.02 - 0.05$ peuvent décrire les mouvements du choc dans plusieurs configurations. Concernant les oscillations à moyenne fréquence, des valeurs typiques de $S_L = 0.1$ jusqu'à $S_L = 0.5$ sont courantes pour les zones décollées, et sont souvent associées à un mouvement de *flapping* (Kiya and Sasaki, 1983). Ces oscillations sont connues depuis longtemps (Cherry et al., 1984) et sont associées à des instabilités de type Kelvin-Helmholtz.

L'origine du mouvement basse fréquence des ondes de choc est controversée : de

nombreuses études ont supposé un lien entre le tremblement de choc et les tourbillons présents dans la couche limite turbulente (Andreopoulos and Muck, 1987; Erengil and Dolling, 1991a; Beresh et al., 2002). Dans une compression sur rampe, Ganapathisubramani et al. (2007) a suggéré que les mouvements des choc sont liés au passage de certaines structures cohérentes provenant de la couche limite en amont. Cependant, d'autres études numériques (Touber and Sandham, 2009b; Hadjadj, 2012) ont montré que ces structures ne sont pas nécessaires pour observer des instationnarités dans la zone du choc. Cette hypothèse a été confirmée par des études expérimentales (Dupont et al., 2006), qui indiquent que les fluctuations de pression dans la couche limite amont sont en très faible cohérence avec les variations de pression générées par le choc : la source de l'instabilité pourrait être l'organisation de l'écoulement en aval par une rétroaction acoustique dans la bulle de recirculation. Les deux théories proposées, quoiqu'en désaccord sur la position, soutiennent l'idée que l'instabilité du système provient d'une source unique. Cependant, un modèle plausible est que l'interaction répond comme un système dynamique qui est forcé par des perturbations externes (Clemens and Narayanaswamy, 2014).

L'analyse de stabilité linéaire est couramment utilisée pour avoir des informations sur le comportement des instationnarités dans un écoulement (Theofilis, 2003; Sipp et al., 2010). Selon Huerre (2000), les instationnarités peuvent être classifiées en deux catégories : l'écoulement peut se comporter comme un oscillateur, et imposer sa propre dynamique, ou il peut avoir un comportement de type amplificateur de bruit. Dans le premier cas, une décompositions en modes globaux peut décrire la dynamique de l'écoulement qui est piloté par un mode global instable (Theofilis, 2011). Dans le deuxième cas, le système filtre et amplifie certains bruits de fond du système à cause des instabilités convectives, et une décomposition en valeurs propres de l'opérateur de Navier-Stokes linearisé ne peut pas décrire la dynamique du système (Trefethen et al., 1993; Sipp et al., 2010).

Dans le domaine des IOCCL, peu d'études ont essayé de répondre à la question des origines des instabilités en utilisant une approche linéaire. Quelques études ont lié les oscillations du choc à un mode global instable (Robinet, 2007; Touber and Sandham, 2009b). Cependant, le mode trouvé est stationnaire, et le lien avec le comportement instable du choc reste une hypothèse. Dans cette étude nous proposons de décrire la dynamique de l'interaction à travers une décomposition en valeurs singulières du Résolvant Global, en étudiant la réponse de l'écoulement à des forçages externes. Cette approche a été appliquée avec succès pour décrire les modes les plus amplifiés dans des écoulements incompressibles (Jovanovic and Bamieh, 2005; McKeon and Sharma, 2010; Brandt et al., 2011). Ensuite, nous considérons un cas similaire d'un écoulement transsonique autour d'un profil. Comme dans d'autres

études (Crouch et al., 2007, 2009), les oscillations périodiques du choc peuvent être décrites par une décomposition en valeurs propres de l'opérateur de Navier-Stokes linearisé. L'analyse du Résolvant Global est capable de mettre en évidence les instabilités convectives qui peuvent se développer à cause du mécanisme de sélection des fréquences présent dans l'écoulement indépendamment de la présence d'un mode instable.

A.2 Résultats expérimentaux

Dans cette partie, nous présentons les principaux résultats obtenus expérimentalement au sein de la soufflerie S8Ch de l'ONERA. La configuration, connue sous le nom de "bosse de Délery", présente une onde de choc à Mach 1.4 provoquant la séparation de la couche limite et une bulle de recirculation créée à partir du pied de choc.

Vélocimétrie par Images de Particules

La Vélocimétrie par Images de Particules (PIV) est devenue un outil incontournable dans l'étude des écoulements complexes. Cette technique permet d'avoir accès aux champs de vitesse moyens sur une partie de l'écoulement. Dans cette étude, le champ PIV, visible en figure A.1, est centré sur l'aval de la bosse et permet de visualiser la partie supersonique et la région décollée résultant de l'interaction avec le choc.

Ce résultat a été obtenu en moyennant en temps un échantillon de 1000 images et ne permet pas de connaître le comportement instationnaire de l'écoulement. Cependant, on peut observer la forme typique de choc dite "en lambda" et la zone décollée qui présente des valeurs de vitesse négatives un ordre de grandeur plus petites que dans la zone supersonique.

Le champ de vitesse permet en outre d'avoir accès aux grandeurs caractéristiques de l'interaction nécessaires pour adimensionner correctement les fréquences dans les sections suivantes. En particulier, la vitesse utilisée comme référence est donnée par la valeur de la composante horizontale de vitesse au dessus de la zone séparée ($U = 300$ m/s). La longueur d'interaction définie comme la distance entre le pied du choc et le centre de la bulle de recirculation est choisie comme longueur de référence.

Mesures instationnaires à la paroi

Pour analyser le comportement en temps de l'interaction, différents capteurs de pression et de frottement ont été placés à la paroi. La figure A.2 montre les spectres obtenus à partir des mesures de pression instationnaires lorsque les capteurs sont

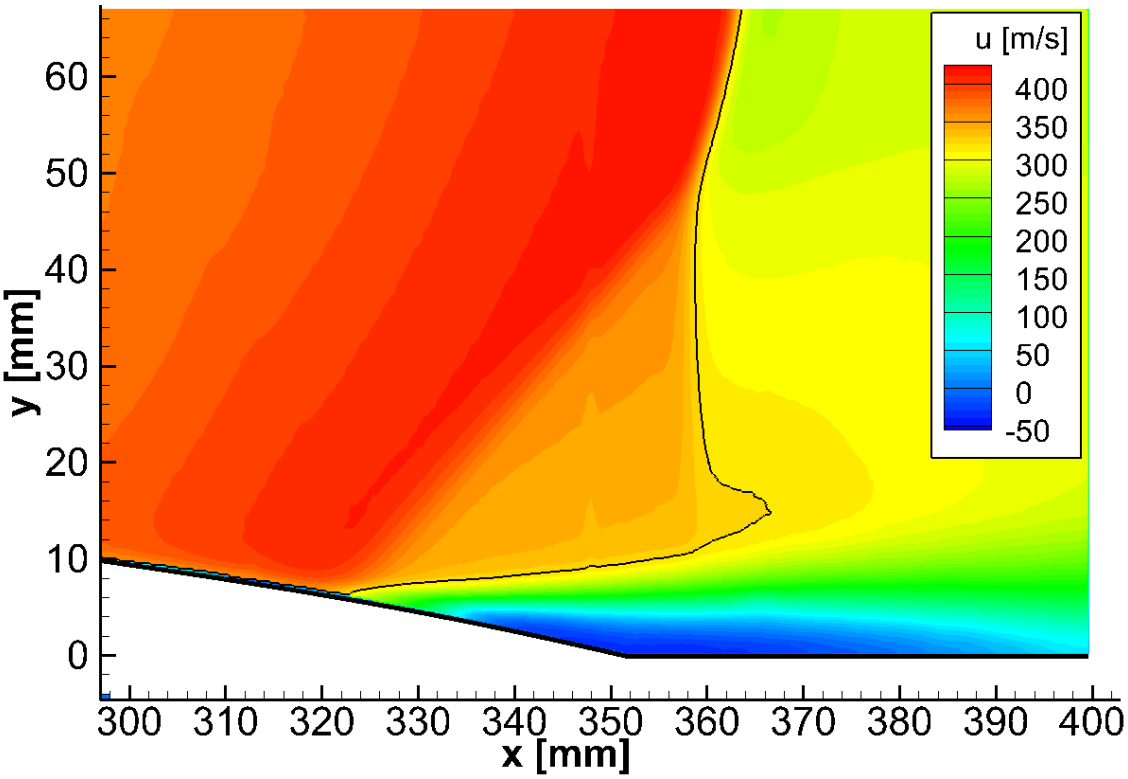

Figure A.1: Champ de vitesse longitudinale obtenu par PIV, isoligne $M = 1$ en noir.

placés au pied de choc (pour $x = 315$ mm), au niveau de la zone décollée ($x = 335$ mm) et au point de recollement (390 mm $< x <$400 mm).

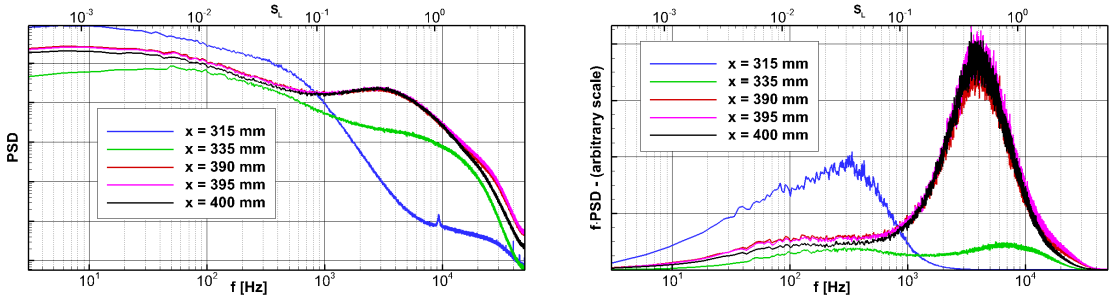

(a) Densité spectrale de puissance.

(b) Spectre premultiplié.

Figure A.2: Spectres de pression à la paroi à différents endroits de l'interaction.

Le principal résultat de cette analyse est que les mouvements du choc sont caractérisés par des oscillations à basse fréquence tandis que les oscillations à moyenne fréquence sont typiques dans la zone décollée.

Visualisation par images de strioscopie

Afin d'accéder à une information plus globale de la distribution spatiale des instationnarités dans l'interaction, l'écoulement a été analysé à l'aide d'images de strioscopie acquises avec une caméra haute cadence. Cette technique de mesure donne accès aux gradients de densité (horizontaux ou verticaux selon l'orientation du couteau) lesquels permettent de caractériser l'onde de choc et les structures tourbillonnaires présentes dans la couche de mélange.

À partir des échantillons (60000 images acquises à une cadence de 35000 Hz), deux traitements sont effectués: une décomposition en modes de Fourier et une cross-correlation des images entres elles. Les deux techniques mettent en exergue la forme spatiale des modes qui représentent les instationnarités typiques de certaines fréquences.

La figure A.3 montre les modes de Fourier obtenus à partir des gradients verticaux de densité pour des fréquences caractéristiques du battement de choc ($f = 300$ Hz pour la figure A.3a) et des instationnarités de la couche de mélange ($f = 4000$ Hz pour la figure A.3b).

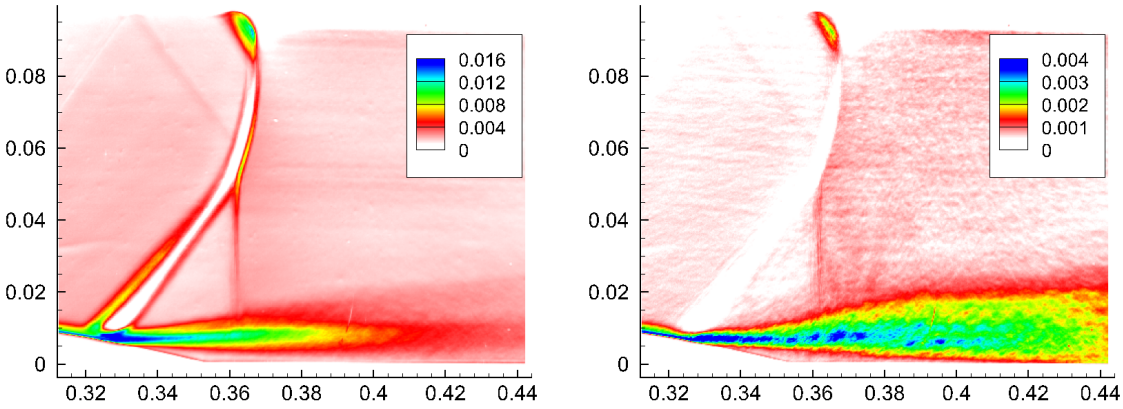

(a) Mode à $f = 300$ Hz.

(b) Mode à $f = 4000$ Hz.

Figure A.3: Modes de Fourier pour le gradient vertical de densité.

La figure A.3 montre que les oscillations à basse fréquence sont typiques de l'intégralité de l'onde de choc et que la partie centrale de la couche de mélange suit les mouvements du choc. Sur un mode de Fourier à plus haute fréquence, la plupart de l'énergie est concentrée dans la zone de cisaillement et le mode n'est plus présent sur le choc.

La figure A.4 montre les résultats de la correlation des images de strioscopie quand le point d'interrogation est dans la couche de mélange. Cette opération permet de mettre en évidence les zones de l'écoulement qui présentent un comportement similaire pendant leur mouvement du au comportement instationnaire

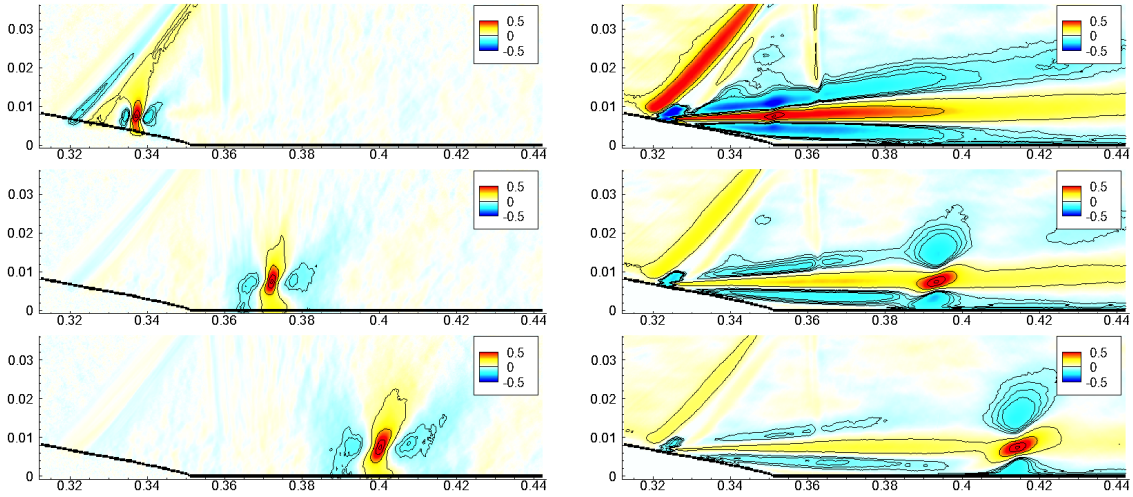

(a) Gradient de densité horizontale $\partial\rho/\partial x$.

(b) Gradient de densité verticale $\partial\rho/\partial y$.

Figure A.4: Correlations pour un point de référence dans la couche de mélange.

de l'interaction.

Lorsque le point d'interrogation est près du point de décollement, les deux résultats produits par les gradients verticaux et horizontaux de densité indiquent que le choc est corrélé avec la couche de mélange. Les battements horizontaux du choc imposent donc un mouvement vertical de la couche de cisaillement. Enfin, lorsque le point d'interrogation est loin du point de séparation, les corrélations sur le choc diminuent en faveur de l'apparition de certaines structures circulaires symétriques par rapport au point d'interrogation. Ce résultat indique la présence des structures tourbillonnaires dans la couche de mélange, lesquelles sont associées grâce aux mesures de pression à la paroi à des fluctuations à moyenne fréquence de la zone cisaillée.

A.3 Approche numérique

Un modèle de type RANS a été choisi pour les simulations numériques et l'analyse de stabilité. L'hypothèse sur laquelle l'étude numérique s'appuie est que les deux phénomènes instationnaires observés expérimentalement sont caractérisés par des fréquences inférieures aux fréquences typiques des structures qui caractérisent les effets de la turbulence. Cette hypothèse de séparation d'échelle de fréquence permet de modéliser l'impact des petites structures sur les plus larges à travers une viscosité turbulente μ_t.

Simulation numérique

Des calculs de type RANS avec un modèle de Spalart-Allmaras ont permis de simuler l'écoulement dans un domaine qui reproduit l'intégralité de la veine d'essai utilisée pour l'étude expérimentale.

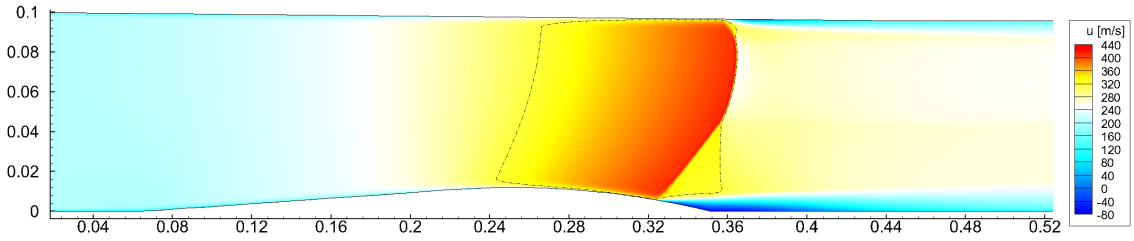

Figure A.5: Composante horizontale de la vitesse. Ligne sonique en pointillée.

Le résultat, présenté en figure A.5, est en accord avec les mesures PIV mais indique que l'écoulement est stationnaire : l'intégration en temps des équations n'est pas capable de reproduire les mouvements à basse fréquence de battement du choc ansi que les fluctuations observées expérimentalement dans la zone cisaillée.

Décomposition en modes globaux

Le résultat de la simulation RANS est ensuite considéré comme champ de base pour une analyse de stabilité : grâce à une linéarisation des équations on obtient la matrice Jacobienne, qui est donnée par :

$$\mathbf{J} = \left.\frac{\partial \mathcal{R}}{\partial \mathbf{w}}\right|_{\mathbf{w}=\mathbf{w_0}} \tag{A.1}$$

où $\mathbf{w_0}$ est le vecteur qui représente le champ de base, solution des équations RANS. À partir de cette matrice nous considérons le problème aux valeurs propres :

$$\mathbf{J}\hat{\mathbf{w}} = \lambda\hat{\mathbf{w}} \tag{A.2}$$

Si au moins une des valeurs propres λ présente un taux d'amplification σ positif, alors l'écoulement est instable. Le spectre obtenu est représenté en figure A.6, où l'on peut observer que les valeurs propres de la matrice Jacobienne sont complètement stables : les instationnarités ne peuvent pas être liées à un mode global instable.

Toutes les valeurs propre à basses fréquences ont une partie réelle faible, et aucun mode ne peut être observé à la fréquence caractéristique du battement du choc. Parmi les valeurs propres stables à moyenne fréquence, certaines sont très proches de l'axe imaginaire : les modes globaux associés, représentés en figure A.7, sont des modes acoustiques, liés aux résonances du tuyau et non pas à la dynamique de la zone décollée.

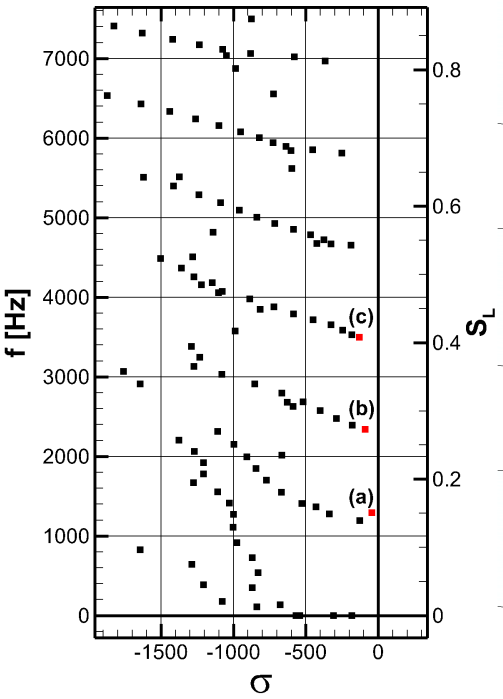

Figure A.6: Valeurs propres.

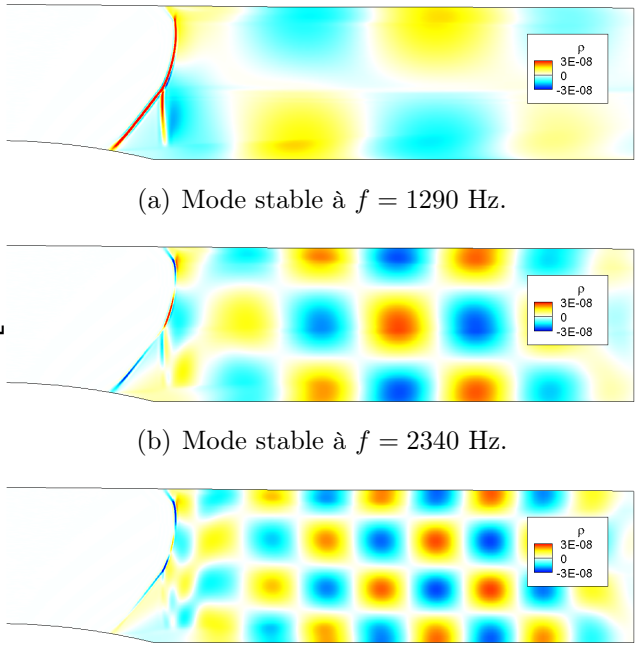

(a) Mode stable à $f = 1290$ Hz.

(b) Mode stable à $f = 2340$ Hz.

(c) Mode stable à $f = 3500$ Hz.

Figure A.7: Modes globaux stables.

Le Résolvant Global

Vu l'absence de modes globaux instables, la dynamique de l'interaction est de type amplificateur de bruit. Pour décrire le mécanisme de sélection de fréquences nous considérons le Résolvant Global, qui est définit par

$$\mathscr{R} = (i\omega \mathbf{I} - \mathbf{J})^{-1} \tag{A.3}$$

où $\mathbf{J}$ est la matrice Jacobienne et $\mathbf{I}$ est la matrice identité. Le Résolvant Global existe pour chaque fréquence ω, car toutes les valeurs propres de $\mathbf{J}$ sont à partie réelle négative, et met en relation la réponse de l'écoulement $\hat{\mathbf{w}}$ quand il est soumis à un forçage externe $\hat{\mathbf{f}}$ à travers $\hat{\mathbf{w}} = \mathscr{R}\hat{\mathbf{f}}$. Grâce à une décomposition en valeurs singulières de la matrice $\mathscr{R}$ on peut calculer le forçage (dit optimal), à une certaine fréquence, qui produit la réponse la plus énergétique de l'écoulement. En faisant cette opération pour toutes les fréquences ω on obtient la courbe de gain $G(\omega)$, qui représente le ratio entre l'énergie de la réponse obtenue par un forçage optimal et le forçage lui-même.

L'évolution en fréquence de la courbe de gain, donnée par la valeur propre la plus énergétique λ_1 du Résolvant Global, est montrée en figure A.8. Cette courbe indique que l'interaction est très sensible aux basses fréquences, caractéristiques du battement du choc, et aux moyennes fréquences, caractéristiques des fluctuations de la couche de mélange.

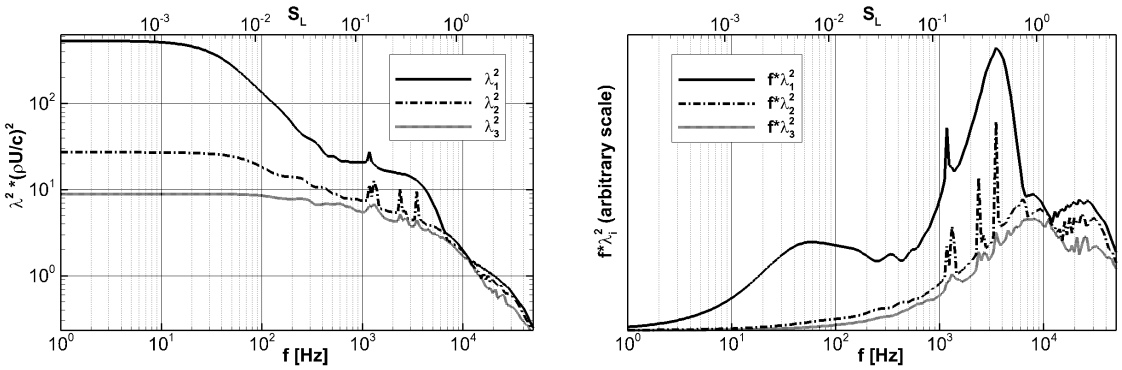

(a) Fonction de gain, échelle logarithmique. (b) Gain premultiplié.

Figure A.8: Valeurs propres du Résolvant Global. Chaque λ_i représente le gain quand l'écoulement est forcé, à la fréquence f, avec un forçage optimal.

La figure A.8b montre le gain premultiplié, où l'on peut observer que la réponse la plus énergétique pour un forçage optimal à basse fréquence est obtenue pour $f = 50$ Hz. Cette réponse est représentée en figure A.9.

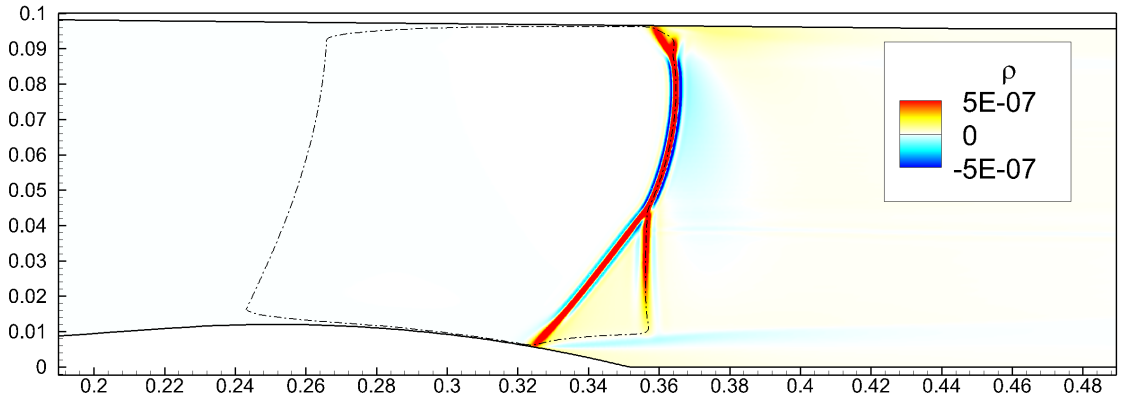

Figure A.9: Réponse optimale à fréquence $f = 50$ Hz.

La réponse est concentrée uniquement sur le choc, et indique qu'un forçage à basse fréquence est capable d'activer une réponse de l'écoulement qui est sur le choc. On peut observer des similarités entre la réponse optimale et le mode de Fourier obtenu expérimentalement à partir des images de strioscopie, représenté en figure A.3.

La figure A.10 montre la réponse obtenue quand l'écoulement est forcé à travers un forçage optimal à 4000 Hz, fréquence pour laquelle la courbe de gain de la figure A.8b est maximale.

La réponse n'est pas dans le choc comme dans le cas à basse fréquence, mais est plutôt concentrée dans la zone cisaillée, avec des structures circulaires périodiques qui commencent à partir du point de décollement. Un comportement similaire a déjà

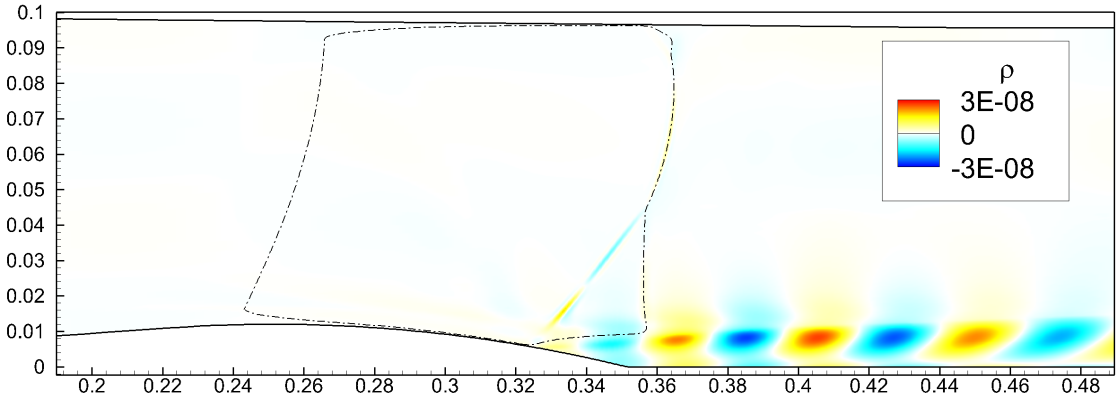

Figure A.10: Réponse optimale à fréquence $f = 4000$ Hz.

été observé dans l'analyse expérimentalebasé sur la corrélation croisée des images de strioscopie, et indique que les mouvements à moyennes fréquences de l'interaction sont dues à une instabilité de type Kelvin-Helmholtz dans la couche de cisaillement.

A.4 Tremblement transsonique sur le profil OAT15A

Dans cette partie nous avons considéré un autre type d'IOCCL : un écoulement transsonique autour d'un profile de type OAT15A. Ce type d'écoulement présente des similarités avec la configuration analysée précédemment, avec la principale différence que, pour certaines incidences, l'onde de choc est soumise à des mouvements périodiques de grande amplitude. La zone décollée s'étend périodiquement du pied de choc au sillage du profil considéré et produit un lâcher de structures tourbillonnaires.

Simulation numérique

La même approche décrite pour la configuration de Délery est appliquée à cet écoulement, qui a été précédemment analysé expérimentalement par Jacquin et al. (2009). Pour toutes les incidences considérées, les simulations RANS arrivent à la définition d'un champ de base qui est utilisé pour l'analyse de stabilité. Pour certaines incidences (dès $\alpha = 3.5°$ jusqu'à $\alpha = 6.0°$), l'intégration des équations en temps reproduit le mouvement de battement de choc connu comme le "buffet".

La figure A.11a montre la solution RANS obtenue pour $\alpha = 3.5°$: on peut observer la présence, comme dans le cas de la bosse de Délery, d'une onde de choc qui provoque la séparation de la couche limite turbulente, et une bulle de recirculations s'étend du pieds de choc jusqu'au bord de fuite du profil.

La figure A.11b montre les effets de l'instationnarité du choc sur le coefficient

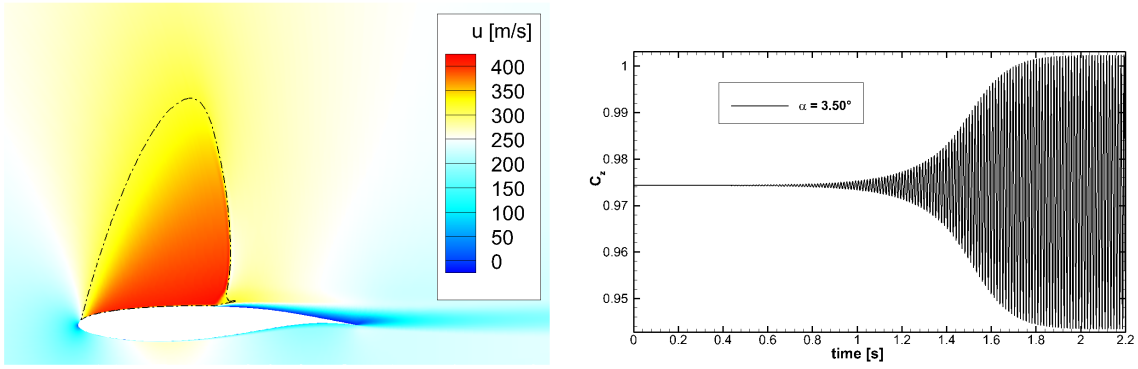

(a) Champs de vitesse horizontale. (b) Évolution du coefficient de pression.

Figure A.11: Solutions RANS et URANS pour $\alpha = 3.5°$.

de pression : l'évolution du Cp en fonction du temps indique que l'écoulement est caractérisé par des oscillations périodiques de l'onde de choc, pour une fréquence d'environ 80 Hz.

Analyse de stabilité

Une analyse de stabilité linéaire comme pour le cas précédent est appliquée pour ce type d'écoulement. Pour chaque incidence, les simulations RANS donnent un champ de base qui est linéarisé pour obtenir la matrice Jacobienne. Ensuite, chaque configuration est analysée par décomposition en valeurs propres.

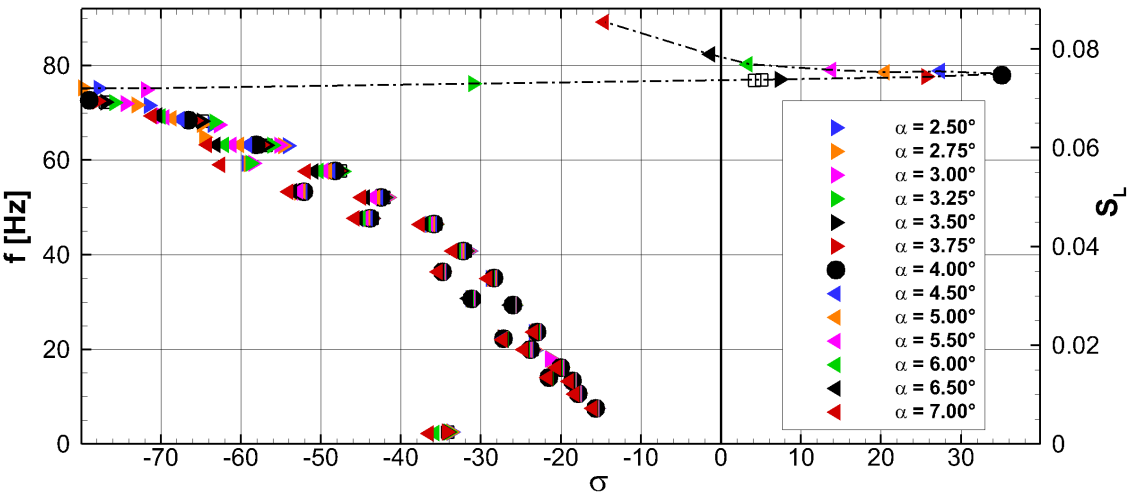

Figure A.12: Valeurs propres pour différentes incidences.

Contrairement au cas précédent, un mode global instable apparaît pour des incidences comprises entre $\alpha = 3.5°$ et $\alpha = 6.0°$. Le spectre montrant l'évolution de cette valeur propre instable en fonction de l'incidence est présenté en figure A.12 :

on peut observer que, en accord avec la simulation URANS, la fréquence du mode instable est à 80 Hz, et la configuration la plus instable arrive pour $\alpha = 4.0°$.

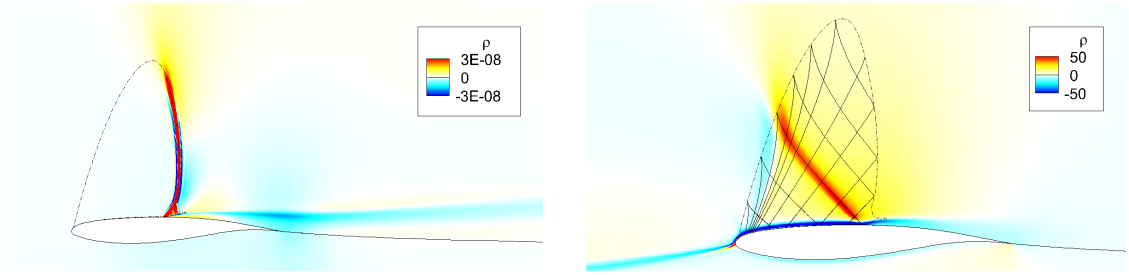

(a) Mode direct. (b) Mode adjoint.

Figure A.13: Modes instables pour $\alpha = 4.0°$. Composante de densité.

Le mode direct instable associé à la valeur propre à partie réelle positive est présenté, pour le cas $\alpha = 4.0°$, en figure A.13a : le mode, principalement sur l'onde de choc indique, comme observé par Crouch et al. (2007), que l'origine du tremblement transsonique est une instabilité de type globale.

En considérant le problème adjoint aux valeurs propres, on a accès aux modes instables adjoints associé à l'instabilité de buffet. Ce mode, représenté en figure A.13b, est énergétique sur la couche limite en amont du décollement et suit la ligne caractéristique descendante qui arrive sur le pied de choc.

La décomposition en valeurs propres de la matrice Jacobienne permet de reproduire correctement les mouvements périodiques de battement du choc observé expérimentalement et par simulation numérique. Cependant, dans l'écoulement d'autres types d'instationnarités, comme dans le cas de la bosse de Délery, peuvent arriver. Pour répondre à la question des instabilités convectives nous considérons le Résolvant Global. Indépendamment de la nature stable ou instable de l'écoulement, la courbe de gain introduite dans la section précédente peut mettre en évidence un mécanisme de sélection de fréquence qui peut se manifester dans ce type d'interaction.

Encore une fois, l'évolution de la valeur propre la plus énergétique du Résolvant Global, présentée en figure A.14a, indique que l'écoulement est sensible aux forçages à basses fréquences (autour de $f = 80$ Hz) et à moyennes fréquences (entre $f = 1$ kHz et $f = 4$ kHz). La présence de la valeur propre instable $f = 80$ Hz cause le pic dans la courbe de gain qui, contrairement au cas de la bosse, est lié à une instabilité globale. En considérant la courbe de gain à moyenne fréquence, un pic à une fréquence qui décroît avec l'augmentation de l'incidence peut être observé.

La figure A.14b montre la réponse optimale à fréquence $f = 3000$ Hz pour le cas $\alpha = 4.0°$. Comme dans le cas de la bosse de Délery l'instationnarité à moyenne

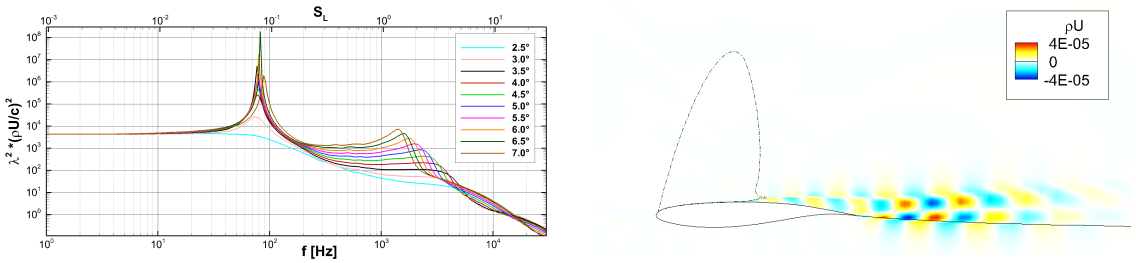

(a) Fonction de gain. (b) Réponse optimale à $f = 3000$ Hz, $\alpha = 4.0°$.

Figure A.14: Analyse du Résolvant Global : instabilités convectives.

fréquence est caractérisé par des modes de type Kelvin-Helmholtz qui se développent à partir des deux zones cisaillées produites par le décollement et par le bord de fuite. Ce résultat indique que, à part la présence du battement de l'onde de choc présent pour certaines fréquences, l'écoulement autour d'un profil est caractérisé par des oscillations à moyennes fréquences, présentes pour toutes les incidences, qui sont liées à la présence de la couche de mélange.

A.5 Conclusions

L'objectif de cette étude était double : décrire la dynamique instable de l'interaction entre une onde de choc et une couche limite turbulente sur la configuration dite "bosse de Délery", et adresser le problème des instationnarités en utilisant l'analyse de stabilité.

L'étude expérimentale a permis de caractériser la configuration considérée : l'écoulement moyen a été analysé par PIV, et le comportement instable a été décrit par des mesures à la paroi et par des images de strioscopie à haute cadence. Le choc est affecté par des instabilités à basse fréquence, tandis que la zone décollée est siège de fluctuations à moyennes fréquences. En calculant le nombre de Strouhal, les fréquences des mouvements du choc et de la couche de mélange se comparent favorablement avec d'autres études.

Des simulations de type RANS ont ensuite donné accès à l'écoulement moyen, qui reproduit l'interaction comme observé expérimentalement. Une analyse de stabilité linéaire a alors été proposée : l'absence de modes globaux instables a indiqué que l'écoulement se comporte comme un amplificateur de bruit et sa dynamique ne peut pas être décrite par une décomposition en valeurs propres. Une formulation théorique basée sur une décomposition en valeurs singulières du Résolvant Global a alors été proposée : il a été montré que la non normalité de l'opérateur linéaire a une grande importance dans la description du processus de sélection de

fréquences observées expérimentalement. Le résultat principal de cette approche est la confirmation que l'instabilité à basse fréquence ne vient pas d'une instabilité globale, mais est la réponse de l'écoulement au bruit environnemental auquel il est soumis. En ce qui concerne les fluctuations à basse fréquence, le forçage optimal est maximal au pied de choc. Considérant les fluctuations à moyenne fréquence, les instationnarités observés dans la couche de mélange sont liés à une instabilité de type Kelvin-Helmholtz, qui existe indépendamment de la présence du choc.

L'approche appliquée à la configuration bosse de Délery a ensuite été utilisée pour étudier la configuration transsonique d'un écoulement autour du profil OAT15A. Dans ce cas, les mouvements périodiques du choc, lorsqu'ils sont présents, peuvent être correctement reproduits par l'approche RANS, et la décomposition en valeurs propres peut prédire l'instabilité à basse fréquence. Concernant les instabilités convectives, la décomposition en valeurs singulières a indiqué que l'écoulement est sujet aux instabilités à basse fréquence même avant le début du phénomène de buffet. À part les mouvements périodiques du choc, il a été démontré que les sources les plus énergétiques d'instabilités sont les couches de mélange en développement du point de séparation et du bord de fuite du profil.

Perspectives

En ce qui concerne l'étude expérimentale, les résultats obtenus avec les correlations des images de strioscopie ont montré le potentiel de la technique, mais pourraient être améliorés avec des acquisitions de données plus longues, qui donneraient une meilleure résolution temporelle dans la décomposition de Fourier.

En ce qui concerne l'étude numérique, l'extension de l'analyse de stabilité à différentes configurations comme le cas IUSTI pourrait donner des résultats intéressants. La suite naturelle de l'approche linéarisée serait le calcul des gradients de sensibilité, pour avoir accès aux informations concernants le contrôle de l'écoulement.

Remerciements

Ce travail de thèse a été réalisé au département DAFE de l'ONERA, où je tiens à remercier Denis Sipp, qui a encadré la totalité de l'étude, et Reynald Bur, qui à rendu possible les études expérimentales en soufflerie. Je tiens à remercier le "groupe supersonique" du laboratoire IUSTI à l'Aix-Marseille Université, dirigé par Jean-Paul Dussauge, pour leur expertise dans le domaine des IOCCL. Enfin, je remercie le soutien financier de l'Agence Nationale de la Recherche à travers le programme DECOMOS (DÉcollemnts COMpressibles et OScillations auto-induites), sous le projet numéro ANR-10-BLANC-914.

Bibliography

Abdessemed, N., Sharma, A. S., Sherwin, S. J., and Theofilis, V. (2009). Transient growth analysis of the flow past a circular cylinder. *Physics of Fluids*, 21:044103.

Agostini, L., Larchevêque, L., Dupont, P., Debiève, J. F., and Dussauge, J. P. (2012). Zones of influence and shock motion in a shock/boundary-layer interaction. *AIAA journal*, 50(6):1377–1387.

Andreopoulos, J. and Muck, K. C. (1987). Some new aspects of the shock-wave/boundary-layer interaction in compression-ramp flows. *Journal of Fluid Mechanics*, 180(1):405–428.

Ardonceau, P. L. (1984). The structure of turbulence in a supersonic shock-wave/boundary-layer interaction. *AIAA journal*, 22(9):1254–1262.

Barakos, G. and Drikakis, D. (2000). Numerical simulation of transonic buffet flows using various turbulence closures. *International Journal of Heat and Fluid Flow*, 21(5):620–626.

Barkley, D., Gomes, M. G. M., and Henderson, R. D. (2002). Three-dimensional instability in flow over a backward-facing step. *Journal of Fluid Mechanics*, 473:167–190.

Beresh, S. J., Clemens, N. T., and Dolling, D. S. (2002). Relationship between upstream turbulent boundary-layer velocity fluctuations and separation shock unsteadiness. *AIAA journal*, 40(12):2412–2422.

Blackburn, H. M., Barkley, D., and Sherwin, S. J. (2008). Convective instability and transient growth in flow over a backward-facing step. *Journal of Fluid Mechanics*, 603:271–304.

Bogar, T. J., Sajben, M., and Kroutil, J. C. (1983). Characteristic frequencies of transonic diffuser flow oscillations. *AIAA journal*, 21(9):1232–1240.

Brandt, L., Sipp, D., Pralits, J. O., and Marquet, O. (2011). Effect of base-flow variation in noise amplifiers: the flat-plate boundary layer. *Journal of Fluid Mechanics*, 687:503–528.

Bruce, P. J. K. and Babinsky, H. (2008). Unsteady shock wave dynamics. *Journal of Fluid Mechanics*, 603:463–473.

Bruce, P. J. K., Burton, D. M. F., Titchener, N. A., and Babinsky, H. (2011). Corner effect and separation in transonic channel flows. *Journal of Fluid Mechanics*, 679:247–262.

Brunet, V. (2003). Computational study of buffet phenomenon with unsteady rans equations. *AIAA paper*, 2003–3679.

Bur, R., Benay, R., Galli, A., and Berthouze, P. (2006). Experimental and numerical study of forced shock-wave oscillations in a transonic channel. *Aerospace science and technology*, 10(4):265–278.

Bur, R., Coponet, D., and Carpels, Y. (2009). Separation control by vortex generator devices in a transonic channel flow. *Shock Waves*, 19(6):521–530.

Bur, R., Corbel, B., and Délery, J. (1998). Study of passive control in a transonic shock wave/boundary-layer interaction. *AIAA journal*, 36(3):394–400.

Cambier, L., Heib, S., and Plot, S. (2012). The onera elsa cfd software: input from research and feedback from industry. In *28th International Congress of the Aeronautical Sciences, ICAS*, volume 2.

Champagnat, F., Plyer, A., Le Besnerais, G., Leclaire, B., Davoust, S., and Le Sant, Y. (2011). Fast and accurate PIV computation using highly parallel iterative correlation maximization. *Experiments in fluids*, 50(3):1–14.

Chapman, D. R., Kuehn, D. M., and Larson, H. K. (1958). Investigation of separated flows in supersonic and subsonic streams with emphasis on the effect of transition. *US Government Printing Office*.

Cherry, N. J., Hillier, R., and Latour, M. E. M. (1984). Unsteady measurements in a separated and reattaching flow. *Journal of Fluid Mechanics*, 144:13–46.

Chomaz, J. M. (2005). Global instabilities in spatially developing flows: non-normality and nonlinearity. *Annu. Rev. Fluid Mech.*, 37:357–392.

Clemens, N. T. and Narayanaswamy, V. (2014). Low-frequency unsteadiness of shock wave/turbulent boundary layer interactions. *Annu. Rev. Fluid Mech*, 46:469–92.

Cossu, C. and Chomaz, J. M. (1997). Global measures of local convective instabilities. *Physical review letters*, 78(23):4387.

Cossu, C., Pujals, G., and Depardon, S. (2009). Optimal transient growth and very large-scale structures in turbulent boundary layers. *Journal of Fluid Mechanics*, 619:79.

Crouch, J. D., Garbaruk, A., and Magidov, D. (2007). Predicting the onset of flow unsteadiness based on global instability. *Journal of Computational Physics*, 224(2):924–940.

Crouch, J. D., Garbaruk, A., Magidov, D., and Travin, A. (2009). Origin of transonic buffet on aerofoils. *Journal of Fluid Mechanics*, 628(1):357–369.

Debiève, J. F. and Dupont, P. (2009). Dependence between the shock and the separation bubble in a shock wave boundary layer interaction. *Shock Waves*, 19(6):499–506.

Deck, S. (2005). Numerical simulation of transonic buffet over the oat15a airfoil. *AIAA journal*, 43(7):1556–1566.

Délery, J. (1978). Analysis of the separation due to shock wave-turbulent boundary layer interaction in transonic flow. *La Recherche Aerospatiale*, pages 305–320.

Délery, J. (1983). Experimental investigation of turbulence properties in transonic shock/boundary-layer interactions. *AIAA journal*, 21:180–185.

Délery, J. (1999). Flow physics involved in shock wave/boundary layer interaction control. In *IUTAM Symposium on Mechanics of Passive and Active Flow Control: proceedings of the IUTAM Symposium held in Göttingen, Germany, 7-11 September 1998*, volume 53, page 15. Springer Netherlands.

Délery, J. (2000). Flow physics involved in shock wave/boundary layer interaction control. In *Iutam Symposium on Mechanics of Passive and Active Flow Control*, pages 15–22. Springer.

Délery, J. and Marvin, J. G. (1986). Shock-wave boundary layer interactions. *AGARDograph*.

Dolling, D. S. (2001). Fifty years of shock-wave/boundary-layer interaction research: what next? *AIAA journal*, 39(8):1517–1531.

Dolling, D. S. and Brusniak, L. (1989). Separation shock motion in fin, cylinder, and compression ramp-induced turbulent interactions. *AIAA journal*, 27(6):734–742.

Dolling, D. S. and Erengil, M. E. (1991). Unsteady wave structure near separation in a mach 5 compression ramp interaction. *AIAA journal*, 29(5):728–735.

Dovgal, A. V., Kozlov, V. V., and Michalke, A. (1994). Laminar boundary layer separation: instability and associated phenomena. *Progress in Aerospace Sciences*, 30(1):61–94.

Drazin, P. G. and Reid, W. H. (1980). *Solutions to the Problems in Hydrodynamic Stability*. Cambridge Univ Press.

Dupont, P., Haddad, C., and Debiève, J. F. (2006). Space and time organization in a shock-induced separated boundary layer. *Journal of Fluid Mechanics*, 559:255–278.

Dupont, P., Piponniau, S., Sidoren, A., and Debiève, J. F. (2008). Investigation by particle image velocimetry measurements of oblique shock reflection with separation. *AIAA journal*, 46(6):1365–1370.

Dussauge, J. P., Dupont, P., and Debiève, J. F. (2006). Unsteadiness in shock wave boundary layer interactions with separation. *Aerospace Science and Technology*, 10(2):85–91.

Dussauge, J. P. and Piponniau, S. (2008). Shock/boundary-layer interactions: Possible sources of unsteadiness. *Journal of Fluids and Structures*, 24(8):1166–1175.

Ehrenstein, U. and Gallaire, F. (2005). On two-dimensional temporal modes in spatially evolving open flows: the flat-plate boundary layer. *Journal of Fluid Mechanics*, 536:209–218.

Ehrenstein, U. and Gallaire, F. (2008). Two-dimensional global low-frequency oscillations in a separating boundary-layer flow. *Journal of Fluid Mechanics*, 614:315–327.

Elena, M. and LaCharme, J. P. (1988). Experimental study of a supersonic turbulent boundary layer using a laser doppler anemometer. *Journal de mécanique théorique et appliquée*, 7(2):175–190.

Elsinga, G. E., Van Oudheusden, B. W., and Scarano, F. (2005). Evaluation of aero-optical distortion effects in PIV. *Experiments in fluids*, 39(2):246–256.

Erengil, M. E. and Dolling, D. S. (1991a). Correlation of separation shock motion with pressure fluctuations in the incoming boundary layer. *AIAA journal*, 29(11):1868–1877.

Erengil, M. E. and Dolling, D. S. (1991b). Unsteady wave structure near separation in a mach 5 compression ramp interaction. *AIAA journal*, 29(5):728–735.

Farrell, B. F. and Ioannou, P. J. (1996). Generalized stability theory. part i: Autonomous operators. *Journal of the atmospheric sciences*, 53(14):2025–2040.

Gallaire, F., Marquillie, M., Ehrenstein, U., et al. (2007). Three-dimensional transverse instabilities in detached boundary layers. *Journal of Fluid Mechanics*, 571:221–234.

Galli, A., Corbel, B., and Bur, R. (2005). Control of forced shock-wave oscillations and separated boundary layer interaction. *Aerospace science and technology*, 9(8):653–660.

Ganapathisubramani, B., Clemens, N., and Dolling, D. (2009). Low-frequency dynamics of shock-induced separation in a compression ramp interaction. *Journal of Fluid Mechanics*, 636(1):397–425.

Ganapathisubramani, B., Clemens, N. T., and Dolling, D. S. (2007). Effects of upstream boundary layer on the unsteadiness of shock-induced separation. *Journal of Fluid Mechanics*, 585:369–394.

Garnier, E. (2009). Stimulated detached eddy simulation of three-dimensional shock/boundary layer interaction. *Shock waves*, 19(6):479–486.

Garnier, E., Sagaut, P., and Deville, M. (2002). Large eddy simulation of shock/boundary-layer interaction. *AIAA journal*, 40(10):1935–1944.

Giles, M. B. and Pierce, N. A. (1997). Adjoint equations in cfd: duality, boundary conditions and solution behaviour. *AIAA paper*, 97–1850.

Giles, M. B. and Pierce, N. A. (2001). Analytic adjoint solutions for the quasi-one-dimensional euler equations. *Journal of Fluid Mechanics*, 426(2001):327–345.

Grilli, M., Schmid, P. J., Hickel, S., and Adams, N. A. (2012). Analysis of unsteady behaviour in shockwave turbulent boundary layer interaction. *Journal of Fluid Mechanics*, 700:16–28.

Hadjadj, A. (2012). Large-eddy simulation of shock/boundary-layer interaction. *AIAA journal*, 50(12):2919–2927.

Hadjadj, A. and Dussauge, J. P. (2009). Shock wave boundary layer interaction. *Shock Waves*, 19(6):449–452.

Harten, A. and Hyman, J. M. (1983). Self adjusting grid methods for one-dimensional hyperbolic conservation laws. *Journal of Computational Physics*, 50(2):235–269.

Hartmann, A., Klaas, M., and Schröder, W. (2011). Time-resolved stereo PIV measurements of shock–boundary layer interaction on the oat15a airfoil. *Experiments in Fluids*, 50(3):1–14.

Hou, Y. X., Clemens, N. T., and Dolling, D. S. (2002). Multi-frame PIV imaging of shock/turbulent boundary layer interactions. In *APS Meeting Abstracts*, volume 1.

Hou, Y. X., Clemens, N. T., and Dolling, D. S. (2003). Wide-field PIV study of shock-induced turbulent boundary layer separation. *AIAA paper*, 2003-0441.

Huang, J., Xiao, Z., Liu, J., and Fu, S. (2012). Simulation of shock wave buffet and its suppression on an oat15a supercritical airfoil by iddes. *Science China Physics, Mechanics and Astronomy*, 55(2):260–271.

Huerre, P. (2000). Open shear flow instabilities. *Perspectives in Fluid Dynamics*, pages 159–229.

Humble, R. A., Elsinga, G. E., Scarano, F., and Van Oudheusden, B. W. (2009). Three-dimensional instantaneous structure of a shock wave/turbulent boundary layer interaction. *Journal of Fluid Mechanics*, 622(1):33.

Humble, R. A., Scarano, F., and Van Oudheusden, B. W. (2006). Experimental study of an incident shock wave/turbulent boundary layer interaction using PIV. *AIAA paper*, 2006-3361.

Humble, R. A., Scarano, F., and Van Oudheusden, B. W. (2007). Particle image velocimetry measurements of a shock wave/turbulent boundary layer interaction. *Experiments in Fluids*, 43(43):173–183.

Jackson, C. P. (1987). A finite-element study of the onset of vortex shedding in flow past variously shaped bodies. *Journal of Fluid Mechanics*, 182(1):23–45.

Jacquin, L., Molton, P., Deck, S., Maury, B., and Soulevant, D. (2005). An experimental study of shock oscillation over a transonic supercritical profile. *AIAA paper*, 2003–4902.

Jacquin, L., Molton, P., Deck, S., Maury, B., and Soulevant, D. (2009). Experimental study of shock oscillation over a transonic supercritical profile. *AIAA journal*, 47(9):1985–1994.

Johnson, D. A., Bachalo, W. D., and Owen, F. K. (1981). Transonic flow past a symmetrical airfoil at high angle of attack. *Journal of Aircraft*, 18(1):7–14.

Jovanovic, M. R. and Bamieh, B. (2005). Componentwise energy amplification in channel flows. *Journal of Fluid Mechanics*, 534:145–184.

Juan, C. and Javier, J. (2006). Linear energy amplification in turbulent channels. *Journal of Fluid Mechanics*, 559:205–213.

Kiya, M. and Sasaki, K. (1983). Structure of a turbulent separation bubble. *Journal of Fluid Mechanics*, 137:83–113.

Knight, D. D. and Degrez, G. (1998). Shock wave boundary layer interactions in high mach number flows a critical survey of current numerical prediction capabilities. *AGARD ADVISORY REPORT AGARD AR*, 2:1–1.

Koch, W. (1985). Local instability characteristics and frequency determination of self-excited wake flows. *Journal of Sound and Vibration*, 99(1):53–83.

Koch, W. (2005). Acoustic resonances in rectangular open cavities. *AIAA journal*, 43(11):2342–2349.

Kussoy, M. I., Brown, J. D., Brown, J. L., Lockman, W. K., and Horstman, C. C. (1988). Fluctuations and massive separation in three-dimensional shock-wave/boundary-layer interactions. In *Transport Phenomena in Turbulent Flows: Theory, Experiment, and Numerical Simulation*, pages 875–887. edited by M. Hirata and N. Kasagi. Hemisphere, New York.

Lapsa, A. P. and Dahm, W. J. A. (2011). Stereo particle image velocimetry of nonequilibrium turbulence relaxation in a supersonic boundary layer. *Experiments in Fluids*, 50(1):89–108.

Larchevêque, L., Dupont, P., De Martel, E., Garnier, E., and Debiève, J. F. (2010). Experimental and numerical study of unsteadiness in boundary layer/shock wave interaction. In *Turbulence and Interactions*, pages 263–269. Springer.

Lee, B. H. K. (1990). Oscillatory shock motion caused by transonic shock boundary-layer interaction. *AIAA journal*, 28(5):942–944.

Lee, B. H. K. (2001). Self-sustained shock oscillations on airfoils at transonic speeds. *Progress in Aerospace Sciences*, 37(2):147–196.

Lehoucq, R., Sorensen, D., and Yang, C. (1998). *Arpack User's Guide: Solution of Large-Scale Eigenvalue Problems With Implicityly Restorted Arnoldi Methods*. Number 6. Siam.

Liepmann, H. H. W. (1957). *Elements of gas dynamics*. Courier Dover Publications.

Loyau, H., Batten, P., and Leschziner, M. A. (1998). Modelling shock/boundary-layer interaction with nonlinear eddy-viscosity closures. *Flow, turbulence and combustion*, 60(3):257–282.

Marquet, O., Lombardi, M., Chomaz, J., Sipp, D., and Jacquin, L. (2009). Direct and adjoint global modes of a recirculation bubble: lift-up and convective non-normalities. *Journal of Fluid Mechanics*, 622:1–21.

Marquet, O., Sipp, D., Chomaz, J. M., and Jacquin, L. (2008a). Amplifier and resonator dynamics of a low-reynolds-number recirculation bubble in a global framework. *Journal of Fluid Mechanics*, 605:429.

Marquet, O., Sipp, D., and Jacquin, L. (2008b). Sensitivity analysis and passive control of cylinder flow. *Journal of Fluid Mechanics*, 615:221.

Mary, I., Sagaut, P., and Deville, M. (2000). An algorithm for unsteady viscous flows at all speeds. *International journal for numerical methods in fluids*, 34(5):371–401.

McDevitt, J. B. and Okuno, A. F. (1985). Static and dynamic pressure measurements on a naca 0012 airfoil in the ames high reynolds number facility. *Tech Paper NASA*, 2485.

McKeon, B. J. and Sharma, A. S. (2010). A critical-layer framework for turbulent pipe flow. *Journal of Fluid Mechanics*, 658(1):336–382.

Mettot, C., Renac, F., and Sipp, D. (2013). Computation of eigenvalue sensitivity to base flow modifications in a discrete framework: Application to open-loop control. *Under consideration for publication in Journal of Computational Physics*.

Mitchell, D., Honnery, D., and Soria, J. (2011). Particle relaxation and its influence on the particle image velocimetry cross-correlation function. *Experiments in Fluids*, 50(5):1–15.

Muller, J., Mummler, R., and Staudacher, W. (2001). Comparison of some measurement techniques for shock-induced boundary layer separation. *Aerospace science and technology*, 5(6):383–395.

Orr, W. M. F. (1907). The stability or instability of the steady motions of a perfect liquid and of a viscous liquid. part ii: A viscous liquid. In *Proceedings of the Royal Irish Academy. Section A: Mathematical and Physical Sciences*, volume 27, pages 69–138. JSTOR.

Papamoschou, D. and Roshko, A. (1988). The compressible turbulent shear layer: an experimental study. *J. Fluid Mech*, 197(453).

Pearcey, H. H. (1958). A method for the prediction of the onset of buffeting and other separation effects from wind tunnel tests on rigid models. Technical report, DTIC Document.

Pearcey, H. H. and Holder, D. W. (1962). Simple methods for the prediction of wing buffeting resulting from bubble type separation. *Aero Rep*, 1024.

Piponniau, S., Dussauge, J. P., Debiève, J. F., and Dupont, P. (2009). A simple model for low-frequency unsteadiness in shock-induced separation. *J. Fluid Mech*, 629:87–108.

Pirozzoli, S., Bernardini, M., and Grasso, F. (2010a). Direct numerical simulation of transonic shock/boundary layer interaction under conditions of incipient separation. *Journal of Fluid Mechanics*, 657:361–393.

Pirozzoli, S. and Grasso, F. (2006). Direct numerical simulation of impinging shock wave turbulent boundary layer interaction at M = 2.25. *Physics of Fluids*, 18:065113.

Pirozzoli, S., Larsson, J., Nichols, J. W., Bernardini, M., Morgan, B. E., and Lele, S. K. (2010b). Analysis of unsteady effects in shock/boundary layer interactions. *Annu. Res. Briefs*, pages 153–164.

Plotkin, K. J. (1975). Shock wave oscillation driven by turbulent boundary-layer fluctuations. *AIAA Journal*, 13(8):1036–1040.

Poggie, J. and Smits, A. J. (2001). Shock unsteadiness in a reattaching shear layer. *Journal of Fluid Mechanics*, 429:155–185.

Poggie, J. and Smits, A. J. (2005). Experimental evidence for plotkin model of shock unsteadiness in separated flow. *Physics of Fluids*, 17:018107.

Raffel, M. (2007). *Particle image velocimetry: a practical guide*. Springer Verlag.

Ragni, D., Schrijer, F., van Oudheusden, B. W., and Scarano, F. (2011). Particle tracer response across shocks measured by PIV. *Experiments in Fluids*, 50(1):53–64.

Reynolds, W. C. and Hussain, A. K. M. F. (1972). The mechanics of an organized wave in turbulent shear flow. part 3. theoretical models and comparisons with experiments. *Journal of Fluid Mechanics*, 54(02):263–288.

Robinet, J. C. (2007). Bifurcations in shock-wave/laminar-boundary-layer interaction: global instability approach. *Journal of Fluid Mechanics*, 579(1):85–112.

Samimy, M. and Lele, S. K. (1991). Motion of particles with inertia in a compressible free shear layer. *Physics of Fluids A: Fluid Dynamics*, 3:1915.

Sandham, N. D., Yao, Y. F., and Lawal, A. A. (2003). Large-eddy simulation of transonic turbulent flow over a bump. *International Journal of Heat and Fluid Flow*, 24(4):584–595.

Sartor, F., Losfeld, G., and Bur, R. (2012). PIV study on a shock induced separation in a transonic flow. *Experiments in Fluids*, 53(3):815–827.

Schrijer, F. F. J., Scarano, F., and Van Oudheusden, B. W. (2006). Application of piv in a mach 7 double-ramp flow. *Experiments in fluids*, 41(2):353–363.

Selig, M. S., Andreopoulost, J., Muck, K. C., Dussauge, J. P., and Smits, A. J. (1989). Turbulence structure in a shock wave/turbulent boundary-layer interaction. *AIAA journal*, 27(7):862–869.

Sipp, D. and Marquet, O. (2012). Characterization of noise amplifiers with global singular modes: the case of the leading-edge flat-plate boundary layer. *Theoretical and Computational Fluid Dynamics*, pages 1–19.

Sipp, D., Marquet, O., Meliga, P., and Barbagallo, A. (2010). Dynamics and control of global instabilities in open-flows: a linearized approach. *Applied Mechanics Reviews*, 63(3):30801.

Souverein, L. J., Dupont, P., Debiève, J. F., Van Oudheusden, B. W., and Scarano, F. (2010). Effect of interaction strength on unsteadiness in shock-wave-induced separations. *AIAA journal*, 48(7):1480–1493.

Souverein, L. J., Van Oudheusden, B. W., Scarano, F., and Dupont, P. (2009). Application of a dual-plane particle image velocimetry (dual-PIV) technique for the unsteadiness characterization of a shock wave turbulent boundary layer interaction. *Measurement Science and Technology*, 20:1–16.

Spalart, P. R. and Allmaras, S. R. (1992). A one equation turbulence model for aerodinamic flows. *AIAA journal*, 94.

Theofilis, V. (2003). Advances in global linear instability analysis of nonparallel and three-dimensional flows. *Progress in aerospace sciences*, 39(4):249–315.

Theofilis, V. (2011). Global linear instability. *Annual Review of Fluid Mechanics*, 43:319–352.

Theofilis, V., Hein, S., and Dallmann, U. (2000). On the origins of unsteadiness and three-dimensionality in a laminar separation bubble. *Philosophical Transactions of the Royal Society of London. Series A: Mathematical, Physical and Engineering Sciences*, 358(1777):3229–3246.

Thiery, M. and Coustols, E. (2006). Numerical prediction of shock induced oscillations over a 2d airfoil: Influence of turbulence modelling and test section walls. *International journal of heat and fluid flow*, 27(4):661–670.

Thomas, F. O., Putnam, C. M., and Chu, H. C. (1994). On the mechanism of unsteady shock oscillation in shock wave/turbulent boundary layer interactions. *Experiments in Fluids*, 18(1-2):69–81.

Touber, E. and Sandham, N. D. (2008). Oblique shock impinging on a turbulent boundary layer: low-frequency mechanisms. *AIAA paper*, 2008-4170.

Touber, E. and Sandham, N. D. (2009a). Comparison of three large-eddy simulations of shock-induced turbulent separation bubbles. *Shock Waves*, 19(6):469–478.

Touber, E. and Sandham, N. D. (2009b). Large-eddy simulation of low-frequency unsteadiness in a turbulent shock-induced separation bubble. *Theoretical and Computational Fluid Dynamics*, 23(2):79–107.

Touber, E. and Sandham, N. D. (2011). Low-order stochastic modelling of low-frequency motions in reflected shock-wave/boundary-layer interactions. *Journal of Fluid Mechanics*, 671:417–465.

Trefethen, L., Trefethen, A., Reddy, S., and Driscoll, T. (1993). Hydrodynamic stability without eigenvalues. *Science*, 261(5121):578–584.

van Oudheusden, B. W., Jöbsis, A. J. P., Scarano, F., and Souverein, L. J. (2011). Investigation of the unsteadiness of a shock-reflection interaction with time-resolved particle image velocimetry. *Shock Waves*, 21:1–13.

Webster, D. R., DeGraaff, D. B., and Eaton, J. K. (1996). Turbulence characteristics of a boundary layer over a two-dimensional bump. *Journal of Fluid Mechanics*, 320:53–70.

Wu, M. and Martin, M. P. (2007). Direct numerical simulation of supersonic turbulent boundary layer over a compression ramp. *AIAA journal*, 45(4):879–889.

Wu, M. and Martin, M. P. (2008). Analysis of shock motion in shockwave and turbulent boundary layer interaction using direct numerical simulation data. *Journal of Fluid Mechanics*, 594:71.

Unsteadiness in transonic shock-wave/boundary-layer interactions: experimental investigation and global stability analysis

A transonic interaction between a shock wave and a turbulent boundary layer is experimentally and theoretically investigated. The configuration is a transonic channel flow over a bump, where a shock wave causes the separation of the boundary layer and a recirculating bubble is observed downstream of the shock foot.
First, the mean flow is experimentally investigated by means of PIV, then different techniques allows to identify the main unsteadiness of this shock-wave/boundary-layer interaction. As recognised in similar configurations, the flow presents two distinct characteristic frequencies, whose origins are still unknown.
Numerical simulations are performed solving Reynolds-averaged Navier-Stokes equations. Results are in good agreement with the experimental investigation on the mean flow, but the approach fails to predict the unsteady behaviour of the configuration. The solution of RANS equations is then considered as a base flow, and a global stability analysis is performed. Eigenvalue decomposition of the linearised Navier-Stokes operator indicates that the interaction is stable, and the dynamics cannot be described by unstable global modes.
A linearised approach based on a singular-value decomposition of the global Resolvent is then proposed: the noise-amplifier behaviour of the flow is highlighted by the linearised approach. Medium-frequency perturbations are shown to be the most amplified in the mixing layer, whilst the shock wave behaves as a low-pass filter. Optimal forcing and optimal response are capable to reproduce the mechanisms that are responsible for these two phenomena. A restriction on the location of the forcing can give an insight on the origin on the unsteadiness.
The same approach is then applied to a transonic flow over the OAT15A profile, where the flow can present, for a range of angles of attack, high-amplitude self-sustained shock oscillations. Global stability analysis indicates that the shock buffet onset is linked to a Hopf bifurcation, and the eigenvalue decomposition can describe the phenomenon when an unstable global mode is present. Regardless of the angle of attack, singular-value decomposition of the global Resolvent can describe the convective instabilities responsible of medium-frequency unsteadiness.

Mots-clés : SHOCK-WAVE/BOUNDARY-LAYER INTERACTION ; SWBLI ; TRANSONIC ; STABILITY ANALYSIS ; BUFFET

Instationnarités dans les interactions choc/couche-limite en régime transsonique : étude expérimentale et analyse de stabilité

Dans cette étude nous considérons l'interaction entre une onde de choc et une couche limite turbulente dans un écoulement transsonique sur une bosse d'un point de vue expérimentale et théorique, ainsi que dans un écoulement autour d'un profil d'aile. Dans le premier cas, des mesures ont permis de montrer que l'interaction est caractérisée par la coexistence de deux fréquences distinctes, mais l'origine des oscillations basse fréquence est controversée. Des simulations numériques s'appuyant sur les équations RANS permettent une description de l'écoulement moyen, mais ne sont pas capables de reproduire le comportement instationnaire de l'interaction. Nous proposons une étude de stabilité globale : une décomposition en valeurs propres de l'opérateur de Navier-Stokes linéarisé au tour d'un champ de base RANS indique que l'interaction est un phénomène stable, et la dynamique de l'écoulement ne peut pas être décrite par un mode global instable.
Nous considérons ensuite une approche linéarisée, où la réceptivité de l'écoulement à un forçage externe est analysée à travers une décomposition en valeurs singulières du Résolvant Global. Cette approche est proposée afin d'expliquer la sélection de fréquence dans cet écoulement, et montre que l'interaction filtre et amplifie le bruit résiduel existant : certaines perturbations sont plus amplifiées dans la couche de mélange, tandis que le choc semble se comporter comme un filtre passe-bas.
La même approche est enfin appliquée sur un cas d'écoulement transsonique autour d'un profil d'aile, qui peut présenter des oscillations périodiques de l'onde de choc. La décomposition en valeurs propres de l'opérateur de Navier-Stokes linéarisé est capable de décrire la dynamique instationnaire quand un mode instable est présent. Cependant, la décomposition en valeurs singulières du Résolvant Global peut indiquer la présence des instabilités convectives qui sont responsables du comportement instationnaire à moyenne fréquence de l'écoulement.

Keywords : INTERACTION ONDE DE CHOC/COUCHE LIMITE ; IOCCL ; TRANSSONIQUE ; ANALYSE DE STABILITE ; TREMBLEMENT

Office National d'Études et de Recherches Aérospatiales
BP 72 - 29 avenue de la Division Leclerc
92322 CHATILLON CEDEX
Tél. : +33 1 46 73 40 40 - Fax : +33 1 46 73 41 41
http://www.onera.fr